広島大学 学位論文

Nature of chemical bonds in double perovskite-type oxide BaBiO₃ and related oxides visualized by synchrotron-radiation X-ray diffraction

放射光X線回折により可視化された

二重ペロブスカイト型酸化物

BaBiO₃および関連酸化物の化学結合の性質

2020 年

広島大学大学院理学研究科

物理科学専攻

Qing Zhao

目　次

３．参考論文

(1) Transformation of Perovskite $BaBiO_3$ into Layered $BaBiO_{2.5}$ Crystals Featuring Unusual Chemical Bonding and Luminescence.

Hong Li, **Qing Zhao**, Bo-Mei Liu, Jun-Ying Zhang, Zhi-Yong Li, Shao-Qiang Guo, Ju-Ping Ma, Yoshihiro Kuroiwa, Chikako Moriyoshi, Li-Rong Zheng, and Hong-Tao Sun:

Chem. Eur. J. 2018, 24, 8875 − 8882.

(2) Cs_4PbBr_6/$CsPbBr_3$ Perovskite Composites with Near-Unity Luminescence Quantum Yield: Large-Scale Synthesis, Luminescence and Formation Mechanism, and White Light-Emitting Diode Application.

Ya-Meng Chen, Yang Zhou, **Qing Zhao**, Jun-Ying Zhang, Ju-Ping Ma, Tong-Tong Xuan, Shao-Qiang Guo, Zi-Jun Yong, Jing Wang, Yoshihiro Kuroiwa, Chikako Moriyoshi, and Hong-Tao Sun:

ACS Appl. Mater. Interfaces 2018, 10, 15905−15912.

(3) Ion-Exchangeable Microporous Polyoxometalate Compounds with Off-Center Dopants Exhibiting Unconventional Luminescence.

Dan-Dan Zhou, **Qing Zhao**, Fu-Ping Zhu, Zhi-Gang Zhang, Yang

Zhou, Zi-Jun Yong, Ju-Ping Ma, Yoshihiro Kuroiwa, Chikako Moriyoshi, Yong-Zheng Fang, Jia-Li Gu, Jie Shu, Zhi-Yong Li, Jian-Mei Chen, Li-Rong Zheng, and Hong-Tao Sun:

Chem. Eur. J. 2018, 24, 9976 – 9982.

(4) X-ray-activated long persistent phosphors featuring strong UVC afterglow emissions.

Yan-Min Yang, Zhi-Yong Li, Jun-Ying Zhang, Yue Lu, Shao-Qiang Guo, **Qing Zhao**, Xin Wang, Zi-Jun Yong, Hong Li, Ju-Ping Ma, Yoshihiro Kuroiwa, Chikako Moriyoshi, Li-Li Hu, Li-Yan Zhang, Li-Rong Zheng and Hong-Tao Sun:

Light: Science & Applications 2018, 7, 88.

(5) Defective $[Bi_2O_2]^{2+}$ Layers Exhibiting Ultrabroad Near-Infrared Luminescence.

Hong Li, Xiao-Fang Jia, **Qing Zhao**, Ju-Ping Ma, Jian-Dang Liu, Bang-Jiao Ye, Yoshihiro Kuroiwa, Chikako Moriyoshi, Zhi-Yong Li, Qi Liu, Jun-Ying Zhang, and Hong-Tao Sun:

Chem. Eur. J. 2019, 25, 12842 – 12848.

(6) Defect-Triggered Phase Transition in Cesium Lead Halide Perovskite Nanocrystals.

Ju-Ping Ma, Jun Yin, Ya-Meng Chen, **Qing Zhao**, Yang Zhou, Hong Li, Yoshihiro Kuroiwa, Chikako Moriyoshi, Zhi-Yong Li, Osman M. Bakr, Omar F. Mohammed, and Hong-Tao Sun:

ACS Materials Lett. 2019, 1, 185−191.

(7) Doping Induces Structural Phase Transitions in All-Inorganic Lead Halide Perovskite Nanocrystals.

Ju-Ping Ma, Jia-Kai Chen, Jun Yin, Bin-Bin Zhang, **Qing Zhao**, Yoshihiro Kuroiwa, Chikako Moriyoshi, Lili Hu, Osman M. Bakr, Omar F. Mohammed, and Hong-Tao Sun:

ACS Materials Lett. 2020, 2, 367−375.

主論文

Abstract

Perovskite-type oxide $BaBiO_3$ has attracted extensive research interests since the discovery of superconductivity in the doped solid solutions (Ba, K) (Pb, Bi) O_3. Considering the charge balance, the Bi ion normally will take average 4+ valence state in the compound. However, as the Bi ion is referred to be a "valence skipper", hence, the Bi ions are suggested to exhibit charge disproportionation from average Bi^{4+} valence state to Bi^{3+} and Bi^{5+} valence states with equal ratio. $BaBiO_3$ is supposed to be not a simple perovskite, but a *B*-site ordered double perovskite with two different *B*-sites in the compound. The charge ordering accounts for the fact that $BaBiO_3$ is electrically semiconductor with a band gap. However, clear experimental evidence of Bi charge order is lacking.

Accurate electron charge density distributions of $BaBiO_3$ have been obtained by the high-resolution synchrotron-radiation powder X-ray diffraction data using the maximum entropy method/Rietveld method. The charge ordered $Ba_2Bi^{3+}Bi^{5+}O_6$ double perovskite adopts four structures, i.e., monoclinic $P2_1/n$, monoclinic $I2/m$, rhombohedral $R\bar{3}$, and cubic $Fm\bar{3}m$ phases upon heating progress. We investigate these phase transitions at charge density level, such as the change of chemical bonding nature and possible modifications in charge density. We found $BaBiO_3$ forms a two-dimensional covalent layer with $P2_1/n$ symmetry, a three-dimensional covalent network with $I2/m$ and $R\bar{3}$ symmetry, and an ionic structure consisting of isolated Bi^{3+} ions and $[Bi^{5+}-O6]^{7-}$ octahedron upon heating progress.

In order to discover the novel oxides with intriguing properties, engineered local

environments of cations coordinated with oxygen ions in oxides is an effective pathway. Here we present the successful synthesis of $BaBiO_{2.5}$ with layered structure enabled by a non-topotactic phase transformation from the perovskite-type oxide $BaBiO_3$. Using the maximum entropy method/Rietveld method based on the high-resolution powder synchrotron-radiation X-ray diffraction data, we successfully found that Bi ions form unusual chemical bonds with four coordinated oxygen ions that results in an asymmetric coordination geometry. One ionic bond and three covalent bonds of Bi-O bonds are successfully visualized in this layered structure that is owing to the hybridization of O $2p$ and Bi $6p$ orbitals. Specifically, we find that this unusual structure shows the near-infrared photoluminescence different from the ordinary Bi-containing systems. Experimental and quantum chemistry calculations motivate us to propose the excitonic nature of near-infrared photoluminescence. Our work highlights that creating materials with unusual Bi-O bondings and Bi coordination geometry will provide a pathway to discover the materials with new physical properties. We believe this work may stimulate interests in exploring a series of materials containing heavier p-block elements, thus providing prospects for discovering systems with unconventional properties.

Contents

Chapter 5

Electron charge density study of BaBiO$_{2.5}$

Acknowledgment

References

Chapter 1

Introduction

1.1 Perovskite-type structure

Perovskite-type structure materials are widely found in nature and firstly get its name from a mineral with the formula $CaTiO_3$. Generally, the chemical formula of perovskite can be described with formula ABX_3. The A-site is usually occupied by the alkaline or alkaline earth ions with larger ions radii, and the B-site is usually occupied by the transition metal ions with smaller ions radii, and the X sites are usually oxygen ions or halide ions.[1-4] Geometrically, the standard ideal crystal structure of perovskite is expected to be cubic symmetry with the $Pm\overline{3}m$ space group as shown in Fig. 1-1. A-site ions locate at the eight vertices of the cubic cell, and the X site ions locate at the center of each of the six faces to form an oxygen octahedron, while B site ions occupy the center of the oxygen octahedron. The A-site is surrounded by twelve oxygen ions. In cubic $Pm\overline{3}m$ symmetry, the position of the A sites is (0, 0, 0), the position of the B sites is (1/2, 1/2, 1/2), and the position of the X sites is (1/2, 1/2, 0).
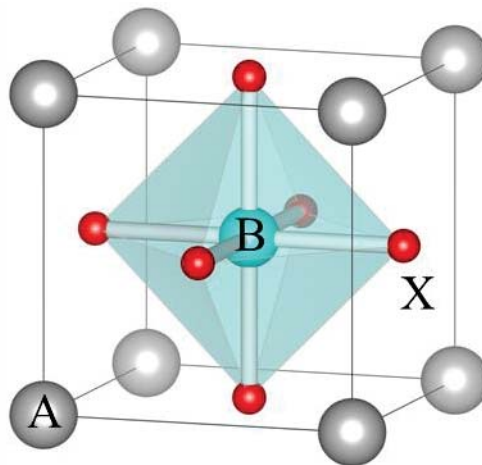
Figure 1-1 Cubic crystal structure of perovskite ABX_3 with $Pm\overline{3}m$ space group.

Perovskite structures are well known the most frequently involved structures in the solid-state inorganic chemistry. The cations in perovskite can be used with almost all the metallic elements in the periodic table. One hand, to form a stable perovskite structure, the valence balance is necessary. On the other hand, in the perovskite structure, the ions radii play a very important role in the structural stability. Various ions can occupy both A- and B- site in a perovskite structure. Here the ionic radius of A-site, B-site cations and O-anions is recorded as R_A, R_B and R_O, and there is a certain geometric relationship among these three parameters. For an ideal cubic simple perovskite structure, there must exist

$$R_A + R_O = \sqrt{2}(R_B + R_O) \qquad (1\text{-}1)$$

In the ideal cubic perovskite shown in Fig. 1-1, it can be concluded that two times of the B-O bond length is exactly equal to the length of its cell parameter, and two times of the A-O bond length is equal to the length of the plane diagonal. Here, the bond length is simply equivalent to the sum of the Shannon ion radii of the two ions constituting the bond,[5] so the above equation can be obtained. In fact, in many existing perovskite compounds, the above equation is not absolutely suitable. Anions and cations are allowed to deviate slightly. So, the actual perovskite structure has a relationship shown below,

$$t = \frac{R_A + R_O}{\sqrt{2}(R_B + R_O)} \qquad (1\text{-}2)$$

The physical quantity t introduced here is called tolerance factor. It is obvious that the ideal tolerance factor t of cubic perovskite is equal to one. However, the tolerance factor formula ignores the influence of ion coordination number on the effective ion radius. So, in the actual experiment material, the tolerance factor of most perovskite materials cannot be equal to one perfectly. Generally, the tolerance factor is between 0.8 and 1. Therefore, when the effective ion radius of the A-site cation is too large or

the ion radius of the *B*-site is too small, that is, the tolerance factor *t* value deviates from the allowable range, no stable perovskite structure can be formed. In addition to the above geometric structure conditions, the anions and cations of perovskite also need to meet the charge balance, so that the overall electric neutrality is maintained, that is, the sum of the valence of cations at *A* and *B* positions should be kept at six in a perovskite-type oxide.

Table 1-1 Tolerance factor of A site atom and B site atom of perovskite type oxide at room temperature. The A site atom is calculated with 12 coordination, the B site atom with 6 coordination, and the O atom with 2 coordination (1.35 Å).

Materials	Space group	Tolerance factor *t*
$BaTiO_3$	*P4mm*	1.071
$PbTiO_3$	*P4mm*	1.027
$KNbO_3$	*Amm*2	1.062
$KTaO_3$	*Pm*$\overline{3}$*m*	1.062
$LaAlO_3$	*R*$\overline{3}$*m*	1.017
$KMnF_3$	*Pm*$\overline{3}$*m*	0.980
$SrTiO_3$	*Pm*$\overline{3}$*m*	1.009
$CsPbBr_3$	*Pnma*	0.870
$PbZrO_3$	*Pbam*	0.970

In fact, there are not many perovskite compounds with simple cubic structure, but there are a lot of distorted derivative structures. Although the ions slightly deviate from the ideal position of cubic perovskite, the arrangement and distribution of the ions are consistent with perovskite, and the space group and lattice constant of the compound may change, but the overall structure is still perovskite-type as shown in Table 1-1.[6-8] The calculation of the tolerance factor is performed using nearest coordinated neighbor oxygen. The ionic radius of the atom at *A*-site ions with twelve coordination oxygen is considered, and the ionic radius of the atom at *B*-site with six

coordination oxygen is applied, respectively. In the case of the oxygen ions, only the B-site ions is treated as the first nearest neighbor coordination, and the ion radius with two coordination is about 1.35 Å.

For example, the substitution of ions at the B position of perovskite may lead to the skew and distortion of the octahedron of oxygen at the B position, thus reducing the symmetry of the crystal, and may changing from a cubic system to a tetragonal, orthogonal or monoclinic system. In the distorted perovskite-type structure, the cell side length is usually $\sqrt{2}$ times, n times or $n\sqrt{2}$ times of the simple cubic cell side length. Generally speaking, the symmetry of perovskite structure will change with the change of temperature or pressure. When the temperature or pressure increases, the symmetry increases, the temperature and pressure decrease, and the symmetry decreases. The A and B sites of perovskite structure can be doped by ions, that is, both A and B sites can be occupied by one or several ions. In addition, there are also cations or anions vacancy in the perovskite crystal sometimes.

1.2 B-site ordered double Perovskite-type structure

The name of double perovskite corresponds to that of single perovskite ABO$_3$. Its general chemical formula can be expressed as A_2BB'O$_6$.[9-16] The most important point that is different from ABO$_3$ is that the B-site of perovskite oxide is occupied by two different transition metal elements. The standard B-site ordered double perovskite has an orderly arrangement of oxygen octahedrons composed of different elements in B-site, as shown in Figure 1-2. B- and B'-site ions are the ion with smaller ion radius, generally the transition metal element ions, and A site is the ion with larger radius, the same as ABO$_3$. The B-site ions at the top angle form the face centered cubic structure with the oxygen ions, the B-site ions are located in the body center of the octahedron formed by the O anions, and the A-site ions are located in the body center of the cube formed by the B- and B'-site ions. In the B-site ordered double perovskite-type structure A_2BB'O$_6$, the tolerance factor formula is also applicable, that is

$$R_A + R_O = \sqrt{2}\left(\frac{R_B + R_{B'}}{2} + R_O\right)t \tag{1-3}$$

In most cases, the B-site ordered double perovskite structure is not ideal. Different elements in B- and B'- site, electronic configuration and interaction between ions will cause structural distortion. In the B-site ordered double perovskite, the substitution of B-site elements provides a great possibility to find new materials. In Fig. 1-2, it can be seen that B-site ion and B'-site ions are separated by O ions to form B-O-B' bond, which is 180 ° in ideal case.
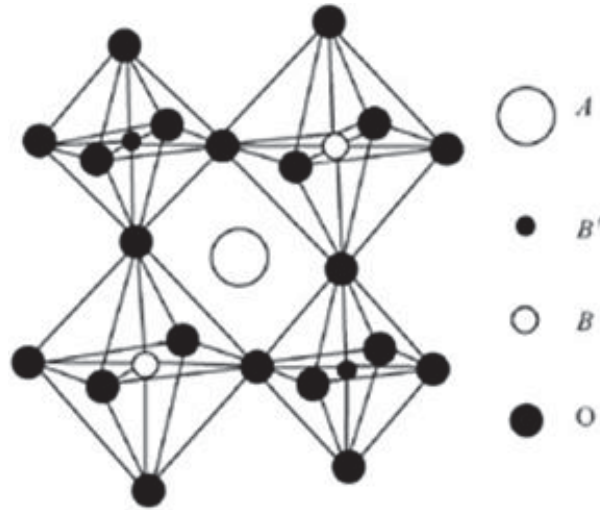
Figure. 1-2 B-site ordered double perovskite oxide

B-site ordered double perovskite oxides have been widely investigated in the recent years owing to its rich interesting physical properties. [17-22] Compared with the simple disordered ABO_3 perovskite, both the B- and B'-site in this ordered structure can adjust different kind of transition metals ions arranged with a rocksalt-type manner. As a consequence, some intriguing magnetic or electrical phenomenon can be observed through the interactions among B-B, B-B' and B'-B' sites, leading to many different kind of intriguing physical properties, such as ferroelectricity, colossal magnetoresistance, half metallic behavior, or high-temperature ferrimagnetic order and so on. One of the famous example is

Sr_2FeMoO_6,[16-17] people observed a high ferromagnetic Curie temperature ($T_C \sim$ 420 K) and half-metallic behavior in this compound, which makes the material to be highly potential for application in spintronic devices above room temperature. This intriguing property inspired the investigations of $3d$-$4d(5d)$ orbitals hybridized through B-B' pathway in B-site ordered double perovskites. Another similar sample is Sr_2CrOsO_6,[12] people found a ferrimagnetic (FiM) phase transition occuring with much higher T_C (725 K) through simply changing the B-site transition metal ions. In addition, People have found interesting spin interactions in the ordered perovskite family of A_2FeOsO_6 (A = Ca, $Ca_{0.5}Sr_{0.5}$, and Sr). Among these compounds, the Fe^{3+} and Os^{5+} ions are ordered at B-sites. With decreasing the size of A-site ions, the crystal symmetry can be reduced owing to the increasing octahedral distortion, where the average Fe-O-Os bond angle is about 165.3° for Sr, 158.9° for $Sr_{0.5}Ca_{0.5}$ and 150.9° for Ca. Sr_2FeOsO_6 shows the tetragonal $I4/m$ symmetry, and $(Ca_{0.5}Sr_{0.5})_2FeOsO_6$ shows the monoclinic $P2_1/n$ sysmetry.[18-22] Two antiferromagnetic phase transitions were observed in Sr_2FeOsO_6 owing to the lattice instability and the competing magnetic superexchange interactions. In contrast, one FiM ordering is found in the monoclinic phase of Ca_2FeOsO_6 and $CaSrFeOsO_6$ showing the Curie temperature about 320 K and 210 K, respectively, which is owed to the AFM ordering between the Fe^{3+} and Os^{5+} ions. In contrast, when the lead ions occupy the A-site, Pb_2FeOsO_6 shows an interesting cubic double ordered perovskite structure with $Pm\bar{3}m$ symmetry. A long-range ferrimagnetic order is observed below 280 K between the neighbored Fe^{3+} and Os^{5+} octahedron through straight Fe-O-Os pathway.

1.3 Charge order

Generally, transition-metal oxides with mixed valence states of ions show very interesting physical properties in some compounds. The compounds with Fe ions sometimes will show many exotic physical phenomena owing to rich valence state of

Fe ions. For instance, an intriguing charge order state was found in the compound Fe_4O_5 that is recently obtained using the high-pressure synthesis method, where the competing Fe^{2+} and Fe^{3+} ordering is revealed.[23,24] Another interesting sample is an *A*-site ordered quadruple perovskite $LaCu_3Fe_4O_{12}$. Charge transfer is observed between Cu and Fe ions via changing the temperature or pressure showing the unusually high Cu^{3+} and $Fe^{3.75+}$ valence states, meanwhile, the sharp variations of unit cell, changes of magnetic and electrical transport properties are observed accompanied with negative thermal expansion.[2,25,26] Charge ordering is usually easy to be observed in transition metal oxides with mixed-valent ions.[27-29] The perovskite with Mn ions is especially potential to observe long-range charge ordering of the Mn^{3+} and Mn^{4+} ions in these materials owing to the antiferromagnetic spin ordering, or the orbital ordering of Mn^{3+} ions accompanied with lattice distortions. After the long-range ordering, people usually can observe a series of changes in the resistivity, magnetization, and lattice parameter. The charge ordering transition are generally associated with the effects of chemical pressure introduced by cation size, temperature, pressure, or magnetic field.

1.4 Phase transition

In many kinds of perovskite type oxides, structural phase transitions occur when the temperature changes. From high temperature to low temperature, the symmetry usually decreases. Structural phase transition is usually accompanied by visible changes in atomic position and lattice distortion in the crystal. For example, phase transition in ferroelectricity perovskite oxide appears when the crystal phase become low symmetric phase with non-centro symmetry via temperature decreasing. The spontaneous atomic displacement causes the corresponding structural phase transitions. During the process, the fundamental vibration of a transverse wave among the lattice vibrations is frozen with decreasing temperature, which is essentially sensitive to the temperature. As the temperature decreases, the crystal symmetry

decrease, at the same time, the frequency of the fundamental vibration decreases, where the softening of phonon occurs, and this kind of softening fundamental vibration is called the soft mode. The anharmonicity of the lattice vibrations is believed to play a critical role in the mechanism of softening process. When the lattice vibration is anharmonic, with decreasing temperature the frequency of fundamental vibration decrease owing to the restoring force of lattice vibration. Below the phase transition temperature, the frequency of the soft mode becomes zero, the atomic displacement pattern corresponding to this soft mode is frozen, and a ferroelectric phase with low symmetric can be realized. The soft mode of lattice vibrations largely depends on the different mass of atoms consisting of compounds, crystal structure parameters, thermal vibration of atoms, the bonding nature and the interaction between atoms, including the dipole field, etc. Soft mode has been used not only to explain the phase transition of ferroelectrics, but the phase transition of superconductivity, or the metal-insulator phase transition.[30]

When people try to investigate the phase transition of perovskite oxide, two kind of soft modes are most frequently used to explain the process of phase transition. One mode is the Γ_{15} mode that is a mode of octahedron consisting of six oxygen occupying the center of the Brillouin zone. The other modes are M_3 and R_{25} modes at the boundary of Brillouin zone, which are the rotation modes of oxygen octahedron. Figure 1-3 shows the Brillouin zone in the simple cubic structure of the perovskite oxide. Rotation of Γ, M, R means the phonon mode revealing each reciprocal point in the Brillouin zone.[31] People can observe different kind variation of soft mode in the phase transitions of perovskite-type materials.
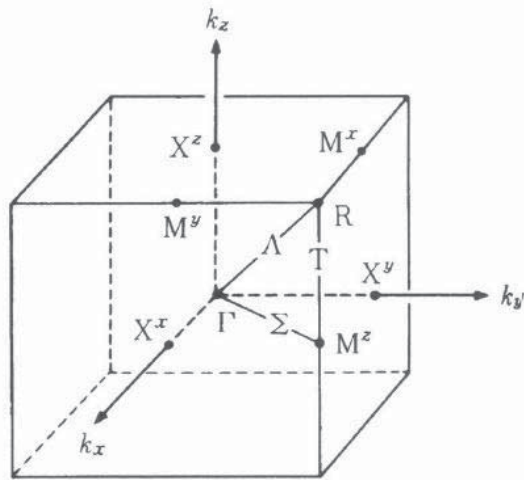
Figure 1-3 Brillouin zone of cubic perovskite-type structure.

For example, the Γ_{15} mode is a transverse wave optical mode of infrared active. when the mode is softened and frozen, the phase transition takes place with the atomic displacement occurring along the [001] direction, which usually allows the appearance of spontaneous polarization for ferroelectric materials. Figure 1-4 shows three different kind of atomic displacement of the Γ_{15} mode,[31] (a) indicates the relative motion between the B-site ions and the surrounded oxygen octahedron called the Slater mode, (b) between A-site ions and oxygen octahedron with B-site ions called the Last mode, and (c) shows the transformation of oxygen octahedron. For example, the spontaneous polarization of ferroelectric $BaTiO_3$ can be explained using slater mode. In comparison, the mechanism of phase transition of ferroelectric $PbTiO_3$ can be attributed to the combination of the Slater mode and Last mode.
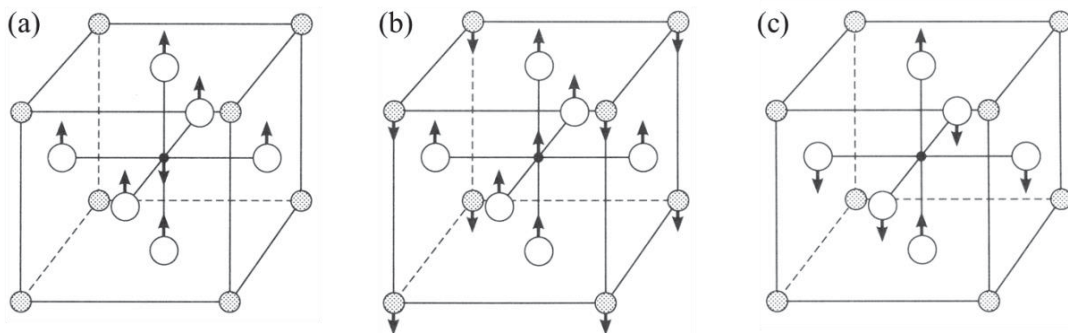
Figure 1-4 Atomic displacement when Γ_{15} mode is frozen; (a) slater mode, (b) last mode, (c) O octahedron displacement mode.

9

Differently, Figure 1-5 shows the rotational displacement of oxygen octahedron in a crystal structure when the M_3 and R_{25} modes are frozen,[31] which is a transverse acoustic mode. The rotation of oxygen octahedron is around the <001> axis. In the M_3 mode, the adjacent oxygen octahedrons of up and down take the rotation along the same direction, however, in the R_{25} mode, the directions of rotation of oxygen octahedrons are opposite, which will cause the occurring of super lattice structure owing to the alternate twisting of octahedrons. These two modes are usually easy to be observed in the low temperature antiferroelectric phases.
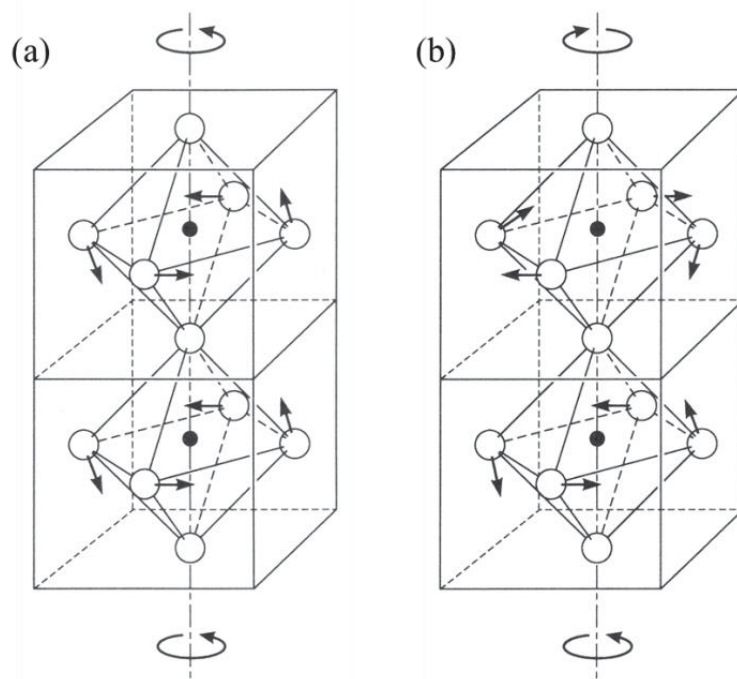
Figure 1-5 Atomic displacement when M_3, R_{25} mode is frozen; (a) M_3 mode and (b) R_{25} mode.

For the perovskite-type structure, these three different kinds of modes can all be the candidates to explain the phase transition. The choice of the soft modes is found to be strongly depending on different perovskite materials. In general, there seem to exist a competition between the Γ_{15} mode, and M_3 and R_{25} modes. In the perovskite

material, when phase transition take place with the Γ_{15} mode, the M_3 and R_{25} modes seem to not exist, which conversely makes sense in most cases. This phenomenon of separation behavior of phase transition mode can be revealed using the tolerance factor of perovskite-type structure.[32]

The ideal tolerance factor should be equal to unit in the cubic perovskite structure. The tolerance factor was proposed to classify the stability of different of the perovskite-type structure consisting of different element ions. In some point, the tolerance factor can also be used to explain the competition among different kind of soft mode. The Shannon ion radius is often used for ionic radius. In general, when the tolerance $t > 1$, there exists a large enough space around the B-site ions rather than around the A-site ions, which benefits the occurring of Γ_{15} mode. However, when the tolerance factor $t < 1$, it means that there exists space around the A-site ions instead. In such case, the phase transition is accompanied with the M_3 or R_{25} modes. There also exist some special cases, for example, $LaAlO_3$ was found to have a phase transition with the R_{25} mode, and phase transition of $SrTiO_3$ showed the combination of Γ_{15} mode with the decreasing process and R_{25} mode at very low temperature. In addition, Table 1-2 shows some existing examples of perovskite-type compounds with different tolerance factor and soft modes.[31,33,34] The soft modes of different perovskite compounds almost obey the tendency related to the tolerance factor mentioned above. Generally, with tolerance factors $t > 1$, the Γ_{15} mode, which is at the Brillouin zone center, is easily to occur. On the other hand, with tolerance factor $t < 1$, the M_3 and R_{25} modes, which are at the Brillouin zone boundary, are easily to get frozen.

Table 1-2 Tolerance factor and the soft modes of various perovskite-type compounds at low temperature.

Materials	Soft mode	Tolerance factor t
$BaTiO_3$	Γ_{15}	1.071
$PbTiO_3$	Γ_{15}	1.027
$KNbO_3$	Γ_{15}	1.062
$KTaO_3$	Γ_{15}	1.062
$LaAlO_3$	R_{25}	1.017
$KMnF_3$	M_3	0.980
$SrTiO_3$	Γ_{15}	1.009
$CsPbBr_3$	R_{25}	0.870
$PbZrO_3$		0.970

The phase transition usually accompanies with the distortion from the ideal perovskite structure. The distortion is generally attributed to three factors, that is the octahedra distortions, ions displacements within the octahedra and octahedra tilting. In early years, Glazer reported the Glazer notation system to classify the distortion. The Glazer notation tilt system can be described using the rotation of the octahedra correspond to three axes. The description of rotations is presented with two parameters. For example, a rotation system $a^+a^+a^+$ indicates the same rotation about each axis. The first parameter a describe the magnitude of the rotation. Hence, the rotation system $a^+a^+c^+$ shows a different rotation angle about z axis. The second parameter is the +, - or 0 superscript. The positive superscript indicates the same rotation direction between the adjacent layers of octahedra, the negative superscript reveals the opposite rotation of the neighbored octahedra, and zero superscript is applied with no rotations. There are total 23 types of Glazer notation divided into four groups with the number of tilt parameters as shown in Table 1-3.[35,36] Correspondingly, M_3 mode and R_{25} mode can also be defined using Glazer tilting system as $a^0a^0c^+$ and $a^0a^0c^-$ as shown in Fig. 1-5, respectively.

Table 1-3 Classification of space groups by Glazer notation.

Tilt system number	Tilt system symbol	Space group	Tilt system number	Tilt system symbol	Space group
Three-tilt systems			*Two-tilt systems*		
1	$a^+ b^+ c^+$	*Immm*	15	$a^0 b^+ c^+$	*Immm*
2	$a^+ b^+ b^+$	*Immm*	16	$a^0 b^+ b^+$	*I4/mmm*
3	$a^+ a^+ a^+$	*Im$\bar{3}$*	17	$a^0 b^+ c^-$	*Cmcm*
4	$a^+ b^+ c^-$	*Pmmn*	18	$a^0 b^+ b^-$	*Cmcm*
5	$a^+ a^+ c^-$	*P4$_2$/nmc*	19	$a^0 b^+ c^-$	*I2/m*
6	$a^+ b^+ b^-$	*Pmmn*	20	$a^0 b^- b^-$	*Imma*
7	$a^+ a^+ a^-$	*P4$_2$/nmc*			
8	$a^+ b^- c^-$	*P2$_1$/m*			
9	$a^+ a^- c^-$	*P2$_1$/m*	*One-tilt systems*		
10	$a^+ b^- b^-$	*Pnma*	21	$a^0 a^0 c^+$	*P4/mbm*
11	$a^+ a^- a^-$	*Pnma*	22	$a^0 a^0 c^-$	*I4/mcm*
12	$a^- b^- c^-$	*P$\bar{1}$*			
13	$a^- b^- b^-$	*I2/a*	*Zero-tilt systems*		
14	$a^- a^- a^-$	*R$\bar{3}$c*	23	$a^0 a^0 a^0$	*Pm$\bar{3}$m*

# 1.5 Electron charge density study by synchrotron radiation X-ray diffraction

The discovery of X-rays was one of the most important discoveries of physics in the late 19th and early 20th centuries, which provides an effective research method for many scientific fields. The discovery and research of X-rays play a huge important role in the impact on the development of physics and the entire science and technology since the 20th century. In 1895, Rontgen reported a discovery of new kind of ray named X-rays. Barkla found the polarization of the X-rays, which is a big step

forward in understanding the nature of X-rays. In 1912, Laue found the X-ray diffraction phenomenon when a beam of X-rays hitting on a crystal, which captured the scattering on the plate. The wave properties of X-rays were proved for the first time. Hence, Laue was awarded the Nobel Prize in 1914 year for this discovery. In the following year 1913, Bragg father and son designed the first X-ray spectrometer, which was successfully used to analysis the structure of NaCl crystal. X-rays was proved to have effectiveness for analyzing crystal structure. The formation of X-rays crystal diffraction was clearly explained, and the most famous Bragg formula was proposed. In 1916 year, Debye and Scherrer developed a method to study crystal structure using X-rays with powder polycrystal samples, and they observed the diffraction pattern of concentric rings called Debye-Scherrer ring on the imaging plate. Compared with single crystal samples, polycrystalline samples are much easier to obtain, which facilitates the study of crystal structural analysis. When a charged particle with a speed close to the speed of light makes a circular motion in a magnetic field, it emits a continuous spectrum of electromagnetic waves along the tangent direction of the deflection orbit. In 1947, people first observed this kind of electromagnetic wave on an electron synchrotron and called it the synchrotron radiation. Since then, people started to use the synchrotron-radiation X-ray diffraction (SXRD) to determine the crystal structure of materials. In the past 100 years, X-ray diffraction analysis of crystal structure has been greatly developed. Since X-ray diffraction has a correlation with the electrons, the obtained diffraction peak contains information about the electron density around the atoms. X-ray diffraction has already been recognized as an excellent method in the direct observation of chemical bonds in crystals structure in the real space.

Electron charge density study using synchrotron-radiation X-ray diffraction plays an important role to reveal the relationship between crystal structure and physical properties. In recent years, accuracy of experimentally obtained charge density distributions has made spectacular advances through analyzing the synchrotron-radiation powder X-ray diffraction data using the maximum entropy method (MEM)/Rietveld method. Generally, the Rietveld structural analysis is limited to the

atomic level, which gives some limited structural information, i.e. lattice constants, atomic position, thermal vibration, bonding angle, and bonding distance, etc. However, these structural parameters of atomic level sometimes fail to give an accurate connection between structure and physical properties. The MEM/Rietveld method is recognized as a combination between the MEM method and the Rietveld analysis, which has successfully been applied in the charge density studies to complementary the structural analysis.

The charge density study can be used in investigating the bonding nature in the crystal structure. For instance, a novel superconductor MgB_2 shows a geometric three-dimensional (3D) nested structure with boron honeycomb sheets sandwiched between Mg triangular sheets. Furthermore, the corresponding MEM charge density clearly reveals the bonding nature around B ions and Mg ions. The two-dimensional (2D) strong covalent bonding network of boron ions and the full ionization of Mg ions are observed in the MEM charge density distribution map as shown in Fig. 1-6.[37,38] This kind of 2D layered structure usually benefits the superconductivity, which is related to the superconductive mechanism.
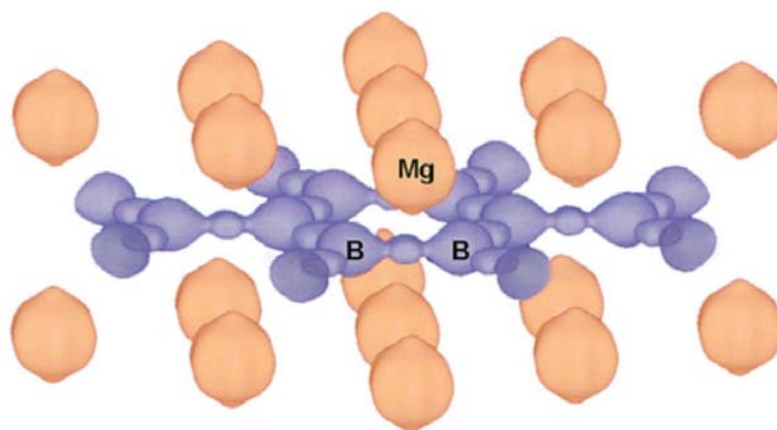
Figure 1-6 The MEM charge density distribution of MgB_2 at 15 K. The isosurface shown here is 0.75 e $Å^{-3}$

Another sample to show the difference in bonding nature using MEM/Rietveld method is a spin-crossover complex, that is $Fe(phen)_2(NCS)_2$ shows a reversible low-spin to high-spin transition induced by laser at low temperature about 92 K as

shown in Fig. 1-7.[39] The Fe^{2+} ions are surrounded by six N atoms in crystal structure at both low-spin and high-spin phase, therefore, Fe^{2+} ions show more isolated from the neighbored N atoms at high-spin phase with a much lower charge density in a longer Fe^{2+}-N bond.
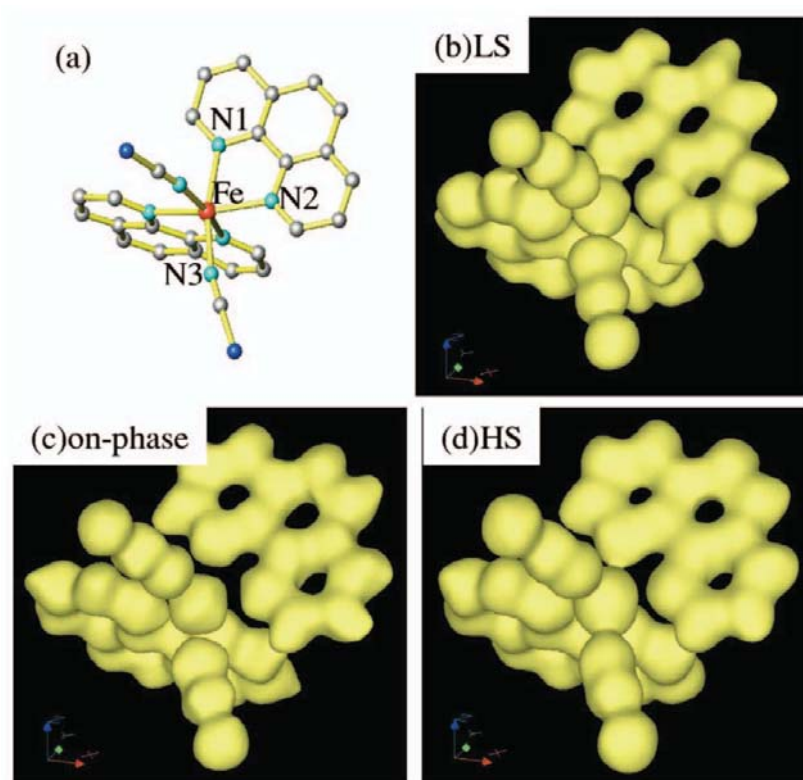

Figure 1-7 (a) Crystal structure of $Fe(phen)_2(NCS)_2$ with Ball and stick model. The MEM charge density distribution of (b) the LS phase at 92 K, (c) the on phase using laser at 92 K, and (d) the HS phase at 260 K, Isosurface is 0.45 e $Å^{-3}$.

Our group has been revealing the structural characteristics of perovskite-type oxide ferroelectrics using MEM/Rietveld method, such as $BaTiO_3$ and $PbTiO_3$. The precise charge density distributions of $BaTiO_3$ and $PbTiO_3$ have been evaluated to understand the chemical bonding nature from an electronic viewpoint. $BaTiO_3$ forms an ordinary three-dimensional (3D) covalent network of $Ti-O_6$ octahedron in all phases as shown in Fig. 1-8. In comparison, Strong covalence on the Pb-O bond is observed in the tetragonal $PbTiO_3$, which forms a two-dimensional (2D) layered structure of a covalent bonding network of the $Ti-O_5$ pyramid and the covalent Pb-O

bonds, however, in cubic PbTiO$_3$, the bonding nature of Pb-O bonds shows distinct ionic as shown in Fig. 1-9.[40,41] The possible existing orbital hybridization between Ti-O and Pb-O predicted by first-principles calculation is successfully visualized. It seems like the phase transitions are accompanied by changes in the bonding nature of some specific bonds.
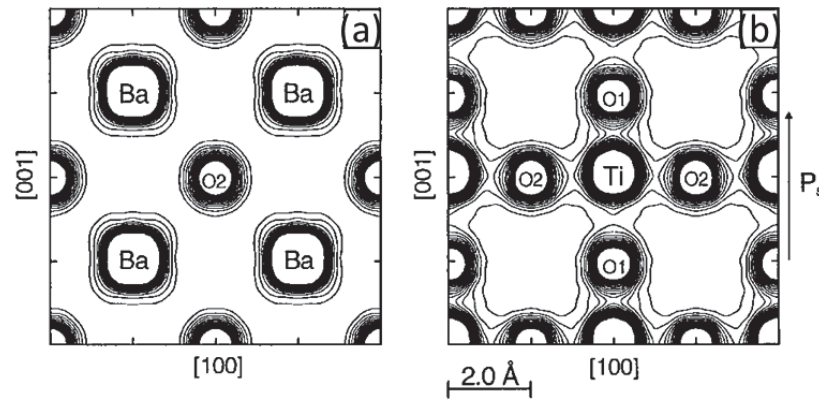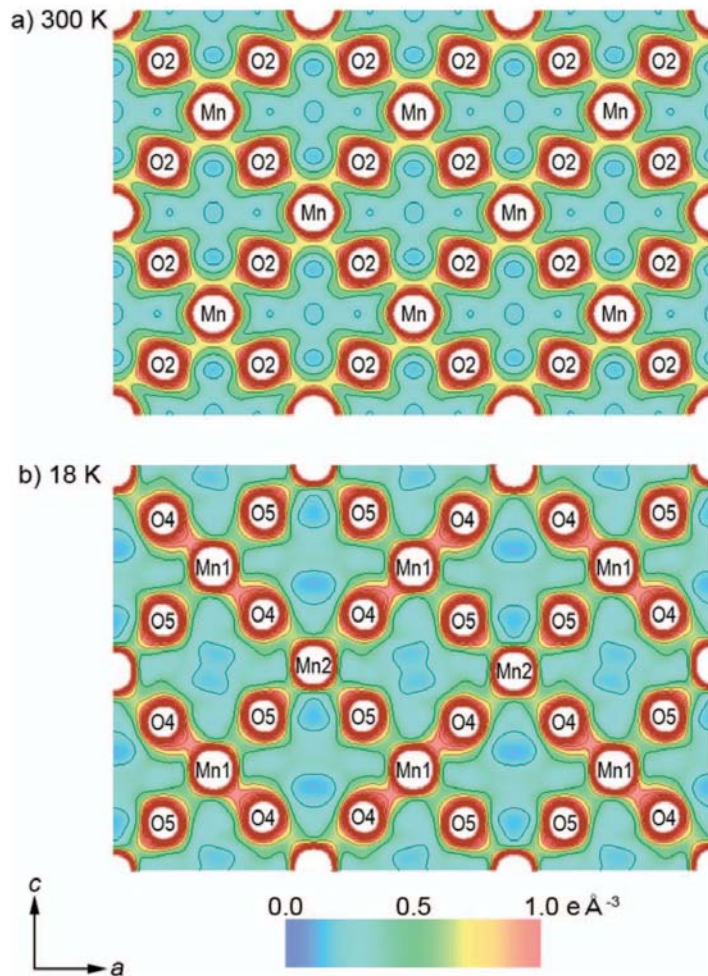

Figure 1-8 MEM charge density distribution in tetragonal of BaTiO$_3$; (a) (1 0 0) plane and (b) (2 0 0) plane. Contour lines are drawn at intervals of 0.2 e Å^{-3} from 0.4 e Å^{-3} to 2.0 e Å^{-3}.
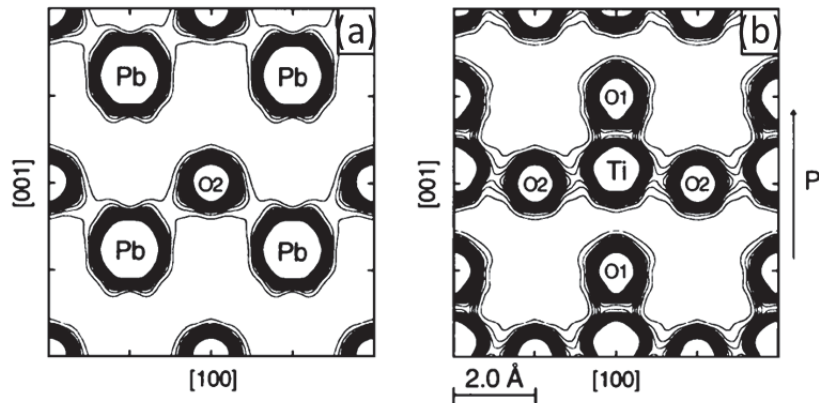
Figure 1-9 MEM charge density distribution in PbTiO$_3$ tetragonal; (a) (1 0 0) plane and (b) (2 0 0) plane. Contour lines are drawn at intervals of 0.2 e/Å^3 from 0.4 e Å^{-3} to 2.0 e Å^{-3}.

Besides, the MEM charge density study can also be used to study the charge

order or the orbital order. For example, the charge density distribution study has also been performed in the $Nd_{1-x}Sr_xMnO_3$ system to investigate the charge and orbital ordering. In the half-doping, charge ordering of Mn^{3+} and Mn^{4+} in $Nd_{1/2}Sr_{1/2}MnO_3$ is successfully visualized at 18 K. A zigzag pattern of the anisotropy charge density around Mn^{3+} sites were observed, which is owing to the $p_{x(y)}$-d_{x2-y2} hybridization of bonding electron as shown in Fig. 1-10.[42] Meanwhile, the charge density around Mn^{4+} sites is isotropic. At $x = 0.65$, charge ordering of Mn ions disappear, instead, an long-range ordering of $d_{3z^2-r^2}$ orbital appears in $Nd_{0.35}Sr_{0.65}MnO_3$ at low temperature($<T_N$). An anisotropic charge density distribution around Mn ions was clearly observed with a higher charge density in the shorter Mn-O1 bonds as shown in Fig. 1-11.[43]

Figure 1-10 MEM charge density distribution of $Nd_{1/2}Sr_{1/2}MnO_3$ on the (010) plane at

(a) 300 K and (b) 18 K.
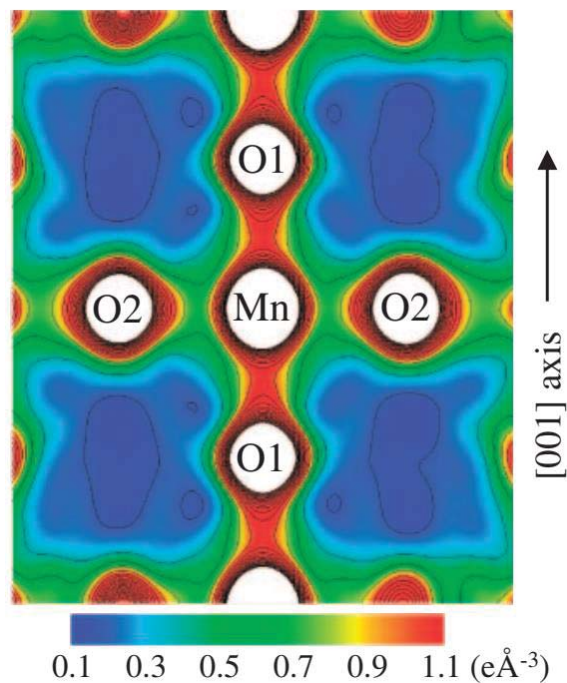
Figure 1-11 MEM charge density distribution of $Nd_{0.35}Sr_{0.65}MnO_3$ on the Mn–O1–O2 plane at 30 K.

On the other hand, the excellent counting statistics and the high angular resolution of SXRD data also enable us to visualize the electron charge density of light elements such as Li and H in the compounds with heavy elements at the same time.

1.6 BaBiO$_3$ and BaBiO$_{2.5}$

BaBiO$_3$, with a perovskite-type structure, has attracted extensive research interest after the superconductivity discovered at low temperatures in the doped solid solutions (Ba, K) (Pb, Bi) O$_3$. The superconductive oxide $BaPb_{1-x}Bi_xO_3$ was firstly found in 1975 as shown in Fig. 1-12,[44] $BaPb_{0.8}Bi_{0.2}O_3$ shows a transition temperature about 12 K accompanied with a low density of states around the Fermi

level. The doping the electronically inactive Ba donor sites induce the superconductivity in $Ba_{0.6}K_{0.4}BiO_3$ with a higher Tc about 30 K in 1988 as shown in Fig. 1-13.[45-47]
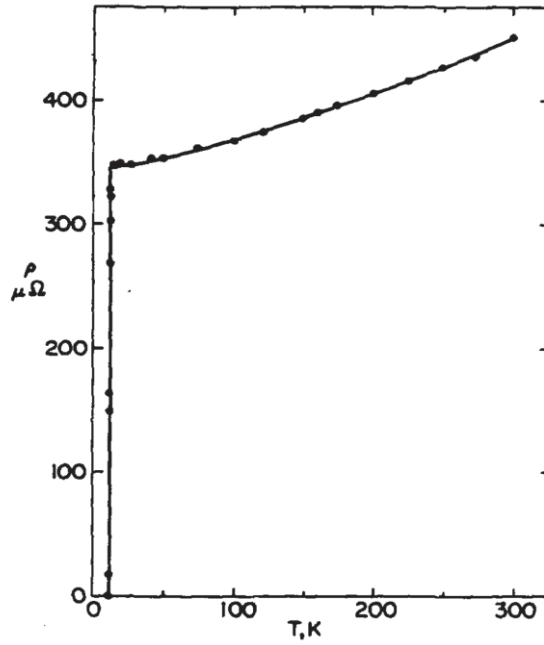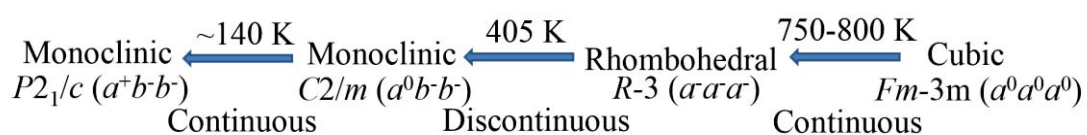

Figure 1-12 Eectrical resistivity with dependence of temperature of $BaPb_{0.8}Bi_{0.2}O_3$.
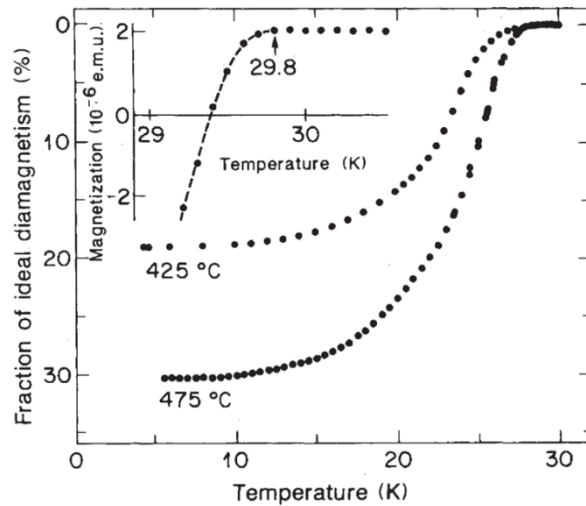
Figure 1-13 Temperature-dependent magnetization for $Ba_{0.6}K_{0.4}BiO_{3-x}$ samples decreasing the temperature with a magnetic field of 19 Oe. Inset shows enlarged region near Tc of the sample annealed at 475 °C in oxygen.

Additionally, BaBiO$_3$ is expected to be used in photocatalytic applications. BaBiO$_3$ serves as an efficient catalyst under visible light in water splitting reactions, carbon dioxide reduction, and the decomposition of various organic contaminants.[48-52] The high activity of BaBiO$_3$ is owing to the electron configuration of Bi ions and chemical bonding, which facilitate charge mobility and narrow the band gap. BaBiO$_3$ photocatalysts have inspired much attention owing to the special electronic structure consisting of orbital hybridization between O 2p and Bi 6s obtials. The 6s orbitals of Bi ions show the high dispersion, which encourages the reduction of the band gap and charge mobility.

Assuming that the valence state of Ba ions is Ba^{2+} in BaBiO$_3$, that of Bi ions should be Bi^{4+} to maintain charge neutrality. However, as a Bi ion is referred to as a valence skipper, it typically does not assume the Bi^{4+} valence state in compounds. Hence, Bi ions may exhibit charge disproportionality from the Bi^{4+} valence state to the Bi^{3+} and Bi^{5+} valence states. The typical chemical formula of oxide materials with a perovskite-type structure is denoted ABO$_3$, where A and B are occupied by cations. BaBiO$_3$ does not exhibit a B-site disordered simple perovskite-type structure, however, it is supposed to exhibit a B-site ordered double perovskite-type structure to occupy two different B sites for Bi^{3+} and Bi^{5+} ions with equal occupancy with the formula of Ba$_2$Bi^{3+}Bi^{5+}O$_6$. The charge order attributes the fact that BaBiO$_3$ is electrically a semiconductor.[53-56] This compound have been proved to undergo a successive structural phase transitions under lowing temperature from cubic ($Fm\overline{3}m$), rhombohedral ($R\overline{3}$), and monoclinic ($I2/m$) to monoclinic ($P2_1/n$) phases as shown in Fig.1-14.[57-60]

Monoclinic	~140 K	Monoclinic	405 K	Rhombohedral	750-800 K	Cubic
$P2_1/c$ ($a^+b^-b^-$)		$C2/m$ ($a^0b^-b^-$)		R-3 ($a^-a^-a^-$)		Fm-3m ($a^0a^0a^0$)
	Continuous		Discontinuous		Continuous	

Figure 1-14 Phase transition diagram of stoichiometric BaBiO₃.

BaBiO₃ undergoes several temperature dependent phase transitions accompanied with BiO₆ octahedral tilting. The charge ordered BaBiO₃ have four different phases. From cubic phase to rhombohedral phase and monoclinic to monoclinic phase, these two-phase transitions seem to adopt the second-order phase transition. In contrast, the phase transition between rhombohedral and monoclinic phase shows the discontinuous transition, that means the first-order phase transition. The detail of every crystal structure is shown below in Fig. 1-15.

Cubic $Fm\bar{3}m$ Rhombohedral $R\bar{3}$

Monoclinic $C2/m$ Monoclinic $P2_1/c$
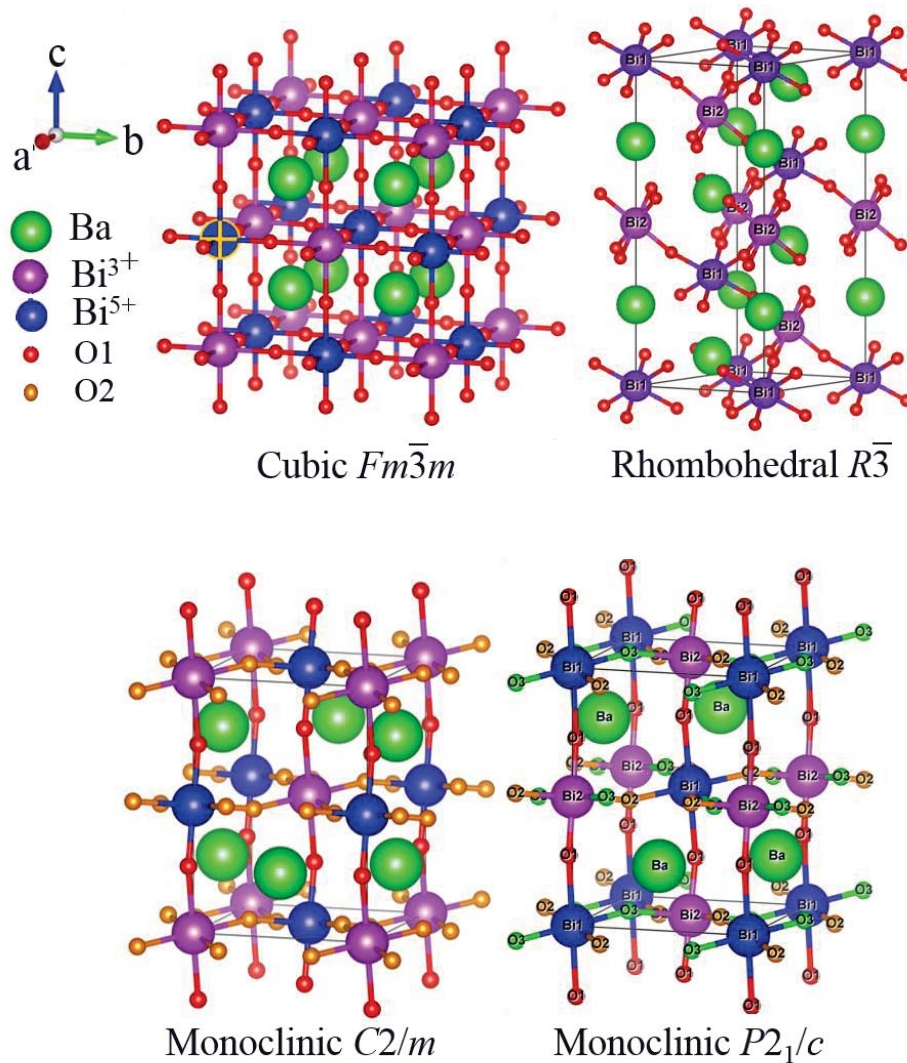
Figure 1-15 The crystal structure of BaBiO₃ at different phases.

Bismuth is one of the most studied ions existing in many different kinds of functional materials processing different local coordination environments, leading to the occurrence of large amount of intriguing properties such as the ferroelectricity, superconductivity and so on.[61-65] These functional materials seem to be strongly corelated to the lone pair of Bi^{3+} ions, which usually show the stereoactivity.[66-68] The Bi ions with various oxidation states can exhibit in many compounds, which rich the functional diversity. Among these Bi-containing compounds, perovskite $BaBiO_3$ has been widely investigated, which shows an octahedral of [$Bi^{3+}O_6$ and $Bi^{5+}O_6$] breathes out and in mode.[69-71] Generally, the modification of local coordination environments of cations in the network of crystal can emerge many interesting properties.

The modification of local oxygen coordination environments of cations in different oxides have been widely investigated. Through the part of oxygen atoms extraction, the phase transformation of structure can be achieved, which sometimes enable the apperance of many kinds of novel oxides with unexpected physical properties different from those of corresponding oxygen rich parent compounds.[72-82] One of the most well-known samples is the transformation from perovskite structure $SrFeO_3$ to layered structure $SrFeO_2$, which shows the dramatic changes in crystal lattice and magnetic spins.

1.7 Purposes

$BaBiO_3$ as the parent sample of the superconductive doped solid solution have already been investigated in the crystal structure and phase transition using neutron diffraction. We have already learned that is one of the best papers on the structure analysis. However, we have been supposing that if we can analyze the crystal structure precisely by using synchrotron radiation X-ray diffraction (SXRD), in

addition, we can provide the experimental direct evidence on the chemical bonding between atoms. The MEM/Rietveld analysis combined with SXRD enabled us to visualize the electron charge density distribution around the Bi ions, hence, we could directly observe the charge order of Bi^{3+} and Bi^{5+} in $BaBiO_3$ from the difference in the ionic radii. The nature of chemical bonds could be also observed to summarize them. We believe that we are the first ever to experimentally observe the electron charge density distributions accurately in $BaBiO_3$. Our study enriches the understanding of the structural characteristics, charge order, and chemical bonding nature of $BaBiO_3$ in a viewpoint of electron charge density distribution, which may provide avenues for developing low dimensional $BaBiO_3$-derived functional materials such as superconductors.

Since it is difficult to prepare the stoichiometry oxygen failing compounds in a well-controlled behavior, the synthesis of $BaBiO_3$-derived phases (such as $BaBiO_{2.5}$) by reductive method is challenging. Previous work often resulted in obtaining mixed phases with impurities, that usually made crystal structural analysis and property characterization extremely difficult. Besides, the structure and physical properties of the $BaBiO_{2.5}$ are still poorly investigated until now. Encouraged by the discovery of superconductivity in the doped solid solution of $BaBiO_3$, we suggested that there may be new physical characteristics in its reductive phase, which may have an interesting Bi local coordination geometry and unusual chemical bonding nature.

Chapter 2
Experimental method
2.1 Synchrotron radiation X-ray diffraction

Synchrotron-radiation light source refers to a physical device that generates synchrotron radiation. It is a type of high-performance strong light source that generates synchrotron radiation when relativistic electrons (or positrons) deflect in a

magnetic field as shown in Fig. 2-1. The emergence of electronic synchrotrons, especially the development of electronic storage rings, has promoted the widespread application of synchrotron radiation.
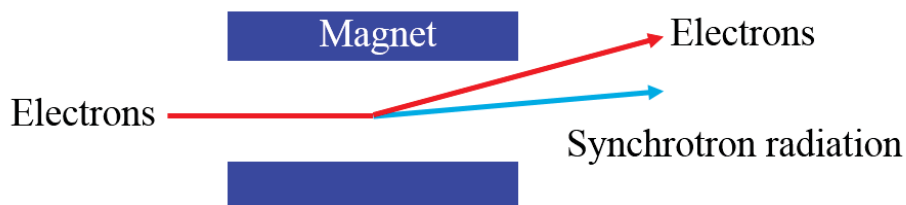
Figure 2-1 The generation of synchrotron radiation. When electrons make a motion in a magnetic field, it emits synchrotron radiation along the tangent direction of the deflection orbit.

The synchrotron-radiation light source has experienced three generations of development, and its main body is an electronic storage ring. The early research of synchrotron radiation was carried out on the electron synchrotron. The electronic storage ring of the first generation of synchrotron radiation light source was designed for high-energy physics experiments. It only used the parasitic synchrotron radiation from the deflection magnet, so it was also called "combined light source". The first storage ring installed in a synchrotron-radiation light source was at the Synchrotron Radiation Center of Tantalus in 1968. The electron storage ring of the second-generation synchrotron radiation light source is specially designed for the use of synchrotron radiation, which mainly draws synchrotron radiation light from the deflection magnet. The device has been optimized to make the electron beam emittance much smaller than that of the second generation, so the brightness of synchrotron radiation is greatly improved, and high-brightness, partially coherent quasi-monochromatic light can be extracted from inserts such as undulators. The third-generation synchrotron-radiation light source can be further subdivided into high-energy light sources, medium-energy light sources, and low-energy light sources according to the differences in photon energy coverage and electron beam energy in the electron storage ring. With its excellent light quality and irreplaceable role, the

third-generation synchrotron-radiation light source has become the best light source for basic research and high-tech development and application research in many disciplines today. The schematic of a third-generation synchrotron is shown in Fig. 2-2.[83] In the future, the fourth-generation light sources are under development that will produce ultra-brilliant and pulsed time-resolution X-rays for extremely experimental demanding.
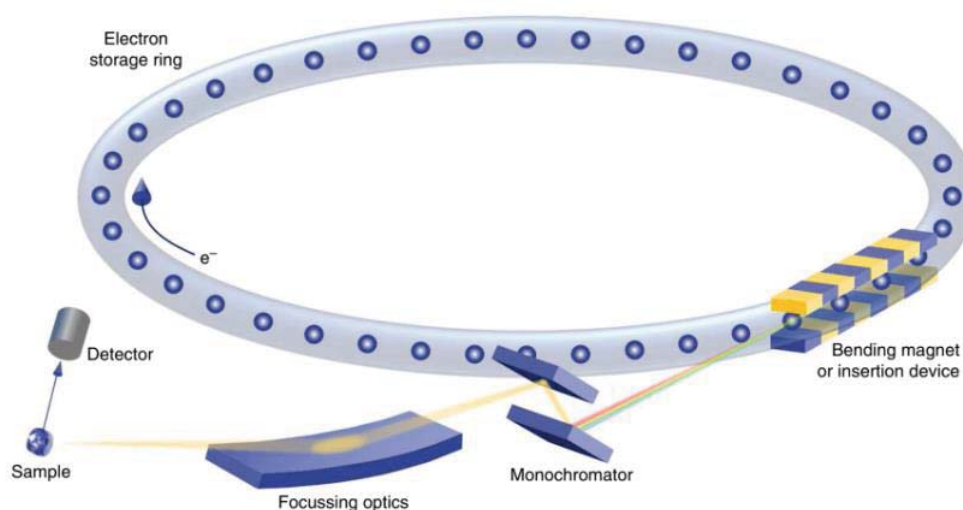
Figure 2-2 Schematic of a third-generation synchrotron.

The synchrotron radiation presents several characteristics. The synchrotron radiation light has a wide wavelength band. The wavelength coverage of synchrotron radiation light is large, and it has a continuous spectrum from far infrared, visible light, ultraviolet to X-ray range, and it can obtain a specific wavelength of light according to the needs of users. The synchrotron radiation light shows the high collimation. The emission of synchrotron radiation light is concentrated in a very narrow cone centered on the direction of electron motion, with a very small angle, almost parallel beam, comparable to laser. The synchrotron radiation light presents the high polarization. The synchrotron radiation light from the deflection magnet is completely linearly polarized on the electron orbit plane. In addition, people can obtain the light of any polarization state using some specially designed insert. The synchrotron radiation light is a kind of light with high purity and brightness. Since the synchrotron radiation

light is produced in the ultra-high vacuum without any pollution caused by any impurities. it is very pure light. The synchrotron radiation light source provides a high-energy light with small wavelength. The X-ray brightness of the third-generation synchrotron radiation light source is hundreds of billions of times that of the normal X-ray machine. The synchrotron radiation light can be a narrow pulse light with excellent pulse time structure. Its width is adjustable from 10^{-11} to 10^{-8} seconds. The interval between pulses is tens of nanoseconds to microseconds. This characteristic is very useful for the study of "change process", such as chemical reaction process, life process, material structure change process and environmental pollution micro process. In addition, the synchrotron radiation has some other unique and excellent properties such as high stability, high flux, micro beam diameter, quasi coherence, etc.
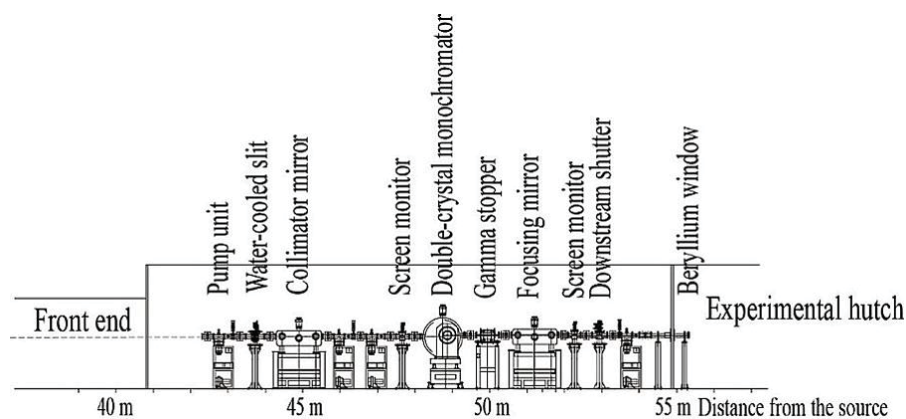
2.2 SPring-8 BL02B2

All our experiments of X-ray diffraction data were all collected in Spring-8 BL02B2 beamlines. SPring-8 is one of largest three-generation synchrotron radiation facility in the world until now as shown in Fig. 2-3. It is located at Harima Science Park City, Hyogo Prefecture, Japan. The wavelength of the emitted radiation has a wide energy range from vacuum ultraviolet rays to hard X-rays with the highest intensity in the world. Furthermore, the high energy γ-ray can be achieved with the energy from 1.5 to 2.9 GeV, meanwhile, the infrared rays can also be obtained.

**Figure 2-3** The bird eye view of the synchrotron radiation facility Spring-8.

Spring-8 can provide the high-energy synchrotron radiation that can be used in many different scientific fields, including observing the mobility of chemical reactions, structural analysis, life science, medicine, industry and so on. Figure 2-3 shows the bird eye view of SPring-8. There are several systems included in the synchrotron-radiation Spring-8. During the whole process of generation of synchrotron radiation, firstly, the electron gun generates an electron beam. Then, the electron beam can be accelerated to about 1 GeV by the linear accelerator. In order to obtain much higher energy electrons with 8 GeV, further accelerate process can be achieved in the synchrotron. The storage ring plays the important role in storing the high energy electrons. Then, the radiation light is generated using the polarization electromagnet combined with the insertion light source. The emitted light is finally guided to every different hatch installed outside the storage ring all through the beam line, which can be used in various experiments for different purposes.

**Figure 2-4** Schematic view of beamline of BL02B2 in Spring-8.

SPring-8 BL02B2 is a beam line for powder diffraction using high-energy synchrotron radiation as shown in Fig. 2-4.[84] The beamline is designed to perform several scientific studies. One hand, it can analysis the crystal structure using the high-resolution X-ray diffraction data. Based on the precis structure analysis, the charge density of the polycrystal sample structures can be obtained that are related to the properties of functional materials. Structure phase transitions can also be clearly determined. On the other hand, Ab initio structure determination can also be performed. Besides the polycrystal samples, the structure analysis of thin films can also be obtained.

Figure 2-5 shows a schematic figure of the optical system installed in BL02B2 beamline.[84] The optical system is used in BL02B2 beamline, which is mainly composed of a curved mirror and a double Si crystal monochromator. The Mirrors are designed for the purpose of removing the unnecessary harmonics, there are three sets of options corresponding to different demand of the energy of synchrotron radiation. Demand of lower than 15.5 keV energy, Si mirror is preferred. Ni mirror can be used in the region from 15.5 keV to 28.2 keV energy, and Pt mirror is required for higher energy than 28.3 keV. The double Si crystal monochromator is installed to improve the parallelism of X-ray and energy resolution, and the Si crystal with parallel (111) plane is used as a standard. The BL02B2 beamline can provide high energy X-ray with a wide energy region from 12 to 37 keV. The energy resolution $\Delta E/E$ is about 2×10^{-4}.

29
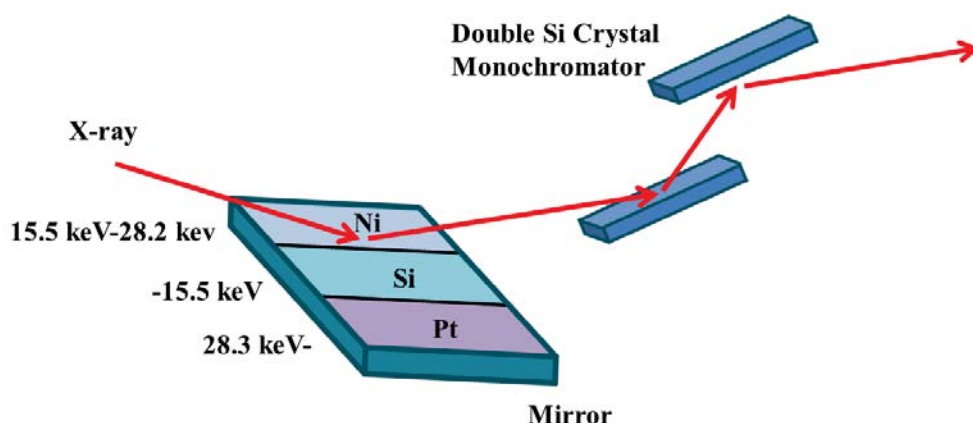
Figure 2-5 The schematic of the optical system in SPring-8 BL02B2.

In the experiment hatch of BL02B2 beamline, a large Debye-Scherrer camera is installed. Figure 2-6 shows a schematic view and photograph of the large Debye-Scherrer camera.[85,86] A curved imaging plate (IP) camera and a semiconductor detector multi-connected diffractometer (MYTHEN) camera on the 2θ axis are installed to collect diffraction pattern. In the measurement, the sample sealed in the glass or quartz capillary is fixed on the ω-axis exposed in the X-ray. During exposure process, the sample keep rotating around the ω-axis to obtain the homogenous diffraction intensity on Debye rings, which balances the influences of inhomogeneous particle size distribution in the sample. This rotating measure guarantees the high quality of powder diffraction pattern. To make the sample located at center, the 5-axises goniometer head is used, so that the sample does not move during the rotation around the ω-axis. When the phase transition is investigated, different temperature diffraction data are required. Hence, a temperature controlling system is installed which is controlled using flowing gas. Below room temperature from 15 - 300 K, He gas recycling type refrigerator is capable, N_2 gas blowing device can be used in measurement at a low temperature of 90 - 300 K. Higher than room temperature, N_2 gas is heated when measurement at a high temperature of 300 - 1100 K is performed. In our measurement, the IP and MYTHEN detector were both used, and the temperature was controlled using a low temperature N_2 gas blowing device.
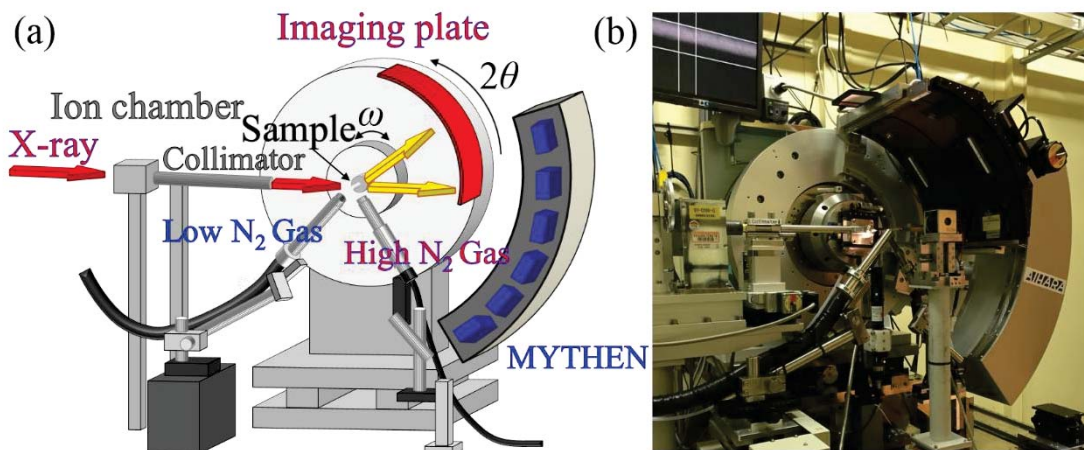
Figure 2-6 The (a) schematic view and (b) photograph of the large Debye-Scherrer camera installed in SPring-8 BL02B2.

MYTHEN detectors have six one-dimensional semiconductor detectors manufactured by DECTRIS company, that are installed at multiple 2θ-axes. In the measurement process, there are two kinds of collecting modes that can be used. One is the double-step mode. The six detectors are aligned at intervals of one detector, and a series of data can be obtained by measuring from the reference position and from the reference position by one detector and measuring at the same time. The other one is the single-step mode, which is usually used in the measurement only a certain angular range data needed. The measurement time of this mode generally is shortened compared with double-step mode, which is owing to no displacement of the detectors through matching the position of the detector at the needed angular range.

The IP data can be obtained using the imagine plate, which is then read through an IP reader. People can directly obtain the diffraction ring on the IP, then we need to transform this diffraction ring into one-dimensional pattern. However, compared with the MYTHEN camera, the diffraction pattern can be directly obtained with one-dimensional data, and the data of the diffraction pattern can be obtained much easier with shorter diffraction time. Besides, the MYTHEN diffraction angle resolution is higher than that of IP, it is possible to combine the sweeping temperature

measurement that is usually used in the determination of phase transition by observing the absolute change in peak position while changing the temperature. it can collect even a very small intensity of diffraction, therefore, the background on the low angle side will become large. In contrast, the IP camera detects only the intensity higher than a certain value, the background is much smaller than the MYTHEN data, and the intensity of signal to noise ratio is much better. Hence, IP data is more suitable for the charge density study or full-pattern Rietveld refinement owing to the better background.

2.3 Sample preparation

First, using the solid-state heating reaction method, the parent polycrystalline $BaBiO_3$ sample was successfully prepared. The starting powders were thoroughly ground to form a homogeneous fine powder consisting of $Ba(NO_3)_2$ (Aladdin., 99.99%) and Bi_2O_3 (Aladdin., 99.99%) powder with stoichiometric amounts. Then the starting powder was then heated at 600 °C for 24 hours. After the first heating process, the obtained powder was ground again. Then second heating processs is performed under 800 °C for 8 h in air. After that, the successfully obtained $BaBiO_3$ sample was slowly cooled to the room temperature.

Second, the parent $BaBiO_3$ sample was then heated at different temperature for 5 h in flowing N_2 gas atmosphere placed in the ceramic containers. The heating and cooling process are at the rates of 10 and 5°C/min, respectively. Several temperatures were used in the heating process of 600, 700, 800 and 900 °C. The obtained $BaBiO_{2.5}$ samples were found to be pure under 800 °C. The $BaBiO_{2.5}$ samples are extremely sensitive to air, where oxidation can occur. Hence, the $BaBiO_{2.5}$ samples were stored in a glovebox with N_2 gas atmosphere.
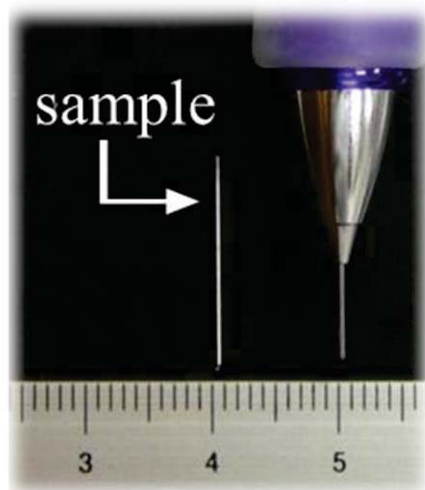
The polycrystal samples are sealed into the capillary with a small inner diameter 0.1 or 0.2 mm. The small size of capillary will almost eliminate the influence on the diffraction data. There are several kinds of capillary aiming at different temperature region. Above 500 K, a quartz capillary is suitable for the measurement. Below that, a boro glass capillary is acceptable owing to the low melting temperature point. However, the influence of boro glass capillary is much smaller than the quartz capillary. People need to aware that the absorption of these two kinds of capillary is small enough to ignore in the experiments.

2.4 Experiment condition

In the research work of $BaBiO_3$, all the powder diffraction pattern was collected using the apparatus mentioned above. Electron charge density studies were performed at the BL02B2 powder X-ray diffraction beamline in SPring-8 using a large Debye–Scherrer camera. High energy X-rays with a short wavelength of 0.414005(1) Å (30 keV) were used. One may pay attention to the decision of synchrotron radiation energy in the experiment, which should be slightly higher than the K edge absorption energy of the elements involved in the compounds. The powder sample was then sealed in a quartz capillary of 0.1 mm internal diameter for the high temperature

measurements, meanwhile, the boro glass capillary of 0.1 mm inter diameter was used for the low temperature measurements. The SXRD patterns were measured in the transmission geometry. If the sample contains heavy elements such as Bi, the absorption effect in X-ray diffraction must be considered. However, in this experiment, the absorption effect was negligibly small because high-energy X-rays were used. The phase transitions were investigated during temperature sweeps from 100 to 1100 K with a every 5 K interval and heating rate of 20 K/min using the MYTHEN detectors.[86] Precise SXRD data with good counting statistics for electron charge density studies were collected at 900, 600, 300, and 100 K in each phase using an imaging plate IP. The temperatures can be controlled within 1 K by the N_2 gas flow temperature controlling system. The crystal structure and electron charge density distributions were determined by using the MEM/Rietveld method. The MEM analyses were performed with the unit cell divided into small voxels. The volume of one voxel corresponded to approximately $0.05 \times 0.05 \times 0.05$ Å^3. The MEM analysis was performed using the program package ENIGMA.[87] The crystal structure and MEM electron charge density distribution maps were plotted using the program VESTA.[88]

The Vienna Ab initio Simulation Package (VASP) was used in First-principles calculations.[89,90] The projector augmented wave method was applied in the treatment of Electron–ion interactions.[91,92] Using the Perdew–Burke–Ernzerhof function, the generalized gradient approximation calculation of exchange-correlation interactions was modified. The valence electrons included Ba $5s^2\ 5p^6\ 6s^2$, Bi $5d^{10}\ 6s^2\ 6p^3$, and O $2s^2\ 2p^4$ in the calculation. In all calculations, the plane-wave kinetic energy cutoff is 500 eV, and k-point spacing for Brillouin zone sampling is 0.25 Å^{-1}. The crystal structures were determined by relaxing the structure, where the magnitudes of all forces worked on the atoms should be less than 0.01 eV/Å.

In the experiment of BaBiO$_{2.5}$ samples, the TG measurements were carried out on a Netzsch STA 449C thermal analyzer, the BaBiO$_{2.5}$ powder samples were heated under an oxygen atmosphere with a flow rate of 40 ml min^{-1}, which will enable us to

determine the amount of oxygen in the obtained $BaBiO_{2.5}$. The heating treatment was performed from 30 to 800 °C with a rate of 5 K min^{-1}. The ordinary powder XRD measurements with lower resolution were performed using a desktop diffractometer (D2 PHASER, Bruker, λ= 1.54056 Å) under 30 kV and 10 mA radiation. In the experiment, the $BaBiO_{2.5}$ samples were carefully sealed in two pieces of tapes to avoid the pollution of air. The high-resolution SXRD data were collected on an imaging plate using a large Debye–Scherrer camera at SPring-8 BL02B2 beamline. The wavelength used in the experiment is stabled at 0.414096(1) Å. The $BaBiO_{2.5}$ samples used in the SXRD measurement were sealed in the Hilgenberg glass capillaries under lower temperature below 400 K with an inner diameter of 0.2 mm. In order to avoid the occurrence of preferred orientation in diffraction pattern, the rotating of sample was necessary during the measurement to average the intensity of diffraction pattern. The SXRD pattern of $BaBiO_{2.5}$ was collected in the 2θ range from 3.0° to 70.0° (resolution of d >0.36 Å in the d spacing). The low-temperature SXRD data of $BaBiO_{2.5}$ was collected using the low temperature N_2 gas flow controlling system with 1 K resolution. Using the MEM/Rietveld method, the crystal structure and electron charge density distributions of $BaBiO_{2.5}$ were obtained. The 148 × 152 × 120 pixels of unit cell were used in the MEM electron charge density distribution calculation of $BaBiO_{2.5}$. The program VESTA was used in the drawing of the crystal structure and MEM electron density distribution. The $BaBiO_{2.5}$ samples were sealed in two pieces of quartz glasses in the collection experiments of PL, Raman scattering, and absorption spectra. The emission and excitation spectra of PL experiments and at room-temperature were collected using a FLS 980 spectrofluorometer (Edinburgh Instruments Ltd.). The NIR PL spectra under the 658 nm laser diode at different temperature were collected using an electrically cooled PMT (Hamamatsu, H10330-75) equipment and analyzed by the monochromator (Horiba, iHR550). The different excitation power densities from 0.05 to 1.2 W/cm^2 of 658 nm laser were used in the PL measurements. The 658 nm laser light was the third harmonic of a Nd:YAG laser pumped by an optical parametric oscillator. The Raman scattering measurements were performed under a 633 nm laser line with a power of 5 mW using

a micro-Raman spectrometer (Horiba Jobin Yvon, Labram HR 800). The backscattered radiation was collected by microscope optics and scattered by a monochromator installed with a holographic grating. The slit and pinhole sizes are 100 and 300 mm, respectively. The UV-vis-NIR spectroscope (Cary 5000, Agilent) with an integrating sphere was used in collecting of diffuse reflectance spectra of the $BaBiO_{2.5}$. The Kubelka-Munk transformation was used to convert the obtained reflectance spectra into the pseudo-absorbance spectra. At the 1W2B beam line located at the Beijing Synchrotron Radiation Facility, the X-ray absorption spectra were collected at the Bi L_{III} edge of $BaBiO_{2.5}$, Bi_2O_3 and Bi. All spectra were collected at room temperature. The Bi and Bi_2O_3 powders were used as the references compared with $BaBiO_{2.5}$ sample. The IFEFFIT software package was used in the analyzing of the XAFS data.[89] The FEFF6 computational package was used in simulating the scattering amplitudes of Bi-O, Bi-Bi, and Bi-Ba paths used in fitting the EXAFS spectrum of $BaBiO_{2.5}$, originating from the experiment structure result. Eight single scattering paths were included in the calculation model. The EXAFS fitting results showed the 0.8 of amplitude reduction factor S_0^2, and Bi_2O_3 sample was used as a reference sample. The fitting was carried out in R space from 1 to 4 Å, on the FT of the k^3-weighted EXAFS.

The projector augmented wave (PAW) potentials in the VASP code was used in spin polarized density functional theory (DFT) calculations.[90] A single point at the generalized gradient approximation (GGA) lattice geometry was used in the Hybrid DFT calculation. The structure used in the calculation is modified using the GGA scheme with Perdew-Burke-Ernzerhof (PBE).[91] The 450 eV of the kinetic energy cutoff for the plane-wave basis was determined. The Monkhorst-Pack k-point mesh with $5 \times 5 \times 5$ was used to take sample in the Brillouin zone. When the maximum forces were less than 0.01 eV·Å^{-1} and the total energy was converged to 1×10^{-4} eV/atom, the ions were relaxed. The band structure and density of state (DOS) of $BaBiO_{2.5}$ were analyzed by the hybrid exchange and correlation functional of Heyd-Scuseria-Ernzerhof (HSE06).[92] Considering the fact of the weak chemical

bonding among the crystal structures of $BaBiO_{2.5}$, we used a damped van der Waals (optB86b-vdW functional) correction in the calculation.

Chapter 3
Analysis method

3.1 Rietveld analysis

In the early 1969 years, Rietveld reported his original research to analyze the neutron powder diffraction data.[93] Since then, the Rietveld refinement has been recognized as a powerful method to analyze the crystal structure. In the Rietveld analysis, the parameter of profile and cell are carefully refined based on a given structure model that is similar to the structure of your compound, meanwhile, the diffraction optics effects, and instrumental factors are also considered. After years of development, it has been wildly used in the analysis of crystal structure nowadays using the characteristic XRD or SXRD, and time-of-fight (TOF) neutron diffraction from the spallation neutron source.

The Rietveld refinement results of the diffractions can simultaneously provide many kinds of information including the lattice constants, atomic position, thermal vibration, vacancy and so on. Based on these factors, lattice distortion and crystallite size can be discussed. Meanwhile, the mass ratio of each phase in a mixture can be determined by the ratio of scattering factors. Rietveld analysis is suitable for the crystal structure analysis with the premise that people understand the structure of the target sample. If the crystal structure of the sample is unknown, it is necessary to analyze the crystal structure using maybe the Transmission Electron Microscopes.

In the Rietveld analysis, the diffraction pattern calculated based on an approximate structure model, then, measured diffraction pattern should match the calculated diffraction pattern as closely as possible. After that, the structure parameters can be optimized through eliminating the model deviation. The diffraction

data measured from the X-ray diffraction experiment are fitted using a theoretical function by nolinear-least-squares methods. The error sum of the squares can be obtained using the following function in the Rietveld refinement.

$$S(x) = \sum_i w_i [y_i - f_i(x)]^2 \qquad (3\text{-}1)$$

The $S(x)$ can be minimized during the optimization with the variable parameter x. Here y_i (i = 1, 2, 3...) displays the observed diffraction intensity, and w_i ($=1/y_i$) corresponds to the statistical weight at the ith measurement point. $f_i(x) = f(2\theta_i; x_1, x_2, x_3,...)$, which is the calculated diffraction intensity. The calculated diffraction intensity has a function shown below.

$$f_i(x) = s S_R(\theta_i) A(\theta_i) D(\theta_i) \sum_K m_K |F_K|^2 P_K L(\theta_K) G(\Delta 2\theta_{iK}) + y_b(2\theta_i) \qquad (3\text{-}2)$$

The scale factor refers to s. $S_R(\theta_i)$ is related to the roughness effect of the surface at low scattering angles in the Bragg-Brentano X-ray diffraction geometry. $A(\theta_i)$ shows an absorption in the Debye-Scherrer geometry, $D(\theta_i)$ is related to the effect of a width of divergence slit in the Bragg-Brentano X-ray diffraction geometry. K shows the Miller index of the reflection. m_K refers to the multiple factor, F_K represents the structure factor, P_K shows a preferred orientation, $L(\theta_K)$ refers to the Lorentz polarization factor, and $G(\Delta 2\theta_{iK})$ is a reflection profile factor. $y_b(2\theta_i)$ shows the background intensity at ith point.

Generally, R factor acts as an index for evaluating the Rietveld analysis results. There are several kinds of R factors involved in this paper, such as R_{WP}, R_I, and R_F. The definition is shown below.

$$R_{WP} = \left\{ \sum_i w_i [y_i - f_i(x)]^2 \middle/ \sum_i w_i y_i^2 \right\}^{\frac{1}{2}}, \qquad (3\text{-}3)$$

$$R_I = \sum_H |I'_{obs}(H) - I_{cal}(H)| \middle/ \sum_H I'_{obs}(H), \qquad (3\text{-}4)$$

$$R_F = \sum_H ||F'_{obs}(H)| - |F_{cal}(H)|| \middle/ \sum_H |F'_{obs}(H)|, \qquad (3\text{-}5)$$

R_{WP} shows a weighted reliability factor of fitting result between the whole

experimental diffraction with the calculated diffraction pattern, R_I shows a reliability factors comparing the calculated diffraction intensity and observed diffraction intensity, and R_F evaluates the difference of the crystal structure factor between observed and calculated diffraction pattern. In these functions, $I'_{obs}(\boldsymbol{H})$ and $I_{cal}(\boldsymbol{H})$ refer to the observed and calculated integrated intensity of Bragg reflections, respectively, and $F'_{obs}(\boldsymbol{H})$ refers to an estimated structure fator of observed diffraction. The variable parameter $\boldsymbol{H}$ refers to (h, k, l). If these reliability factors are smaller than 5%, which means the calculated crystal structure is consistent with the assumed structural model, it can be believed that reliable crystal structure are obtained.

In the Rietveld refinement, apart from the fitting of lattice parameter, atom position and thermal vibration, fitting of diffraction profile is also necessary. The half-value width of profiles in the diffraction pattern is fitted using a half-width function. The half-width function defines the half width W of the profile in the calculated diffraction based on the structural model. The definition of the function is shown below.

$$W = \left(u + v \times \tan\theta + w \times \tan^2\theta + p \times \sec^2\theta \right)^{\frac{1}{2}} \tag{3-6}$$

where u, v, w, and p factors describe the profile of calculated diffraction pattern.

3.2 Maximum entropy method (MEM)

The Maximum Entropy Method (MEM) is a model estimation method based on the information theory.[94,95] In early 1967 year, it was proposed by J. P. Burg to analysis the earthquake wave.[96] The MEM is recognized as the most potential method to deal with the limited number of information. MEM has been successfully used in various data analysis in many different fields. Nowadays, MEM has been widely applied in a wide range of spectral analysis and image processing techniques.

In MEM analysis, we can obtain a solution that maximizes information entropy under a constraint condition based on the information obtained in the experiment. In

this paper, we used MEM method to determine the electron charge density distribution. During the process of determination of electron charge density distribution, the whole structure factor of the crystal structure can be estimated beyond the limitation of the experimental diffraction whose structure factor is usually zero without diffraction intensity. The MEM charge density study can only observe the outer shell electrons distribution, such as localized bound electrons and conduction electrons rather than inner shell electrons. These outer shell electrons contribute greatly to the diffraction intensity of low angle region, whose distribution is spatially existing far away from the nucleus. MEM method is more suitable for polycrystal samples rather than single crystal samples owing to its extinction effect in the low angle region that cannot be ignored. The MEM analysis can provide the direct visualization of chemical bonds between atoms. The attenuation effect in the low angle region can be avoided in the angular dispersion type powder diffraction, and the possible existed overlap of reflection in low angle region can also be ignored. The first charge density study using MEM is performed for Si. Figure 3-1 shows the comparison between structural factors of calculated MEM electron density analysis of Si and the observed experimental structural factors.[97,98] The structural factor obtained by MEM electron density analysis shows a good agreement with the observed structural factor. A smooth curve of MEM structural factor is observed extended to the high angle region. In contrast, the observed structural factor can only be observed with $\sin\theta/\lambda < 0.8$ Å^{-1} owing to the high abortion.
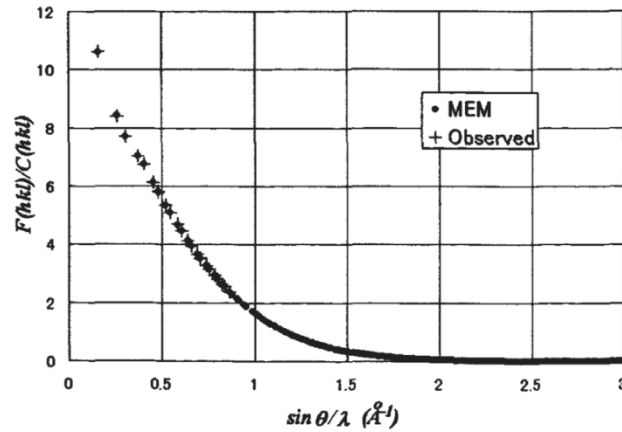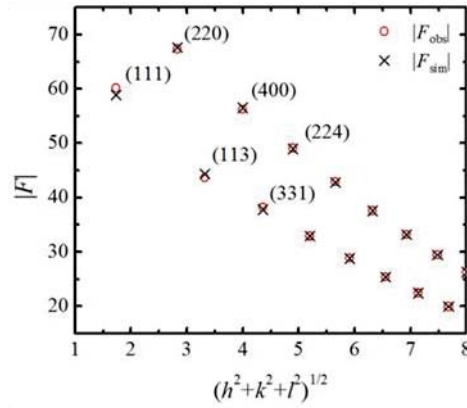
Figure 3-1 Structural factors and observed structural factors calculated by MEM electron density analysis of Si. Although the observed structural factor is only $\sin\theta/\lambda = 0.8$ Å^{-1}, structural factors can be predicted up to the high angle region by MEM analysis.

The MEM analysis of Si gives the detailed structural information including the bonding characteristics between atoms. The two-dimensional electron charge density distribution of the Si (110) plane using the ordinary direct Fourier method and MEM is shown in Fig. 3-2.[99] Both electron charge density distributions can be obtained based on the same experimental measured structural factor with a range of $d > 0.58$ Å ($Q < 0.86$ Å^{-1}). It is obvious that electron density distribution around the atomic position can be obtained using the conventional direct Fourier method, however, the electron charge density distribution between atoms such as the bonding electrons appears to be irregular, which is because of the defect of truncation effect. Generally, to observe the electron charge density distribution in the real space using conventional direct Fourier method, the whole inverse space is required including the high Q data, which usually mismatch the experimental result.
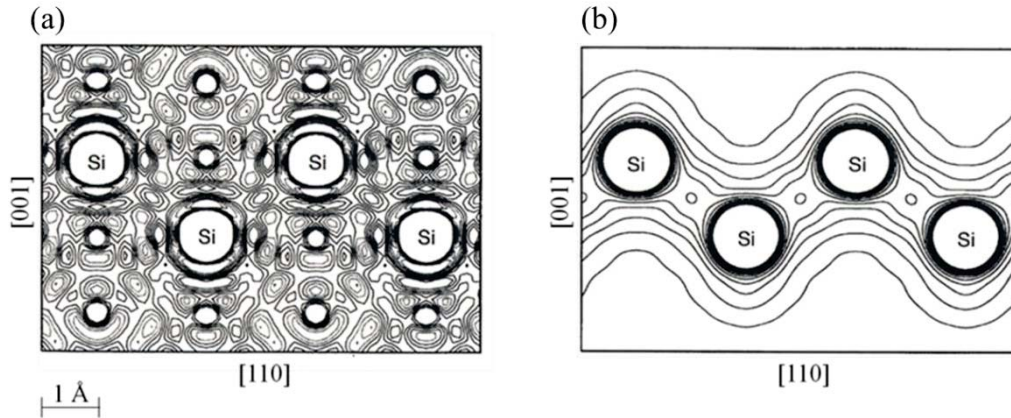
Figure 3-2 Difference in Si electron density distribution due to different analysis method; (a) the conventional direct Fourier method (contour lines -3.0 to 3.0 $e\text{Å}^{-3}$, with step 0.3 $e\text{Å}^{-3}$), (b) MEM electron density analysis (contour lines 0.1 to 2.0 $e\text{Å}^{-3}$, with step 0.1 $e\text{Å}^{-3}$). (110) plane electron density distribution. It has been analyzed using structural factors of the same range ($d > 0.58$ Å) measured by X-ray diffraction experiments.

In contrast, the MEM can clearly obtain not only the electron charge density distribution around atoms but also the existence of covalent bonds between Si atoms. The overlap of the electron charge density is directly observed. This is because MEM can successfully estimate the whole structural factor including high Q region which cannot be actually experimental measured. Hence, MEM method has a good advantage in analysis of the electrons density distribution of bonds based on the finite number of structural factors.

Figure 3-3 Structure structural factor of Si including the observed structural factor F_{obs} and calculated structure factor F_{sim} by the *Pendellosung* Method. Si is assumed to be a complete ion of 4+ valence state. F_{obs} and F_{sim} have slight differences in low order diffraction.[99]

Besides, the electron density distribution highly depend on the range of Q. Figure 3-3 shows a comparison between the experimental structure factor F_{obs} used in Fig. 3-2 and the calculated structural factor F_{sim} using the *Pendellosung* Method.[100] In the range where Q is large with a larger diffraction index, the calculated F_{sim} structural factors almost show no deviation from the measured F_{obs} structural factors. However, it should be understood that the difference of structure factor is much larger in the small Q range. This is owing to the information of the outer shell electrons and bound electrons included in the small Q range. As a consequence, to investigate the charge density distribution in the covalent bonding, the structural factors of low Q region should be carefully be estimated.

On the other hand, as already mentioned above, the Fourier transform shows a disadvantage in structure factor analysis of high Q data is. Q is derived from the Bragg's diffraction equation.

$$2d \sin\theta = \lambda, \tag{3-7}$$

$$Q = 4\pi \sin\theta / \lambda = 2\pi/d. \tag{3-8}$$

The high Q data contain a smaller d value, which will give us more detail of the electron charge density distribution in spatial crystal structure. In a sense, the parameter d can be used to measure the resolution of the crystal space. In MEM

analysis, the structure factor of high Q region is necessary, otherwise, an error of structure factor estimation may occur in the calculation. So high resolution of diffraction data with a wide-angle range is needed. However, in the experiments of X-ray diffraction, atomic scatterings and thermal vibration will sharply reduce the intensity in the high Q angle region, the statistical precision of high Q data is generally poor. As a consequence, the analysis result might be incorrect. In order to get a precise analysis results, it is obvious that the statistical accuracy of experimental observed structure F_{obs} should be as high as possible in a wide Q range.

In the case of X-rays diffractions, considering the electron density distribution of the unit lattice to be one whole scatterer, the structural factor can be defined using the following function.

$$F(H) = V \int \rho(xyz)e^{-2\pi i(hx+ky+lz)}dxdydz \tag{3-7}$$

The entropy can be defined as,

$$S = -\sum_r \rho'(r)\ln\frac{\rho'(r)}{\rho_0'(r)} . \tag{3-8}$$

Here, $r = (x, y, z)$.

$$\rho'(r) = \rho(r)\Big/\int \rho(r)dr , \tag{3-9}$$

$$\rho_0'(r) = \rho_0(r)\Big/\int \rho_0(r)dr , \tag{3-10}$$

where $\rho(r)$ is the electron density at a certain pixel r, and $\rho_0(r)$ is the electron density in a reference state. Here we introduce constrain C as given information.

$$C = \frac{1}{N}\sum\frac{|F_{cal}(H) - F_{obs}(H)|^2}{\sigma_H^2} , \tag{3-11}$$

where $F_{obs}(H)$ is the observed crystal structure factor by experiment, N is the number of structure factors, and σ_H is the standard deviation for $F_{obs}(H)$. $F_{cal}(H)$ can be obtained using the following function.

$$F_{cal}(H) = V \int \rho(r)\exp(-2\pi i r \cdot H)dr . \tag{3-12}$$

V is the unit cell volume. C is expected to be 1 from the error theory. Combined with

the equations (3-7) and (3-10), the following entropy $Q(\lambda)$ equation is obtained.

$$Q(\lambda) = -\sum_r \rho'(r) \ln \frac{\rho'(r)}{\rho_0'(r)} - \frac{\lambda}{2}(C-1),$$ (3-13)

where λ is Lagrangian multiplier. Using the approximation $\partial Q(\lambda)/\partial \rho(r) = 0$ which maximizes equation (3-10), finally we have,

$$\rho(r) = \exp\left[\ln \rho_0(r) + \lambda F_0 \sum \frac{1}{\sigma_H^2} \{F_{obs}(H) - F_{cal}(H)\} \exp(-2\pi i r \cdot H) \right]$$ (3-14)

where $F_{cal}(H)$ is approximated as a Fourier transform of $\rho_0(r)$

$$F_{cal}(H) = V \int \rho_0(r) \exp(-2\pi i r \cdot H) dr .$$ (3-15)

The right side of the expression (3-13) is a function that depends only on $\rho_0(r)$.

In an actually calculating process, firstly given a uniform electron charge density distribution to the $\rho_0(r)$, then $\rho(r)$ is obtained. The operation of setup values in $\rho_0(r)$ is repeated until C no larger than one to finally obtain the electron density distribution. The electron charge density distribution $\rho(r)$ obtained by this method does not change with different initial value $\rho_0(r)$. The ultimate goal is to get the accurate $F_{obs}(H)$.

3.3 MEM/Rietveld method

MEM/Rietveld method is a combination of MEM method and Rietveld analysis mentioned above to study the charge density distribution study. The electron charge density distribution can be obtained using the synchrotron-radiation X-ray powder diffraction data combined with MEM/Rietveld analysis. The method can be simply described as the following process.[101]

In the powder diffraction experiment, the Bragg reflections are projected on the 2θ-axis, so the reflections overlap each other. Therefore, in order to obtain the electron charge density distribution from the diffraction pattern, the following processes should be taken.

(1) Separate the multiple overlaps of Bragg reflections and multiple every product of Bragg reflection.

(2) Various corrections are applied to obtain the absolute value of the crystal structure factor based on the obtained integrated intensity.

(3) Assume a crystal structure model and determine the crystal structure factor based on it.

(4) Perform the MEM analysis using the obtained crystal structure factor.

The first three steps are involved in the Rietveld analysis. The profile separation can be obtained using the structural model that best matches the experimental powder diffraction pattern in the Rietveld analysis. Various corrections involved in the crystal structure model are needed to obtain the precise structural factor, such as the lattice parameter, atomic position, thermal vibration, profile and so on. Finally, electron charge density distribution analysis by MEM is carried out based on the crystal structure factor obtained from the modified crystal structure model. One should notice that comparison between the electron charge density distribution and crystal structure is needed. when the obtained electron density distribution shows no agreement with the crystal structure model, the crystal structure model should be modified to match the result of the electron density distribution, and Rietveld analysis should be performed again. Through these several repeating cycles, we can finally obtain the crystal structure model and the corresponding electron density distribution. Figure 3-4 shows a flowchart of the MEM/Rietveld method.[101]
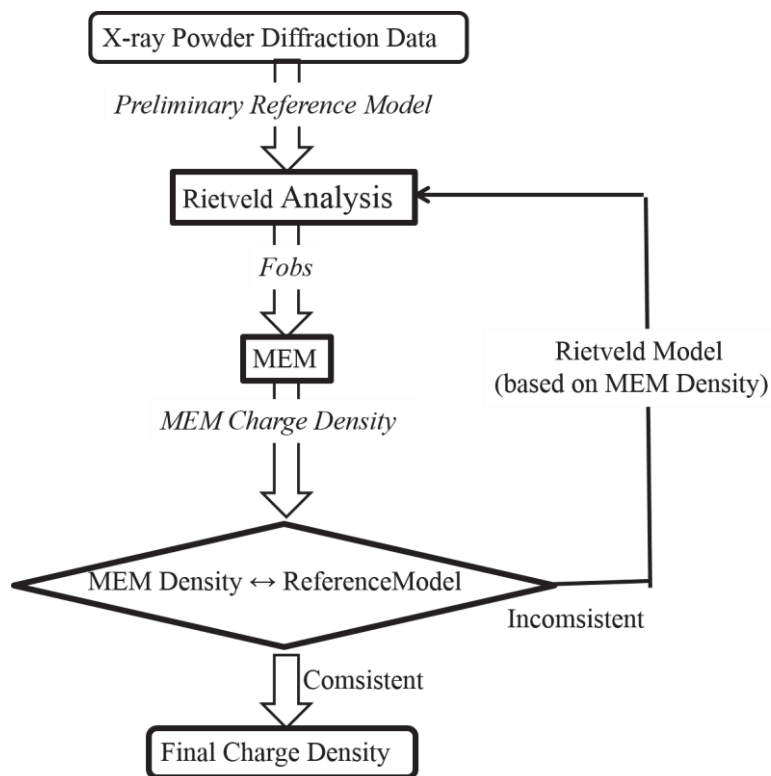
Figure 3-4 Flow chart of the MEM/Rietveld method.

Chapter 4
Electron charge density study of BaBiO₃

Perovskite-type oxide $BaBiO_3$ has been recognized as an important mother compound for superconductors. However, convincing experimental evidence associated with the charge order of Bi ions in $BaBiO_3$ is lacking. Through analyzing synchrotron-radiation X-ray powder diffraction data combined the maximum entropy method/Rietveld method, we present the charge order of Bi^{3+} and Bi^{5+} ions and the nature of chemical bonds in $BaBiO_3$ that are visualized clearly in electron charge density distribution maps. $BaBiO_3$ undergoes successive phase transitions from the

cubic phase with space group $Fm\bar{3}m$ to the rhombohedral $R\bar{3}$, monoclinic $I2/m$, and another monoclinic $P2_1/n$ phases with decreasing temperature. The Bi^{3+}-O bond is considerably more ionic than the Bi^{5+}-O bond in all four phases. $BaBiO_3$ can be regarded as an ionic crystal comprising isolated Ba^{2+} and Bi^{3+} ions as well as $[Bi^{5+}O_6]^{7-}$ octahedra in the $Fm\bar{3}m$ symmetry; a three-dimensional covalent bonding network is formed in the $R\bar{3}$ and $I2/m$ symmetries, and a two-dimensional layered structure comprising $Bi^{3+}O_4$ planar squares and $Bi^{5+}O_6$ octahedra is established in the $P2_1/n$ symmetry at low temperatures. Our study provides a comprehensive understanding of the structural characteristics, electron charge density distribution, and chemical bonds of $BaBiO_3$, which may be useful for developing $BaBiO_3$-derived functional materials such as superconductors.

In this paper, we report the results from high energy synchrotron radiation powder diffraction and charge density study of $BaBiO_3$ to investigate the charge order and phase transition behavior. We demonstrate the crystal structure of $BaBiO_3$ with four phases at temperature in fine steps from 100 to 1100 K. Using synchrotron radiation XRD, we successfully find the direct evidence of charge order in $BaBiO_3$ by detecting the small superlattice reflection peaks. Specially, MEM analysis of SXRD data have proven to be a potential way to determine the electron charge density distribution and corresponding the bonding nature between neighbored atoms, which enables us to directly visualize the electron charge densities around Ba, Bi, and O ions. The difference in chemical bonding on the Bi^{3+}–O and Bi^{5+}–O bonds is clearly visualized. We found that the Bi^{3+}–O bonding shows unusual characteristics with the dependence of temperature, revealing unusual hybridization between O $2p$ and Bi $6s$ or $6p$ orbitals. Our works find the bond lengths are slightly diverse with the dependence of temperature, which is together with the transformation of the bonding nature in charge density level. The phase transition mechanism has been disserted from the charge density viewpoint.

We herein report the results of electron charge density distributions of $BaBiO_3$ through analyzing SXRD data using the MEM/Rietveld method, the charge order of Bi ions and the nature of chemical bonds in the four different phases are successfully demonstrated. Small superlattice reflection peaks originating from the charge order of Bi ions at B-sites with a double-perovskite-type structure are successfully detected in the SXRD pattern. Bi^{3+} and Bi^{5+} ion sites in the structure could be successfully distinguished, and the difference of bonding nature between Bi^{3+}–O and Bi^{5+}–O bonds was clearly visualized in MEM electron charge density distribution maps. The structural characteristics were summarized for the four different phases with the viewpoint of chemical bonding nature. The observed nature of chemical bonds and phase transitions were evaluated by first-principles calculations.

4.1 Phase transition of $BaBiO_3$

In order to confirm the phase transition behavior of $BaBiO_3$, we then performed the temperature-dependent synchrotron-radiation XRD measurements as shown in Fig. 4–1. Through observing the change of peak position and peak splitting, we can defectively determine the possibility of phase transition occurring. The different color shows the intensity of peaks with the lowest blue as background and highest red as peak position. During the measurement, we control the temperature from 100 to 1100 K with a rate of 20 K/min through the flowing N_2 gas. It is apparent that there exist four different phases in $BaBiO_3$ from 100 to 1100 K.
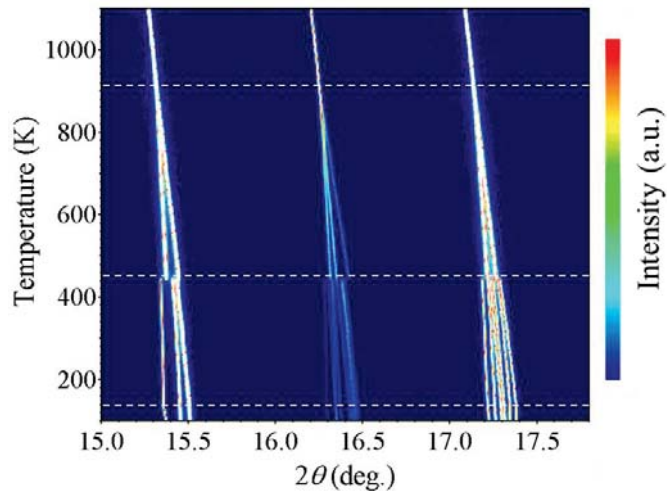
Figure 4–1. Temperature-dependent SXRD patterns of $BaBiO_3$ in the 2θ ranges of 15.0°-17.8° upon heating from 100 to 1100 K with a rate of 20 K/min. The four phases are separated by broken lines at the phase transition temperatures.

Unfortunately, $BaBiO_3$ sample is destroyed by the high temperature around 1100 K owing to the evaporability of bismuth which avoid us to observe the possible evolution of Bi ions ordered state. In the beginning, we assume that the ordered structure will be destroyed at higher temperature than 1100 K, which will show a disordered structure with a average Bi^{4+} valence state. We note the diffraction peaks of $Fm\bar{3}m$ cubic phase at ~15.4° $(440)_c$, 16.3° $(442)_c$ and 17.2°$(620)_c$ split at ~867 K, which can be attributed to the $R\bar{3}$ rhombohedral structure. Further decreasing the temperature at ~443 K will lead to the appearance of more peaks split corresponding to the $I2/m$ monoclinic structure. At lower temperature around 116 K, another monoclinic phase with space group $P2_1/n$ occurs, accompanied with these splitting peaks shrink. All these observations unambiguously confirm three phase transitions occurring over a broad temperature window (100-1100 K) with four different stuctur, which give us a clear crystal structure evolution. Generally, the temperature dependence of the lattice parameter is expected to reveal the appearance of phase transitions. As a consequence, we perform this comparison among these four different crystal structures. Figure 4–2 clearly presents the lattice parameters in all four phases with the dependence of temperature, which is scaled to compare the primitive cubic

parent subcell.
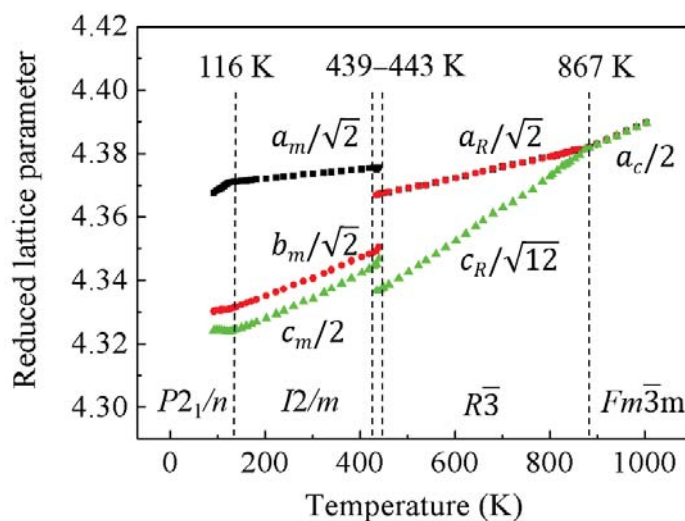
Figure 4–2 The reduced lattice parameter of the primitive cubic subcell in BaBiO$_3$ with the dependence of temperature.

One may notice that the continuous transition from the primitive $P2_1/n$ monoclinic to the second $I2/m$ monoclinic phase has an obvious impact on the tendency of the lattice parameter. In $P2_1/n$ monoclinic phase, the lattice parameter b_m and c_m shorten with increasing temperature, the lattice parameter a_m lengthened at the same time. In contrast, the discontinuous phase transition around 440 K reveal a first-order transition from $I2/m$ monoclinic phase to $R\bar{3}$ rhombohedral phase. With increasing temperature, the two phases get the larger lattice parameter. Besides, there is a two-phase coexistence temperature region from 439–443 K, which is able to obtain lattice parameter in the monoclinic and rhombohedral phase at the same time. Above 867 K, another continuous phase transition to cubic $Fm\bar{3}m$ occurs.

4.2 Crystal structure and charge density at 900 K

To gain a deep insight into the crystal structure of every phase, we hence took high-resolution synchrotron-radiation XRD experiments of BaBiO$_3$ at different temperatures, which have been used in Rietveld analysis and MEM analysis. Figure

4–3 shows the SXRD pattern of $BaBiO_3$ measured at 900 K and the related structure from the Rietveld refinement results. The inset shows the superlatice peaks, which reveals the B-site charge order structure.
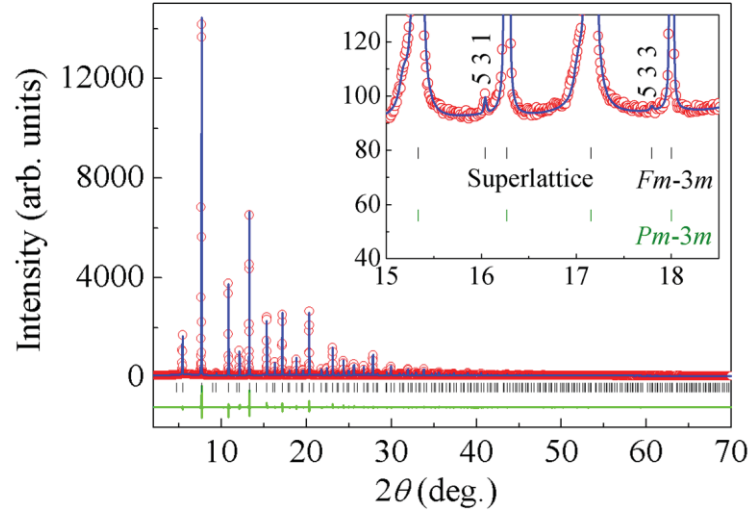
Figure. 4–3 SXRD pattern and structure refinement results of $BaBiO_3$ at 900 K ($2\theta <$ 70°, $d > 0.22$ Å). The observed (circles), calculated (line), and difference (bottom line) are shown. The ticks indicate the Bragg reflections allowed with space group Fm-$3m$. $R_{wp} = 4.78\%$, $R_i = 2.85\%$, $R_f = 2.38\%$. The inset shows the supperlattice peaks.

The refined crystal-structure parameters using the Rietveld refinement are listed in Table 4-1. The diffraction peaks can be assigned on a cubic $Fm\bar{3}m$ ordered double perovskite with lattice parameter double times of the lattice constant of simple disordered perovskite.

Table 4–1 Refined Structural Parameters of BaBiO$_3$ at 900 K in cubic phase.[a]

Atom	Site	x	y	z	U_{11}	U_{22}	U_{33}
Ba	8c	0.25	0.25	0.25	3.18(1)	$=U_{11}$	$=U_{11}$
Bi^{3+}	4a	0	0	0	1.21(2)	$=U_{11}$	$=U_{11}$
Bi^{5+}	4b	0.5	0.5	0.5	1.67(2)	$=U_{11}$	$=U_{11}$
O	24e	0.2619(32)	0	0	3.37(63)	9.67(47)	$=U_{22}$

[a] The space group is $Fm\overline{3}m$ (No. 225). The lattice parameter is a = 8.7721(2) Å. The isotropic thermal parameter $U_{11} = U_{22} = U_{33}$ is refined for Ba, Bi^{3+} and Bi^{5+}. The anisotropic thermal parameters U_{11} and $U_{22} = U_{33}$ are determined for O. Off diagonal elements, $U_{12} = U_{13} = U_{23} = 0$. U_{ij} are given in units of 10^{-2} Å^2.

The absence of some diffraction peak suggests the face-centering of the ordered unit cell, whose index shows the $h + k$, $k + l$, and $h + l$ = odd [102] The appearance of diffraction peaks of (531) and (533) peaks shown in Fig. 4-3 indicates the charge ordering of Bi^{3+} and Bi^{5+} ions. The Rietveld refinement results clearly prove that BaBiO$_3$ forms a B-site ordered double perovskite structure. In this cubic space group, Ba ions are located at 8c (0.25, 0.25, 0.25) position, Bi^{3+} ions at 4a (0, 0, 0) position, Bi^{5+} ions at 4b (0.5, 0.5, 0.5) position, and the O ions at a special site 24e (x, 0, 0), respectively.[103] The only changeable position parameter is the O$_x$, which attributes the Bi^{3+}–O and Bi^{5+}–O bond length. The Bi–O bond lengths were found to be Bi^{3+} 2.298 Å and Bi^{5+} 2.088 Å. Based on the refined bond length, bond valence sum (BVS) calculations give a valence state to be 3.46 for Bi^{3+} site and 5.56 for Bi^{5+} site,[104] suggesting a charge order of Bi^{3+} and Bi^{5+} ions. One may notice the thermal vibration factor of the oxygen ions along the direction perpendicular to the Bi-O bonds, $U_{O22}(=U_{O33})$, is larger than U_{O11} along the direction parallel to the Bi-O bonds, which is owing to the existence of covalent bonding between Bi^{5+} and O shown in Fig. 4–4. The reliable factor of structure factors R_F determined from Rietveld analysis was 2.38%

used in the final MEM charge density analysis. There are 436 observed structure factors from the Rietveld analyses for 900 K data that were used in the MEM analyses. The MEM analyses were performed in an unit cell divided into $176 \times 176 \times 176$ pixels. The volume of one pixel is equal to about $0.05 \times 0.05 \times 0.05$ Å^3.

The charge-density distributions of Three–dimension (3D) and Two–dimension (2D) on (100) plane at 900 K are shown in Fig. 4–4(a) and 4–5(a), respectively. Here the isosurface represents the average distribution of electron clouds. Compared with the core electron density size of Bi ions, Bi^{5+} ions are more localized than Bi^{3+} shown in Fig. 4–4 (b) and (c), which is consistent with the fact that the radii of Bi^{5+} ions (0.76 Å) are smaller than Bi^{3+} ions (1.03 Å). From this point, we can easily distinguish the Bi ions with different valence state at different site.
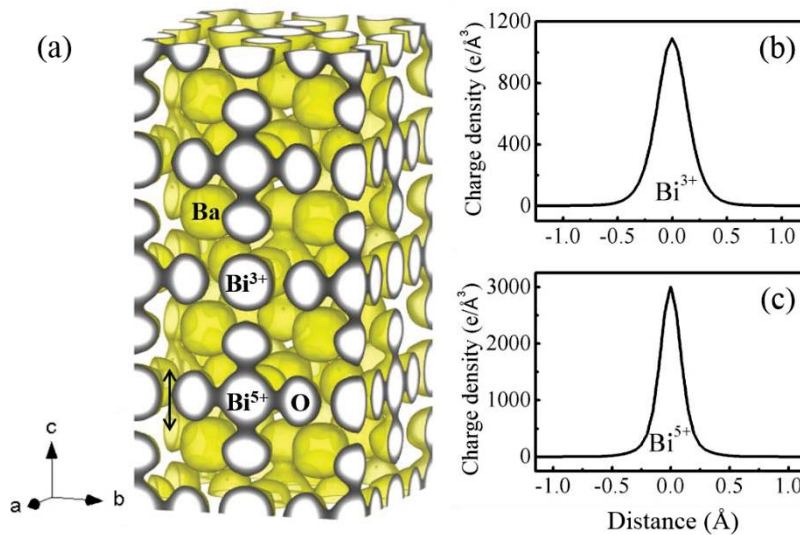
Figure 4–4 (a) 3D MEM electron density distribution at 900 K with space group *Fm*-3*m*. The isosurface is 0.5 e Å^{-3}. 1D charge density around (b) Bi^{5+}, and Bi^{3+} (c) cut at the minimum charge density point in O-Bi^{3+}/Bi^{5+}-O bond along [010] direction.

The electron charge density distributions around O in cubic BaBiO$_3$ are quite anisotropic as shown in Fig. 4–4(a), extending along the direction perpendicular to the Bi^{5+}–O bond direction, which is in good agreement with the larger $U_{O22}(=U_{O33})$ thermal parameters in the Rietveld analysis results. The electron charge density

distributions around Ba^{2+} in cubic $BaBiO_3$ are essentially ionic, there is no electron density overlap observed between Ba^{2+} and O^{2-}. The minimum charge density on the longer Bi^{3+}–O bonding is 0.40 e $Å^{-3}$. This is the same value as the background (~0.36 e $Å^{-3}$) level, which is owing to the strong thermal vibration at 900 K. On the other hand, the electron charge densities of Bi^{5+} and O are found to be highly overlapped. The minimum charge density on the shorter Bi^{5+}–O bonding in Fig. 4–5(a) is charged up to 0.62 e $Å^{-3}$, which is much larger than the Bi^{3+}-O bond. This demonstrates that the Bi^{3+}-O bonding nature of the cubic phase should be ionic, however, that of Bi^{5+}–O is found to be strong covalent, which forms an special ionic crystal consisting of two Ba^{2+} and a Bi^{3+} ions, and an isolated $(Bi^{5+}O_6)^{7-}$ octahedron. In order to confirm the rationality of the experiment results, Figure 4–5(b) shows the electron charge density distribution on the (100) plane determined by the first principles calculation.
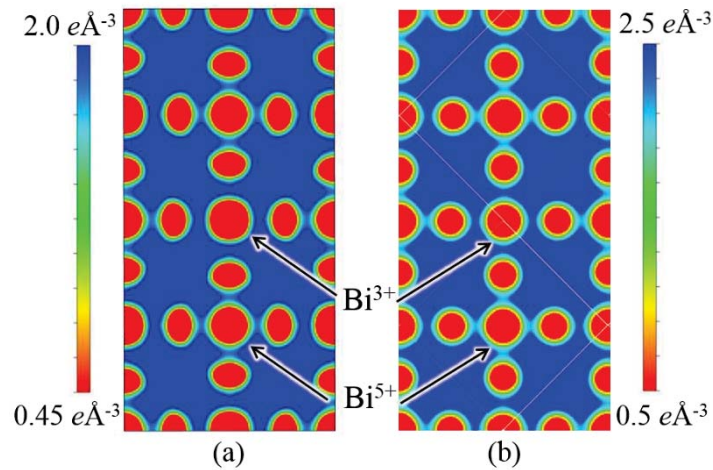
Figure 4–5 (a) 2D MEM electron density distribution of $BaBiO_3$ on the (100) plane at 900 K in cubic phase, contour lines are drawn from 0.0 to 4.0 e $Å^{-3}$ at intervals of 0.5 e$Å^{-3}$,and (b) electron density distribution determined by the first–principles calculation based on the atomic coordinates.

In the First-principle calculations, the actual cubic lattice parameters (see Table 1) at 900 K obtained from Rietveld analysis were used. The First-principle calculation results quantitatively reproduces MEM charge density compared with the experimental results. As for the minimum charge density between Bi^{3+}/Bi^{5+} and O,

there is not much difference between the experimentally obtained value and the theoretically calculated value using First-principle calculation shown in Fig. 4–5(b). One may notice that the electron charge density distributions around oxygen are quite isotropic without considering the thermal vibration in the calculations. The minimum electron density is 0.48 e $Å^{-3}$ and 0.36 e $Å^{-3}$ in the Bi^{5+}–O and Bi^{3+}–O bonds, respectively. No overlap of the charge densities is observed between Bi^{3+} and O. Meanwhile, covalent bond nature of Bi^{5+}–O bonding is found, showing good agreement with the experiment results. The ionic crystal structure with two Ba^{2+} and a Bi^{3+} ions, and an isolated $(Bi^{5+}O_6)^{7-}$ octahedron is clearly determined.

4.3 Crystal structure and charge density at 600 K

With decreasing the temperature, first phase transition occurs from cubic to rhombohedral structure with $R\overline{3}$ space group through the $a^-a^-a^-$ Glazer tilting. Figure 4–6 and Table 4–2 shows the Rietveld refinement fitting results and refined structural parameter at 600 K, respectively. The inset shows the high angle fitting results.
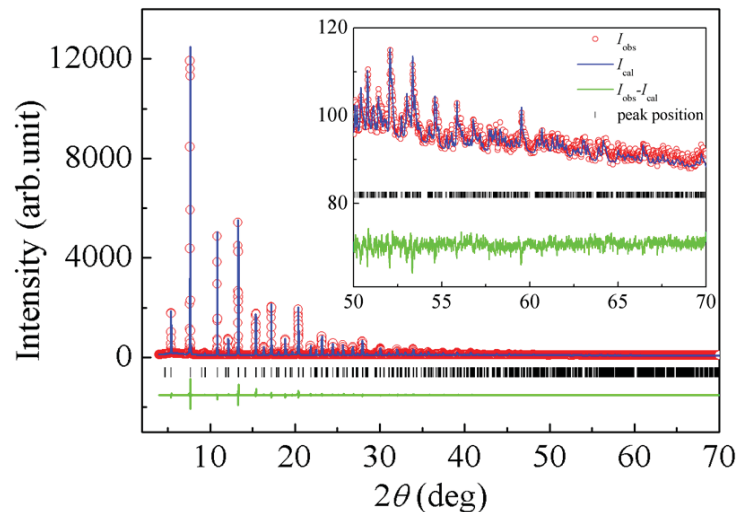
Figure 4–6 XRD pattern and structure refinement results of $BaBiO_3$ at 600 K ($2\theta <$ 70°, $d > 0.22$ Å). The observed (circles), calculated (line), and difference (bottom line)

are shown. The ticks indicate the Bragg reflections allowed with space group $R\bar{3}$. R_{wp} = 3.77%, R_I = 3.65%, R_f= 6.35%. The inset shows the high angle fitting result.

Table 4–2 Structure parameters of $BaBiO_3$ at 600 K in rhombohedral phase.[a]

Atom	Site	x	y	z	B
Ba	6c	0	0	0.2494(2)	1.57(1)
Bi^{3+}	3a	0	0	0	0.92(1)
Bi^{5+}	3b	0	0	0.5	0.44(1)
O	12f	0.5172(19)	-0.0340(20)	0.2580(7)	2.75(17)

[a] The space group is $R\bar{3}$ (No. 148). The lattice parameter is a = 6.1850(1)Å, and c=15.0858(2)Å.

Based on the coordinates, the Bi–O bond lengths in two octahedrons are 2.282 Å and 2.125 Å for Bi^{3+} and Bi^{5+} sites, respectively, which is slightly different from two octahedrons obtained at 900 K cubic phase, giving the BVS valence state to be 3.61 for Bi^{3+} and 5.03 for Bi^{5+}, respectively. There were 2484 structure factors that were used in the MEM analysis, which were determined from the Rietveld refinement in a d-space range larger than 0.36 Å. The MEM analysis was carried out with the unit cell divided into $126 \times 126 \times 300$ voxels.

Figure 4–7 shows the 2D MEM electron density distribution on the $(1\bar{1}2)$ plane at 600 K. The electron densities are both isotropic and highly overlapped in the Bi^{3+}/Bi^{5+}–O bonds. The minimum of the charge densities is charged up to 0.78 e Å^{-3} and 0.86 e Å^{-3} in the Bi^{3+}–O and Bi^{5+}–O bonding, respectively, which confirm the formation of covalent bonds. The minimum charge density is much larger than the value of the background level. In contrast, Ba^{2+} ions are highly ionic without any charge density overlap with the coordinated O ions. All of this information suggests

that BaBiO$_3$ forms a normal 3D covalent network through the connection of Bi^{3+}–O-Bi^{5+} bonds at 600 K. The special ionic state of Bi^{3+} ions at 900 K is broken instead with a covalent state at 600 K, owing to the rotation of the oxygen octahedron. Meanwhile, Bi^{5+} ions still hold stronger covalent bonds with the coordinated O atoms than the Bi^{5+}–O bonds in cubic phase.
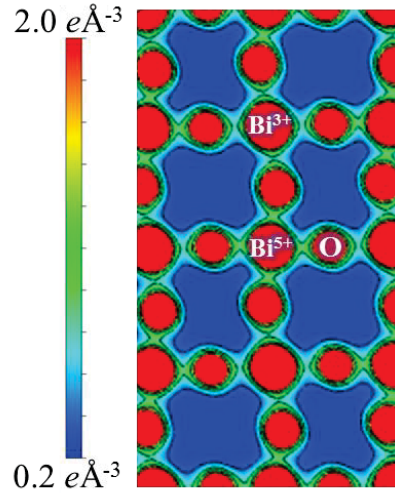
Figure 4–7 2D MEM electron density distribution of BaBiO$_3$ on the (1$\bar{1}$2) plane at 600 K in rhombohedral phase. Contour lines are drawn from 0.0 to 4.0 e Å^{-3} at intervals of 0.2 e Å^{-3}.

4.4 Crystal structure and charge density at 300 K

At 300 K, BaBiO$_3$ shows a monoclinic structure with the space group of *I2/m*, and the fitting result of the Rietveld analysis are shown in Fig. 4-8 and summarized in Table 4–3. Through the $a^0b^-b^-$ tilt system, the oxygen positions are modified into two different sites. As a consequence, the octahedrons around the Bi ions include two different sets of Bi-O bonds, that is, Bi-O1 (Bi^{3+}-O1 2.276 Å and Bi^{5+}–O1 2.135 Å) and Bi–O2 (Bi^{3+}–O2 2.262 Å and Bi^{5+}–O2 2.149 Å) bonds.
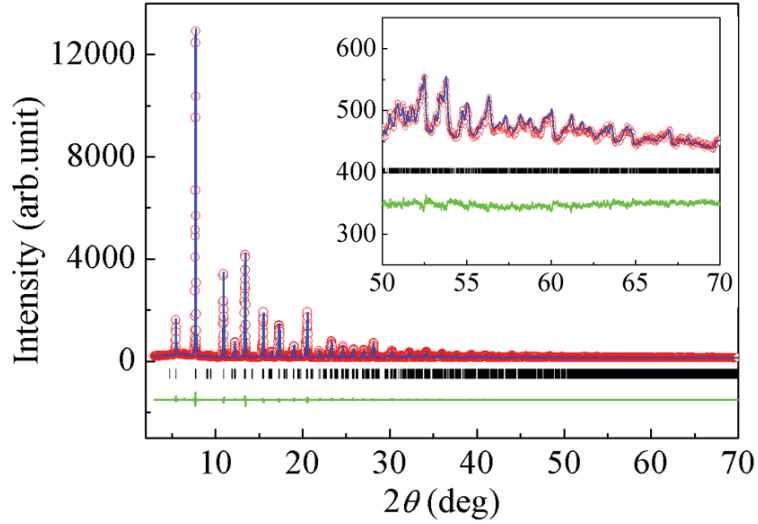
Figure 4–8 XRD pattern and structure refinement results of BaBiO$_3$ at 300 K ($2\theta <$ 70°, $d > 0.22$ Å). The observed (circles), calculated (line), and difference (bottom line) are shown. The ticks indicate the Bragg reflections allowed with space group $I2/m$. $R_{wp} = 1.90\%$, $R_i = 3.21\%$, $R_f = 3.62\%$. The inset shows the high angle fitting result.

Table 4–3 Structure parameters of BaBiO$_3$ at 300 K in monoclinic phase.[a]

Atom	Site	x	y	z	B
Ba	$4i$	0.5013(3)	0	0.2465(1)	0.72(0)
Bi^{3+}	$2a$	0	0	0	0.30(2)
Bi^{5+}	$2d$	0	0	0.5	0.23(1)
O1	$4i$	0.0657(10)	0	0.2584(12)	1.33(14)
O2	$4j$	0.2673(10)	0.2453(16)	-0.0376(4)	1.25(9)

[a] The space group is $I2/m$ (No. 12). The lattice parameter is $a = 6.1871(1)$Å, $b = 6.1399(1)$Å, $c=8.6710(1)$Å, and $\beta=90.179(1)$°.

The number of structure factors determined from the Rietveld refinement was

5353 structure factors, which were transformed in the MEM analysis. The MEM analysis was performed in a unit cell divided into $124 \times 120 \times 176$ voxels. In Fig. 4–9, the MEM charge density at 300 K on the (020) plane and between Bi^{3+}/Bi^{5+} and O2 is visualized. The MEM electron charge density clearly exhibits the Bi^{3+}–O and the Bi^{5+}–O bonding features along any directions in the octahedrons. Similar to the MEM result of rhombohedral structure, the monoclinic phase at 300 K also forms a normal 3D covalent network structure at the charge density level. The minimum charge density of Bi^{5+}–O1 (=1.04 e $Å^{-3}$) and Bi^{5+}–O2 (=0.96 e $Å^{-3}$) bonds is larger than the Bi^{3+}–O1 (=0.93 e $Å^{-3}$) and Bi^{3+}–O2 (=0.86 e $Å^{-3}$) bonds, respectively. This bonding electron distribution is consistent with the MEM result of rhombohedral structure.
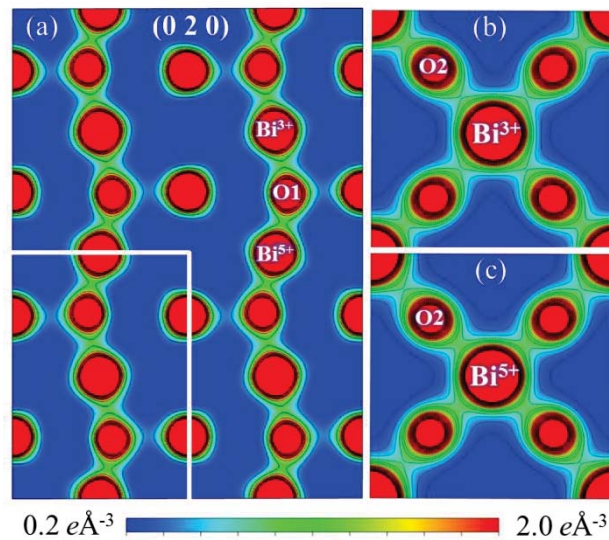
**Fig. 4–9** 2D MEM electron density distribution of $BaBiO_3$ (a) on the (020) plane between Bi^{3+}/Bi^{5+} and O1, (b) between Bi^{3+} and O2, and (c) between Bi^{5+} and O2 at 300 K in monoclinic phase, contour lines are drawn from 0.0 to 4.0 e $Å^{-3}$ at intervals of 0.2 e$Å^{-3}$.

4.5 Crystal structure and charge density at 100 K

In the second monoclinic phase at 100 K, the space group of double perovskite is $P2_1/n$ and the tilt system is $a^+b^-b^-$. The refinement results and structure parameters are shown in Fig. 4–10 and Table 4-4. One may notice that oxygen positions are modified into three different sites. Hence, the Bi-O1/O2/O3 bond lengths in the larger $Bi^{3+}O6$ octahedron are 2×2.450, 2×2.256, 2×2.211 Å, while bond lengths in the smaller $Bi^{5+}O_6$ octahedron are 2×1.989, 2×2.127, 2×2.188 Å. The Bi^{3+}–O1 bond is much longer than Bi^{5+}–O1 bond, which therefore shows a very different bond nature. Based on the bond length BVS calculation, the valence state of the Bi ions are 3.5 and 5.5 for Bi^{3+} and Bi^{5+}, respectively.
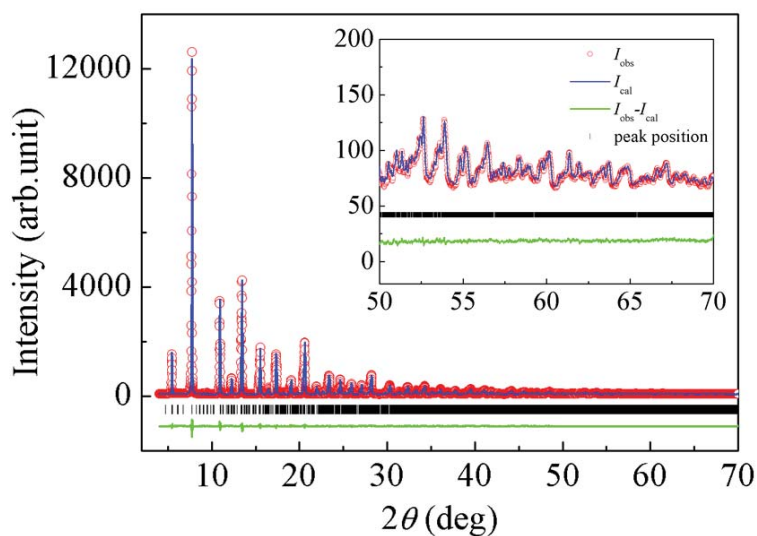
Figure 4–10 XRD pattern and structure refinement results of $BaBiO_3$ at 100 K ($2\theta <$ 70°, $d > 0.22$ Å). The observed (circles), calculated (line), and difference (bottom line) are shown. The ticks indicate the Bragg reflections allowed with space group $P2_1/n$. $R_{wp} = 3.28\%$, $R_i = 2.36\%$, $R_f = 3.02\%$. The inset shows the high angle fitting result.

Table 4–4 Structure parameters of $BaBiO_3$ at 100 K in monoclinic phase.[a]

Atom	Site	x	y	z	B
Ba	4e	0.5037(2)	-0.0099(1)	0.2473(2)	0.24(0)
Bi^{3+}	2a	0	0	0	0.13(3)
Bi^{5+}	2b	0	0	0.5	0.13(3)
O1	4e	0.0796(12)	0.0047(24)	0.2777(10)	1.23(19)
O2	4e	0.2632(51)	0.2513(43)	-0.0296(46)	1.20(19)
O3	4e	0.2681(48)	0.7660(39)	-0.0326(47)	1.20(19)

[a] The space group is $P2_1/n$ (No. 14). The lattice parameter is $a = 6.1811(1)$Å, $b = 6.1279(1)$Å, and $c=8.6544(1)$ Å.

The number of structure factors determined from the Rietveld refinement were 7272. The MEM analysis was then performed in an unit cell divided into $124 \times 124 \times 172$ voxels. Figure 4–11 shows the 2D MEM electron charge density distribution on the (020) plane at 100 K.
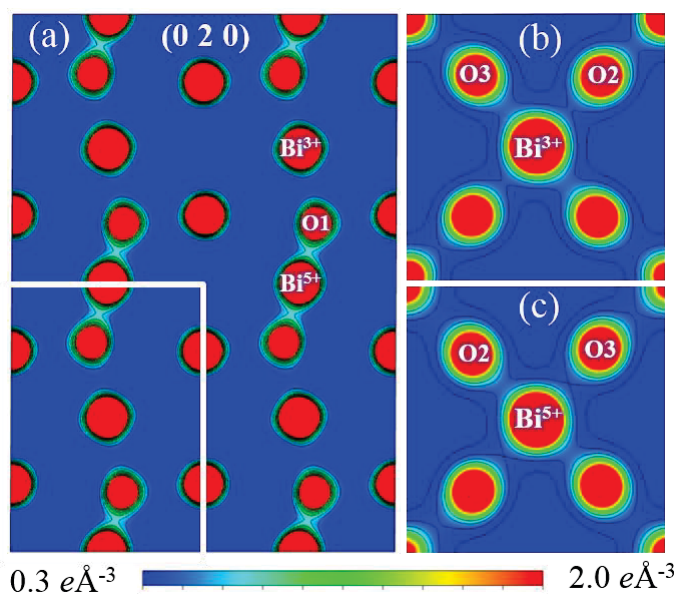
Figure 4–11 2D MEM electron density distribution of $BaBiO_3$ (a) on the (020) plane between Bi^{3+}/Bi^{5+} and O1, (b) between Bi^{3+} and O2/O3, and (c) between Bi^{5+} and O2/O3 at 100 K in monoclinic phase, contour lines are drawn from 0.0 to 4.0 eÅ^{-3} at intervals of 0.2 e Å^{-3}.

Obviously, the electron charge densities around Bi^{3+} and O are quite anisotropic. The electron densities are overlapped along the directions of Bi^{3+}–O2 and Bi^{3+}–O3 with short bonds as shown in Fig. 4–11(b). In a contrast, Figure 4–11(a) shows that Bi^{3+} atom is isolated with the coordinated O1 atom without any charge density overlap. The minimum of the electron densities in the short Bi^{3+}–O2 and Bi^{3+}–O3 bonds are charged up to about 0.41 and 0.47 e Å^{-3}, respectively, revealing the appearance of covalent bonds. One may notice the minimum charge density along the longer Bi^{3+}–O1 bond is about 0.30 e Å^{-3}, that is the same value as the charge density of background level, revealing the ionic bonding nature. As a consequence, Bi^{3+} ions form a special planar square structure. In contrast, Bi^{5+} ions show a normal 3D covalent octahedron. We can observe the electron charge density overlap along the Bi^{5+}–O2 and Bi^{5+}–O3 bonds in Fig. 4–11(c), where the minimum charge density is charged up to 0.47 and 0.40 e Å^{-3}, respectively. Besides, the shortest Bi^{5+}–O1 bond shows the stronger covalent bonds than the other two longer Bi^{5+}–O bonds with a larger minimum charge density of 0.73 e Å^{-3}. All of this information suggests that

BaBiO$_3$ forms an intriguing 2D low dimensional covalent layer through the connection of Bi^{3+}O$_4$ planer square and Bi^{5+}O$_6$ octahedron at 100 K.


4.6 Phase transition mechanism

To gain a deep investigation of the phase transition mechanism of BaBiO$_3$, we next try to reveal the phase transition mechanism at the charge density level as shown in Fig. 4–12. The evolution of electron charge density and correspond crystal structure of BaBiO$_3$ at different temperature are clearly observed, which is that expected for the evolution of the Bi–O bonds and its minimum charge density.
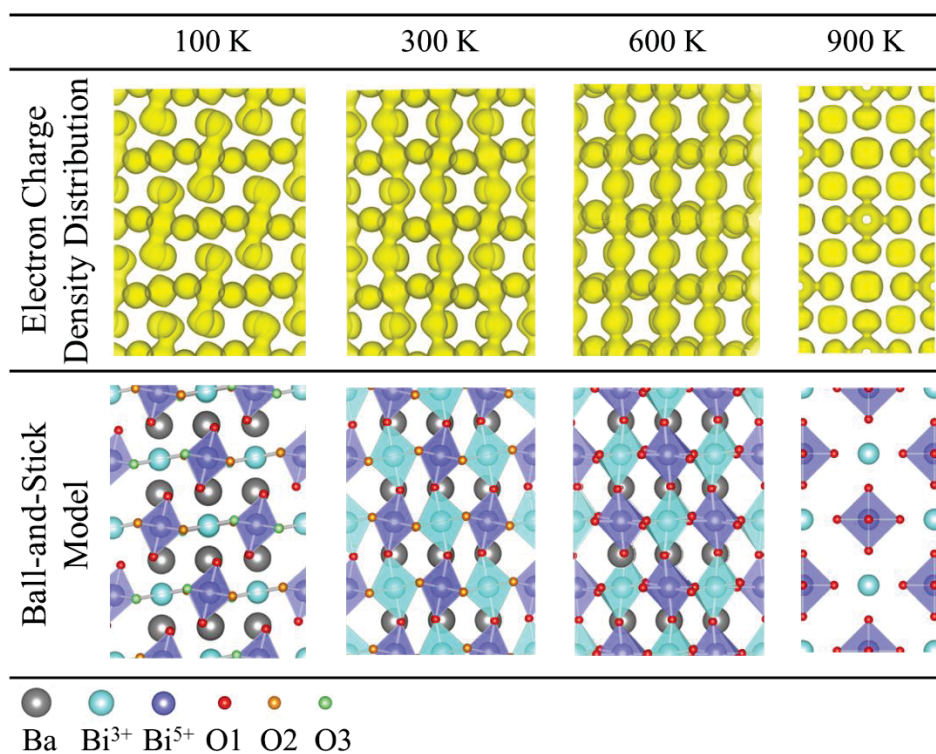
Figure 4–12 The evolution of electron charge density and correspond crystal structure of BaBiO$_3$ with the dependence of temperature.

We found the Bi–O bond length to be distinctly different in two octahedral sites as shown in Fig. 4–13. The average Bi^{3+}–O bonds slightly increase upon heating

process, whereas, the average Bi^{5+}–O bonds decrease. The Bi^{3+}–O bonds persist larger than the Bi^{5+}–O bonds in the whole temperature range.
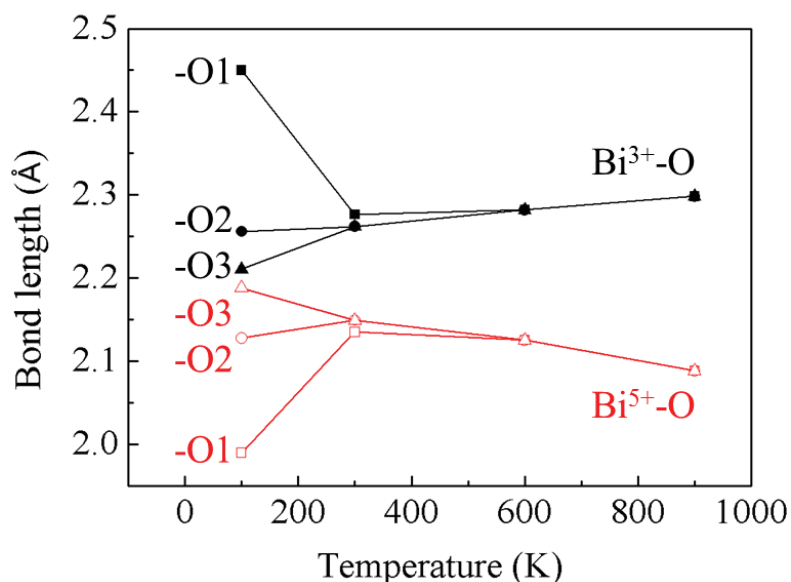
Figure 4–13 The bond length of Bi–O with the dependence of temperature.

In other word, the Bi^{5+}–O bonds show stronger covalency, which are not easily affected by the temperature. We can always observe the charge density overlap of Bi^{5+} and O in all four phases of $BaBiO_3$ in Fig. 4–12. However, the bond nature of Bi^{3+}–O bonds shows intriguing evolution with the dependence of temperature. At 100 K monoclinic phase, Bi^{3+} ions hold a special square planner charge density configuration with four covalent bonds and two ionic bonds. Differently, Bi^{3+} ions show a normal octahedral structure with six covalent bonds at 300 K monoclinic and 600 K rhombohedral phases. The covalent nature of the Bi^{3+}–O bonds is destroyed in cubic phase at 900 K, instead with an ionic structure isolated with the coordinated oxygen atoms. All these facts suggest that the phase transition accompanied with the deformation of the charge density around the Bi^{3+} ions. We show the correspond structure at the charge density level using the ball–and–stick model in Fig. 4–12, here the sticks reveal the covalent nature of the bonds. Accordingly, upon heating, the $BaBiO_3$ structure represent a novel evolution from a 2D covalent-bonding network

consisting of the $Bi^{3+}O_4$ planner square and $Bi^{5+}O_6$ octahedron, to a normal 3D covalent bonding network consisting of two BiO_6 octahedrons, and to an ionic structure consisting of the isolated $[Bi^{5+}O_6]^{7-}$ octahedron and Bi^{3+} ions.

It becomes important to see whether the change in symmetry from monoclinic to rhombohedral, and to cubic is possible or not. For this, the energy hierarchy of $BaBiO_3$ using the first–principle method is shown in Fig. 4–14. The calculated energy difference between different symmetry is obvious. From cubic to monoclinic symmetry, the energy is monotonously decreasing, which reveals the more stable structure. The ground state is found to be monoclinic phase with $P2_1/n$ symmetry.
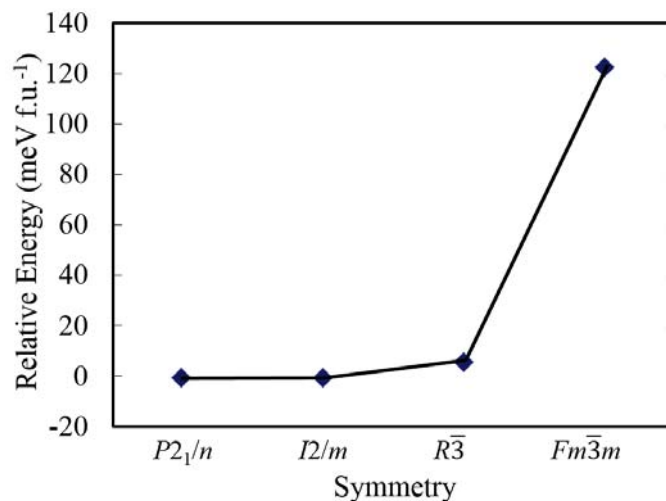
Figure 4-14 Energy hierarchy of $BaBiO_3$ using First-principle calculation method.

4.7 Conclusion

The crystal structure and phase transitions of $BaBiO_3$ have been studied by high resolution synchrotron-radiation X-ray powder diffraction. The charge order and the chemical bonding nature are investigated based of the electron charge density study by MEM/Rietveld method. We find that $BaBiO_3$ undergoes phase transitions from monoclinic, to rhombohedral, and to cubic symmetry upon heating progress. Importantly, we clearly reveal the charge order of Bi^{3+} and Bi^{5+} ions located at different octahedron in the charge density distribution map. The phase transitions are

accompanied with the variation of the bonding nature in Bi^{3+}–O bond. We find the deformation of charge density distribution around Bi^{3+} ions, which leads to the variation of correspond structure from two-dimensional covalent layer, to three-dimensional covalent network, and to a mutually isolated structure with Bi^{3+} ions and $[Bi^{5+}O_6]^{7-}$ octahedra. We highlight that charge density study using MEM/Rietveld method provide a pathway to investigate the charge order and phase transition mechanism.

Chapter 5
Electron charge density study of $BaBiO_{2.5}$

Engineering environments of cations in oxides surrounded by oxygen coordination has received much intense interest owing to many intriguing discoveries of novel oxides with unexpected physical properties. In this work, we successful synthezed the layered $BaBiO_{2.5}$, which is acheived by a phase transformation from the parent perovskite $BaBiO_3$. Through analysing the synchrotron-radiation X-ray diffraction data combined with the MEM/Rietveld method, we investigated the unusual chemical bondings nature of Bi-O bonds consisting of Bi ions and four oxygen coordinations,   where an inhomogenous coordination geometry was found. As a consequence, this special asymmetry structure results in the near-infrared luminescence, which is different from the other ordinary Bi-containing systems. The mechnism of excitonic nature in luminescence were proposed based on the experimental and theoretical results. This work opens a pathway to the discover new materials systems with intriguing functionalities in these compounds with uncommon Bi-O bonding and Bi coordination environments. This work could inspire intense interest to explore functional materials with unusual properties containing heavier elements.

5.1 Crystal structure of BaBiO$_{2.5}$

Layered BaBiO$_{2.5}$ sample was prepared by using heat treatment of parent BaBiO$_3$ sample at 800 ℃ temperature in a reductive N$_2$ (O$_2$<10^{-6}) atmosphere, based on an oxygen reduction transformation process. The polycrystalline BaBiO$_3$ sample was prepared using the solid-state reaction method with stoichiometric amounts of Ba(NO$_3$)$_2$ powder (Aladdin., 99.99%) and Bi$_2$O$_3$ powder (Aladdin., 99.99%). Initial compounds were thoroughly ground for the next heating treatment. The ground powder was heated at 600 °C for 24 hours. After cooling to room temperature, the powder was ground and heated again at 800 °C for 8 hours in air.

During the collection of XRD diffraction pattern process, the succeeded samples were tightly sealed sandwiched with two pieces of tapes to prevent the polluion of water and oxygen, and the XRD pattern of the tape was also shown in the XRD pattern. Obviously, heating treatment of BaBiO$_3$ at 600 ℃ fails to transform the perovskite-type structure of BaBiO$_3$. The structure of BaBiO$_{2.5}$ phase did not occur, which signifies the failure of the bond dissociation divided from the oxygen octahedron coordination. Heating treatment at 700 and 800 ℃ can both results in the occurrence of BaBiO$_{2.5}$ structure phase. Here the BaBiO$_{2.5}$ phase obtained from 800 ℃ heating treatment shows much higher quality in the crystallinities. Increasing the treatment temperature to 900 ℃, an unknown structure phase will occur. Besides, the other Note that the reductive atmosphere is necessary to obtain the BaBiO$_{2.5}$ from BaBiO$_3$ phase. The attempt of heating treatment at air atmosphere failed to obtain the BaBiO$_{2.5}$ structure phase. The synthesis condition plays a critical important role in the formation of BaBiO$_{2.5}$ structure phase.
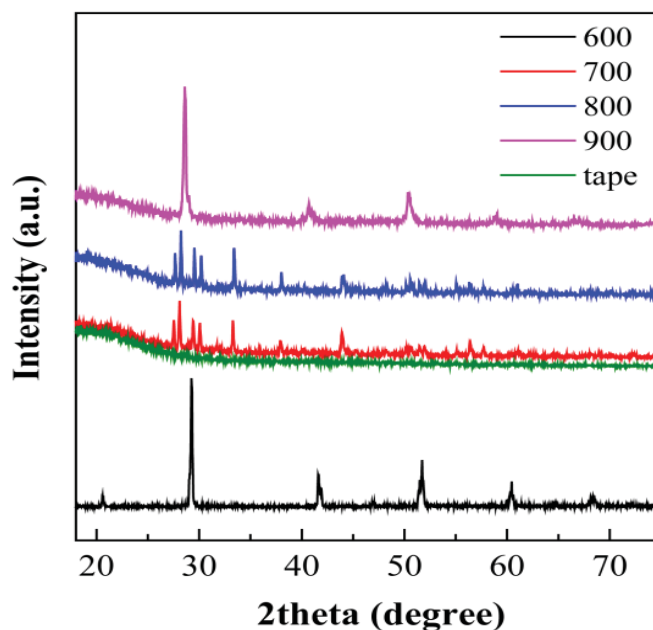
Figure 5-1 XRD patterns of the yielded products by thermal treatment of $BaBiO_3$ at different temperatures (600, 700, 800, and 900 ºC) in flowing reductive high-purity N_2 gas including the XRD of the tapes.

The resulting product we obtained is dark green powder. The process of synthesis of $BaBiO_{2.5}$ is recoverable reverted back to $BaBiO_3$ phase. The result of treatment in an oxygen atmosphere are shown in Fig. 5-2. The oxidation process occurs from $BaBiO_{2.5}$ to $BaBiO_3$ phase. The oxygen vacancy concentration of $BaBiO_{2.5}$ was determined using thermogravimetric data taken in flowing oxygen as shown in Fig. 5-3. Based on the weight difference between obtained $BaBiO_{2.5}$ and $BaBiO_3$, the oxygen vacancy concentration of $BaBiO_{2.5}$ was found to be exact 2.5. The synthesis of $BaBiO_{2.5}$ has been performed using other methods in some papers, however, some impurity phases or oxygen-deviated phases are usually found. We successfully synthesized the stoichiometric $BaBiO_{2.5}$ owing to the controlling of annealing temperature and the used atmosphere.
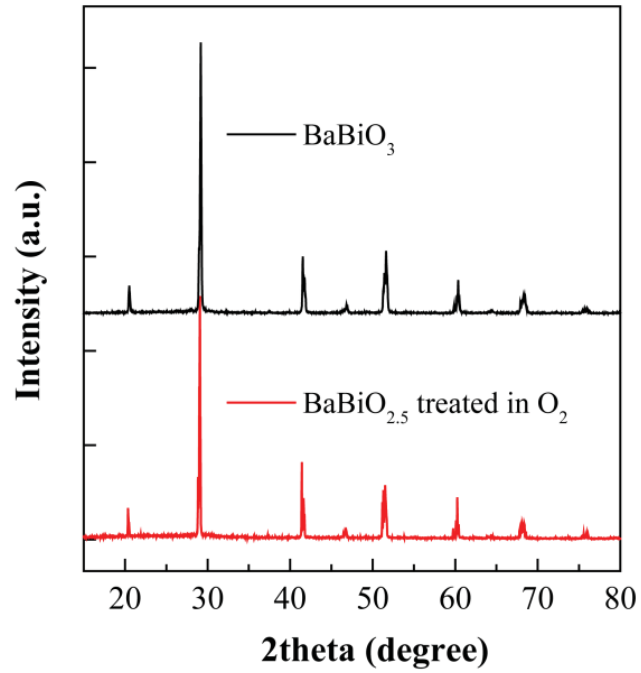
Figure 5-2 XRD patterns of synthesized $BaBiO_3$ perovskites (black) and compounds obtained from the $BaBiO_{2.5}$ treated in flowing O_2 atmosphere(red).
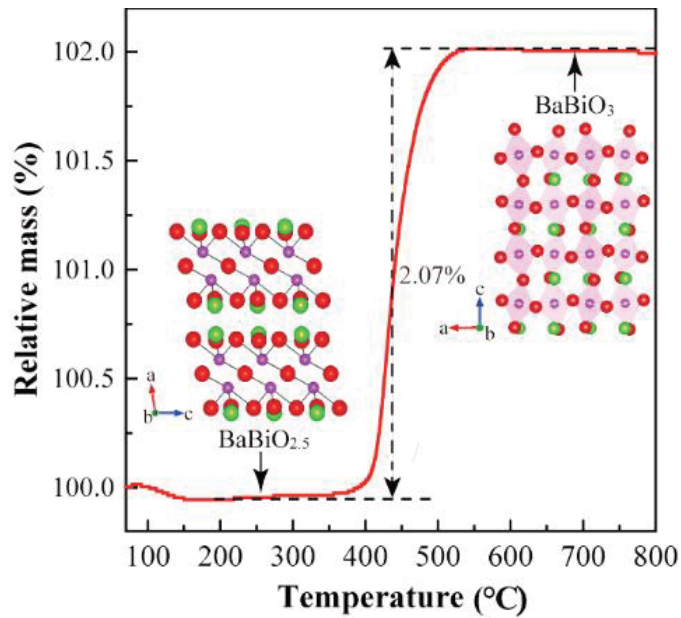

Figure 5-3 Thermogravimetric data collected during the transformation of $BaBiO_{2.5}$ to $BaBiO_3$ in oxygen atmosphere. Insets show the structures of $BaBiO_{2.5}$ (left) and $BaBiO_3$ (right). The red, purple and green balls represent O, Bi, and Ba atoms,

respectively.
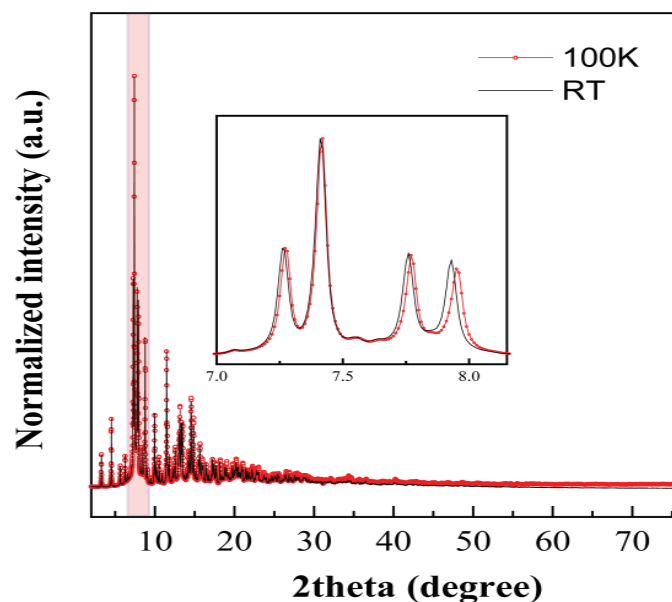
Figure 5-4 Synchrotron XRD patterns of $BaBiO_{2.5}$ at room temperature (RT) and 100 K. No phase transition occurs when cooling $BaBiO_{2.5}$ down to 100 K. Inset shows the enlarged XRD patterns.

In order to confirm the possible phase transition behavior of $BaBiO_{2.5}$, we then collected the SXRD pattern at room temperature and 100 K as shown in Fig. 5-4. Through the comparison between XRD pattern of $BaBiO_{2.5}$, no peak splitting or extra peaks are observed, revealing no phase transition occurring in the temperature range from room temperature to 100 K. The data taken at 100 K showed a better signal-to-noise ratio, we then used it in the following charge density study of MEM/Rietveld analysis. $BaBiO_{2.5}$ shows a monoclinic structure with a $P2_1/c$ space group, and the fitting results of the Rietveld analysis are shown in Fig.5-5 and summarized in Table 5-1. The reliability factors of the intensities R_I and the average weighted profile R_{wp} are about 3.73% and 3.69%, respectively.
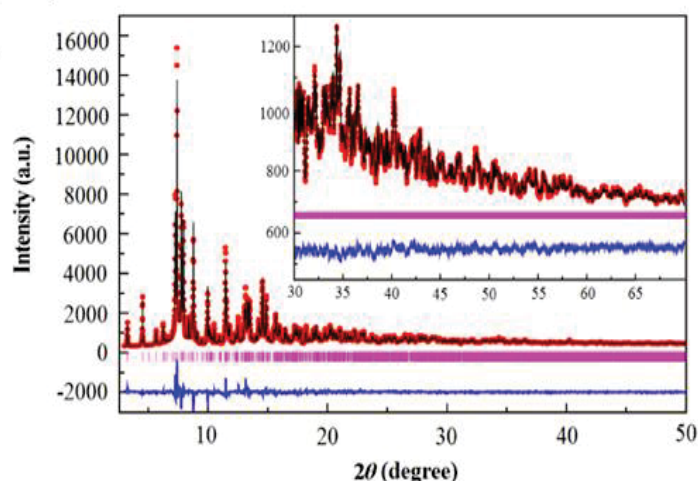
Figure 5-5 Fitting result of the high-resolution synchrotron-radiation XRD pattern of $BaBiO_{2.5}$. The inset shows the enlarged high angles region. The solid lines indicates the calculated diffraction, and round spots indicates the observed diffraction. The short lines indicate the Bragg reflections position. The difference between the observed and calculated diffraction is shown at the bottom in blue lines.

Table 5-1 Structure parameter from the Rietveld refinement for $BaBiO_{2.5}$ at 100 K.[a]

| Atom	Site	x	y	z	B (Å^2)
Ba	4e	0.8644(1)	0.0770(1)	0.2293(2)	0.29(1)
Bi	4e	0.3701(1)	0.1210(0)	0.2758(1)	0.36(0)
O1	2b	0.5000	0.0000	0.0000	1.00(0)
O2	4e	0.1788(9)	-0.0756(8)	0.3011(15)	1.06(21)
O3	4e	0.1728(11)	0.2526(11)	0.0497(13)	1.26(22)

The space group is $P2_1/c$. Lattice constant is a= 7.31256(8) Å, b=7.56805(10) Å, and c=6.03889(7) Å. R_{wp}, R_p, R_i, and R_f are 3.69%, 2.33%, 3.73%, and 2.00%, respectively. The bond lengths of Bi-O1, Bi-O2, short Bi-O3 and long Bi-O3 bonding are 2.24066(0), 2.06474(0), 2.07554(0), and 2.54854(0) Å, respectively.

5.2 Charge density distribution

The MEM/Rietveld analysis of SXRD data is usually recognized as a direct forward way to investigate the electron charge density distribution and the bonding nature between ions. In the MEM/Rietveld analysis, any kind of electron charge density distributions is enabled if the symmetry requirements are met. To perform the MEM/Rietveld analysis, high-quality of SXRD data with good counting statistics and high angular resolution are required, the SXRD pattern were herin collected at BL02B2 in SPring-8 using a large Debye-Scherrer camera with an imaging plate. The sample temperature was controlled using the N_2 gas flow system within 1 K resolution. No phase transition was observed with $BaBiO_{2.5}$ sample cooling down to 100 K. Owing to good signal-to-noise ratio for the data taken at 100 K with IP, we used the data in the following MEM/Rietveld analysis process. The number of structure factors determined from the Rietveld refinement is 7345. The MEM/Rietveld analysis was then performed in an unit cell with 148 x 152 x 120 pixels. The reliability of structure factor used in the final MEM charge density is 2.00%.

As shown in the Fig. 5-6, the features of Bi-O and Ba-O bondings are successfully visualized in the MEM electron charge density map. Obviously, the electron charge densities between Bi and O are observed to be anisotropic, which are found to be strongly overlapped between the Bi and O1, O2, and O3 ions. The Bi-O1, Bi-O2, and short Bi-O3 bondings shows the minimum electron charge densities of 0.35, 0.48, and 0.48 e/Å^3, respectively, which reveals the appearance of the Bi-O covalent bonds. In contrast, the longer Bi-O3 bond is found to have a 0.22 e/Å^3 minimum charge density, that is almost the same value of the charge density of background level, revealing its ionic bonding nature. All information mentioned above suggest that the Bi-O bonds in $BaBiO_{2.5}$ form not only the covalent but also the ionic bond, showing a clearly experimental evidence for unusual orbital hybridization of Bi and O ions. In marked contrast, it is obvious that Ba possess ionic bonds with

neighbored coordinated oxygen ions. In view of the special electron charge density distribution and asymmetric local coordination of Bi ions in $BaBiO_{2.5}$, it can be expected that the lattice is easily deformed under external stimulation.
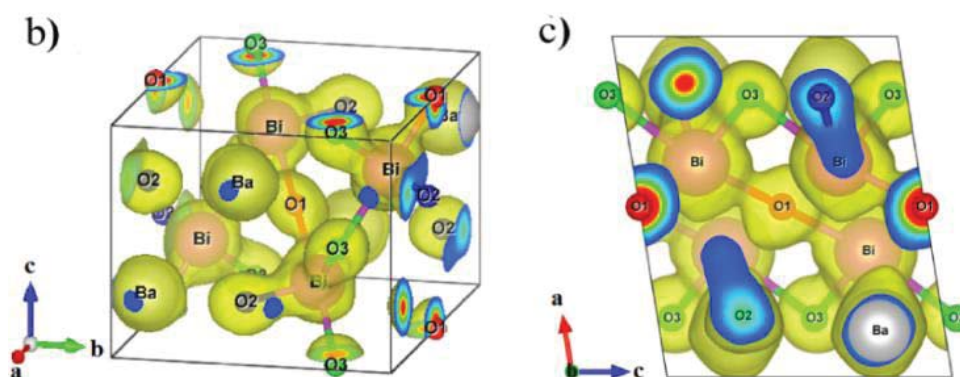
Figure 5-6. 3D electron charge density distribution maps of $BaBiO_{2.5}$ along different axis. The isosurface is 0.3 e Å^{-3}.

EXAFS is a well-known powerful method for examining the local coordination environment around the absorbed ions, we further performed the extended X-ray absorption fine structure spectroscopy (EXAFS) at the L_3 edge of Bi in $BaBiO_{2.5}$ to supplement the MEM/Rieveld analysis result as shown in Fig. 5-7. In the EXAFS experiments, the structure parameter obtained by the MEM/Rietveld method was used as a primitive model. The model and experimental spectra in the k or R space show a good agreement. Best-fit parameters and the quality of the fit are collected in Table 5-2. The goodness-of-fit parameter, the R_{factor}, of this fitting is 0.0083. R is half of the global scattering path length, and σ^2 is the mean square displacement factor; both were obtained from the fitting. We also show the R_{eff} values for each path, which were obtained by using as input the structure as determined by the MEM/Rietveld analysis of the SXRD pattern of $BaBiO_{2.5}$ taken at 100 K. One may note that the EXAFS spectrum of $BaBiO_{2.5}$ was performed at room temperature, which attribute to larger R compared to R_{eff}.
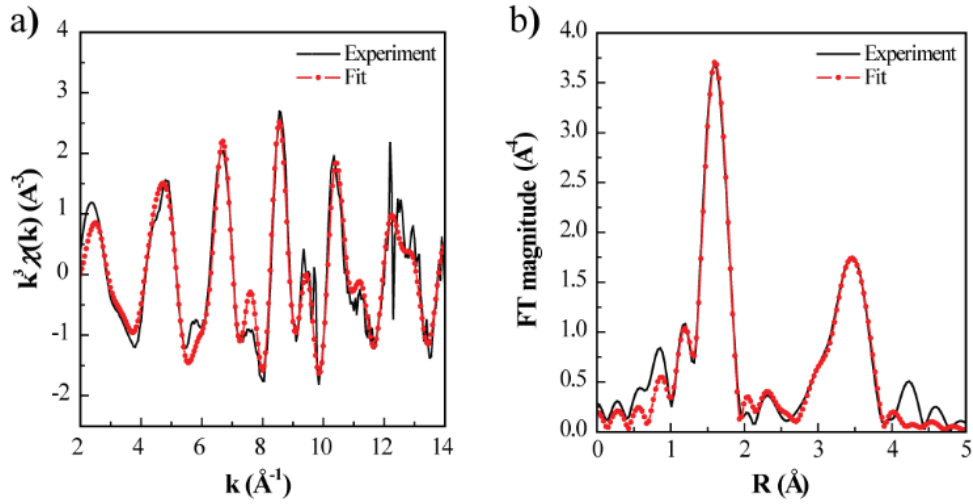
Figure 5-7. a) Bi L_3-edge k^3-weighted EXAFS spectra and b) the Fourier transform (FT) spectra of the k^3-weighted EXAFS of $BaBiO_{2.5}$. The fitting range in R space is 1-4 Å.

Table 5-2. Main results of the fit performed on the k^3-weighted EXAFS spectrum of $BaBiO_{2.5}$.

Path	R_{eff} (Å)	R (Å)	σ^2 (Å^{-2})
Bi-O2.1	2.070	2.104±0.016	0.0040±0.0008
Bi-O1.1	2.241	2.266±0.007	0.0059±0.0048
Bi-O3.2	2.549	2.577±0.008	0.0025±0.0024
Bi-O1.2	3.248	3.285±0.010	0.0129±0.0027
Bi-Bi.1	3.556	3.597±0.011	0.0071±0.0008
Bi-Ba.1	3.581	3.621±0.011	0.0097±0.0015
Bi-Bi.2	3.596	3.636±0.011	0.0072±0.0008
Bi-Ba.2	3.682	3.724±0.011	0.0097±0.0015

5.3 Photoluminescence mechanism

$BaBiO_{2.5}$ shows the unique electron density distribution and bonding nature,

which have prompted us to examine its photophysical properties using a variety of spectroscopic techniques. Compared with non-luminous $BaBiO_3$, the room temperature NIR PL peak of $BaBiO_{2.5}$ is 1186 nm, the full width at half maximum is 27 nm, and it is accompanied with two weak emission bands at 1238 and 1296 nm as shown in Fig. 5-8. When various excitation power densities were used, the intensity ratio or emission curve of the three emission bands remain almost unchanged as shown in Fig.5-9. We noticed that the compound showed no other emission bands in the range of 300-1000 nm. All these results indicate that there is only one class of luminescent substances in the system, which is in sharp contrast to other Bi-containing materials that usually contain multiple types of emitters.
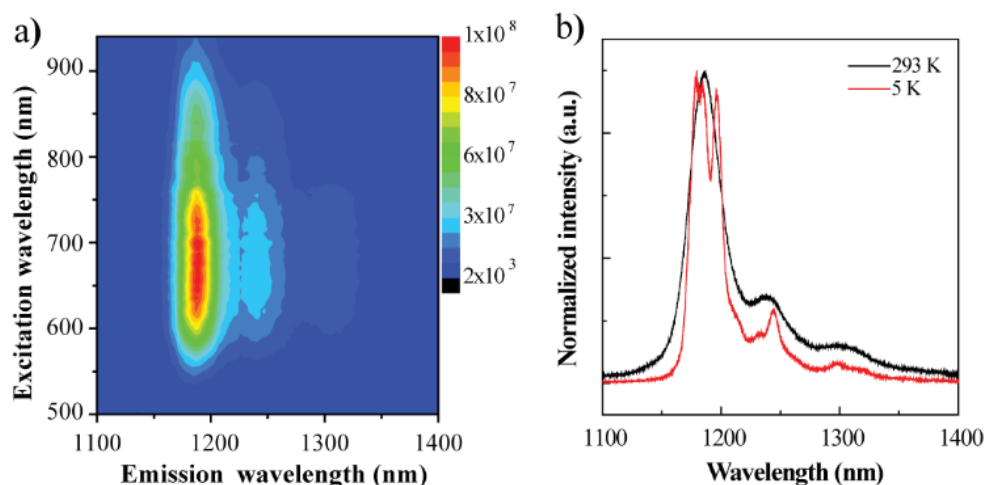
Figure 5-8. a) Excitation-emission graph of $BaBiO_{2.5}$. b) PL spectra of $BaBiO_{2.5}$ performed at 293 and 5 K under the excitation of 658 nm.
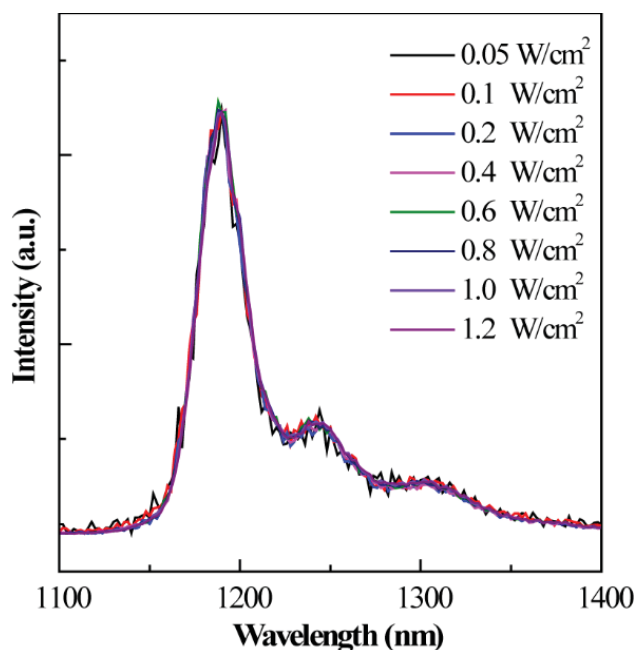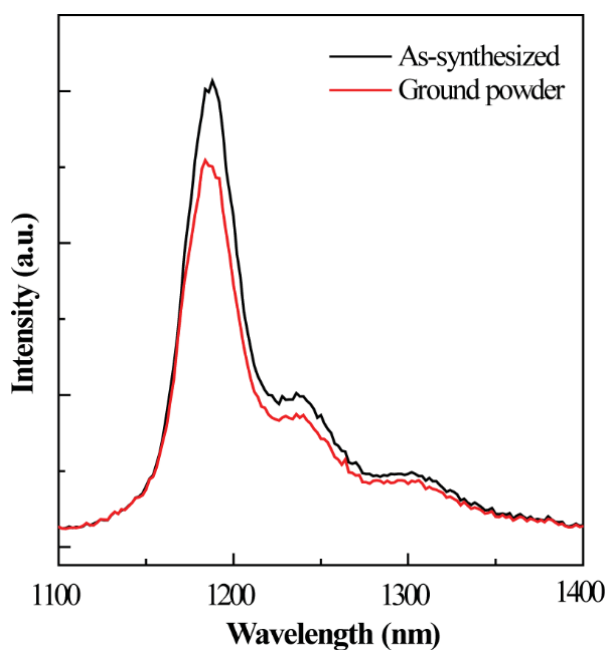
Figure 5-9. Normalized room-temperature PL spectra of BaBiO$_{2.5}$ under 658 nm excitation with different excitation power densities.

We find that the excitation or emission nature of BaBiO$_{2.5}$ are obviously different from those of other observed systems containing Bi ions, such as Bi^{3+}, Bi^{2+} or Bi^{+} ions, which allows us to exclude the possibility of emission from those species. There are two kind of possible emitters, permanent material defects (such as surface defects or dopants) and transient light emitting defects (such as excitons) that may cause the observed PL.[105,106] It is recognized that the emission of permanent material defects usually exhibits a sublinear dependence on the excitation power intensity, which eventually saturates when all defects are filled. Therefore, we performed the PL spectrum of BaBiO$_{2.5}$ with dependence of excitation power density. The PL intensity was observed to increase linearly with the excitation power density from 0.05 to 1.2 W cm^{-2}, indicating no PL saturation as shown in Fig. 5-10.

Although material degradation usually prevents the application of higher excitation power densities, this linear correlation indicates that the luminescence does not come from surface defects. In addition, for the synthesized and reground powders, we observed almost same emission curves and PL intensities as shown in Fig.5-11, further indicating that the emission is from an overall bulk effect, not a surface defect.
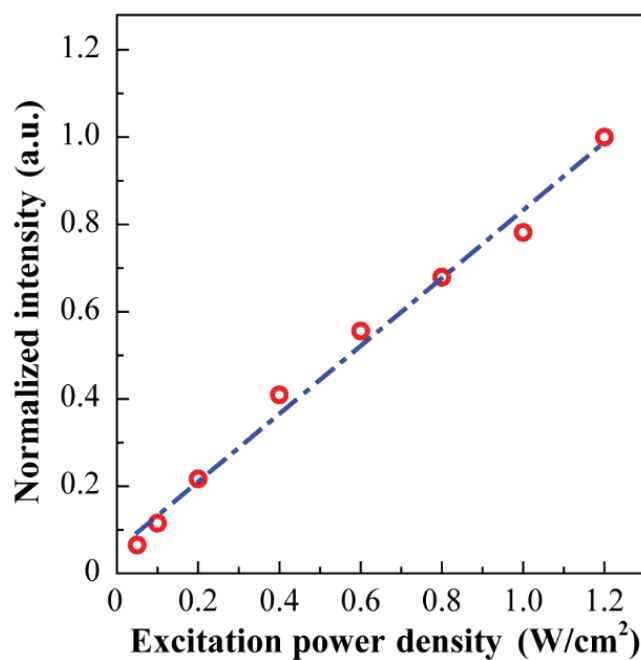
Figure 5-10. Room-temperature emission intensity of $BaBiO_{2.5}$ under 658 nm excitation with dependence of excitation powder densities.

Figure 5-11. Room-temperature PL spectra of the synthesized and ground $BaBiO_{2.5}$ powders under 658 nm excitation.

As we all know, self-trapped excitons (STEs) are one kind of transient defects

formed during light excitation, in which photo-generated charge carriers can be stabilized by large elastic lattice distortion driven by electron-phonon coupling. In other word, when external stimuli is subjected , the deformable lattice is conducive to the formation of STE. Since there is no PL saturation as shown in Fig. 5-12, almost the same emission curve at various excitation energy and the asymmetric coordination geometry of Bi, we speculate that the observed NIR emission may originate from STEs.
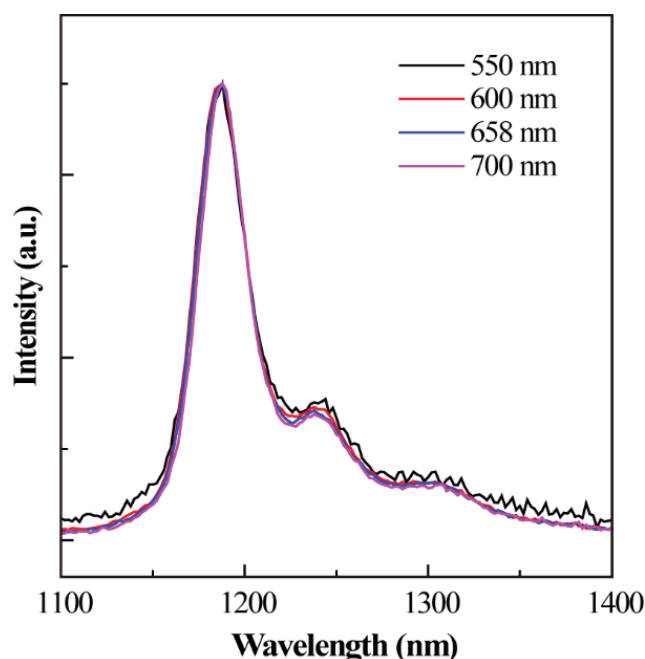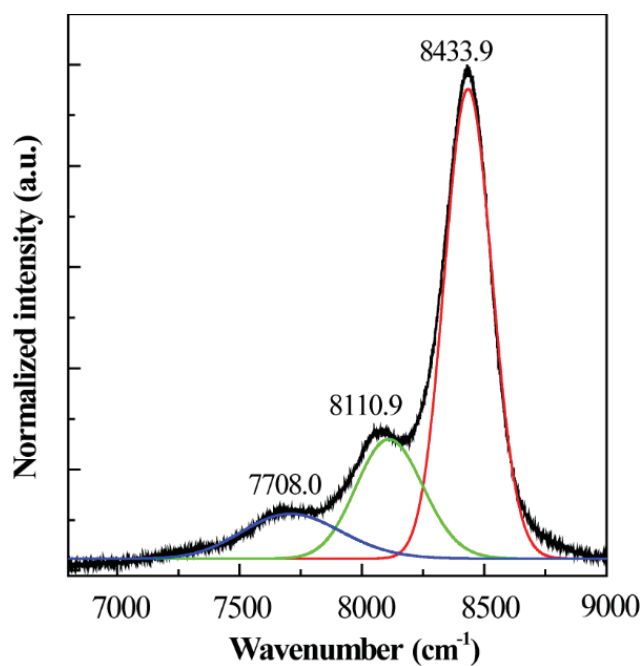

Figure 5-12. Room-temperature PL spectra of $BaBiO_{2.5}$ under different excitation wavelengths.

As shown in Fig. 5-13, $BaBiO_{2.5}$ shows an indirect band gap about 2.48 eV and a below-gap absorption band, which is consistent with the PL excitation lineshape as shown in Fig.5-8 a. Obviously, the room temperature PL spectrum is divided into three peaks, whose energies are 323 and 403 cm^{-1}, respectively, which is equivalent to the phonon energy of 321 cm^{-1} and the sum of phonon energy of 321 and 81 cm^{-1} as shown in Fig. 5-14. Therefore, we assume that the splitting is owing to electron-phonon coupling, that is the nature of vibration development. We note that similar multi-band exciton emission is also observed in the layered perovskite

containing lead, such as $(C_4H_9NH_3)_2PbI_4$.
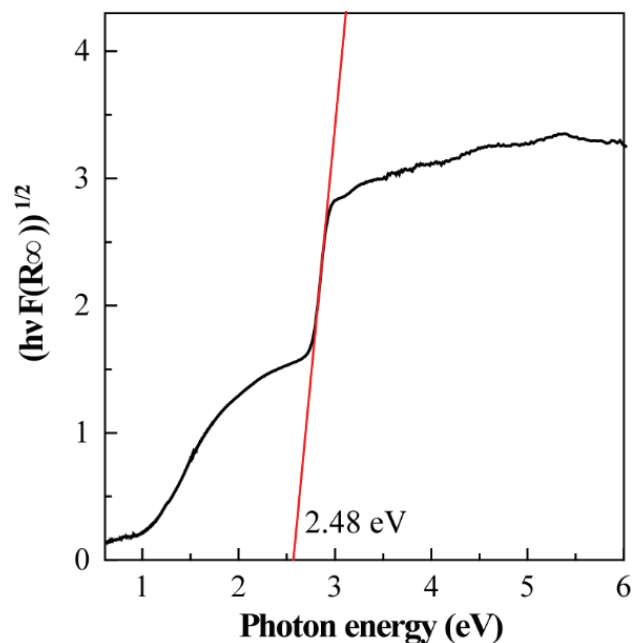
Figure 5-13. T_{auc} plot of $(hvF(R\infty))^{1/2}$ as a function of the photon energy, which is indicative of an indirect bandgap. The below-bandgap absorption can be assigned to the exciton absorption as discussed in the main text.
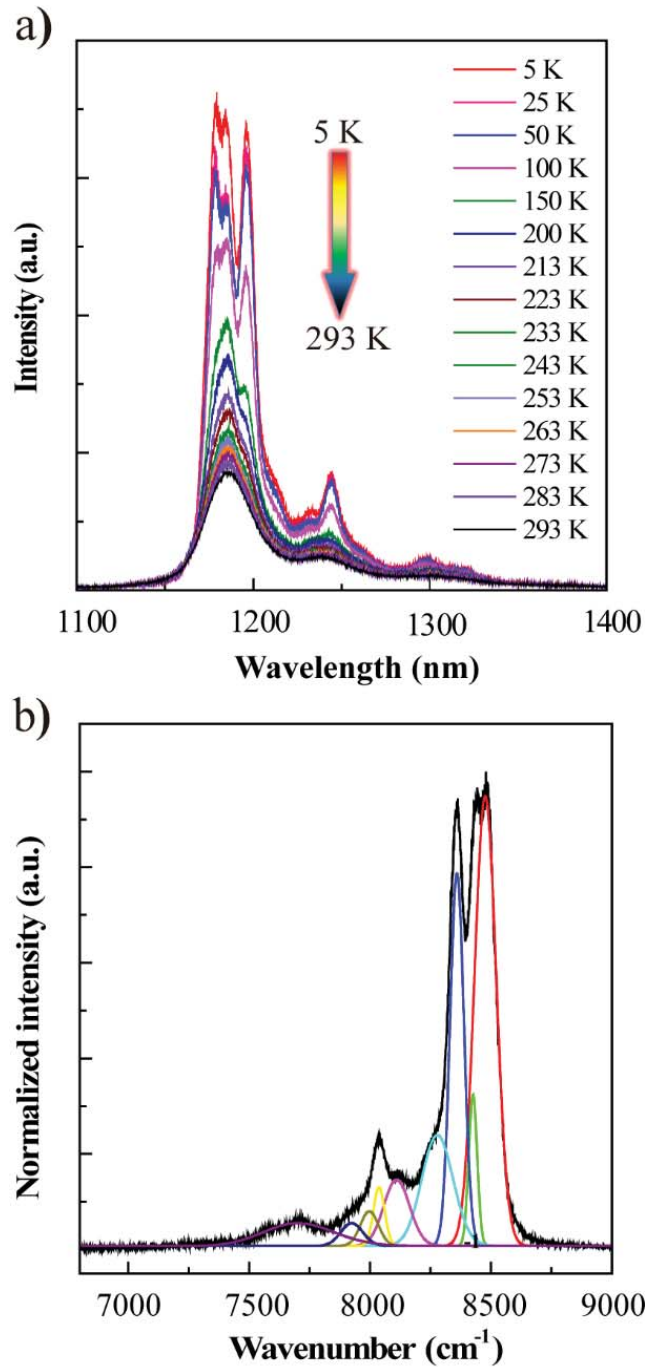

Figure 5-14. Room-temperature PL spectrum of $BaBiO_{2.5}$ under 658 nm excitation. Black and colored curves are experimentally measured and decomposed PL curves,

respectively.

Interestingly, lowering the temperature will result in sharply resolved peaks from the room temperature PL bands as shown in Fig 5-8 b and Fig. 5-15. The spectra collected at 5 K show about nine peaks, and the energy interval between neighbored peaks is less than 230 cm^{-1} as shown in Fig. 5-15 b and Table 5-3.

Table 5-3. The decomposed peak position and energy spacing between adjacent peaks for PL at 5 K. The spacing is calculated by subtracting the peak energy of low-frequency emission from that of the adjacent high-frequency emission. We also listed the phonon energy of $BaBiO_{2.5}$ that is comparable to the corresponding energy spacing. We note that only the spacing of 39.9 cm^{-1} shows a relatively large difference with respect to the phonon energy of 53 cm^{-1}, which may be due to the strong overlapping of the emissions in this spectral region or the existence of the vibrational mode at ca. 40 cm^{-1} for $BaBiO_{2.5}$.

Peak position (cm^{-1})	Energy spacing (cm^{-1})	Phonon energy (cm^{-1})
8476.8		
8425.7	51.1	53
8359.7	66.0	67
8278.5	81.2	81
8110.1	168.4	171
8037.4	72.7	67
7997.5	39.9	53
7924.4	73.1	67
7702.1	222.3	227

Figure 5-15. a) PL spectra of $BaBiO_{2.5}$ with dependence of temperature. b) Decomposed PL spectra. Black and colored curves indicate the experiment and decomposed PL spectra, respectively.

We recommend that the Raman mode at 321 cm^{-1} at low temperatures is frozen, which results in the appearance of radiation recombination involving low-frequency modes. In addition, $BaBiO_{2.5}$ shows almost the same attenuation at different

wavelengths of 5 K as shown in Fig. 5-16, further indicating the vibration characteristics of PL. We noticed that narrow-band PL was quite rare in the compounds containing Bi.[107] The special structure of PL in this layered Bi-containing structure is well investigated for the first time, which may be owing to the weak coupling between emissive state and lattice vibration, compared with the strong coupling in those compounds with three-dimensional crystals or glass-like lattices.
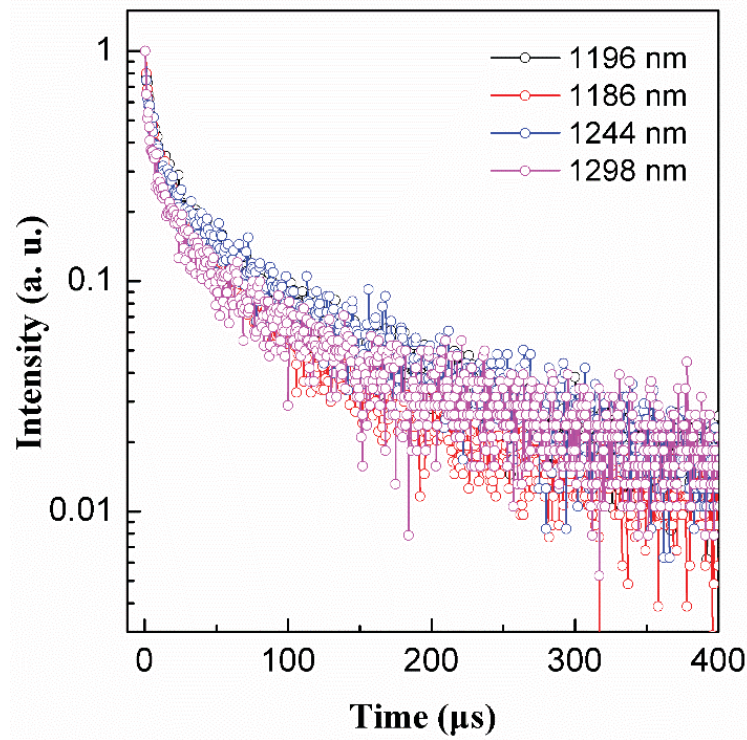

Figure 5-16. PL decay curves of $BaBiO_{2.5}$ at 5 K monitored at different emission wavelengths.

In order to gain a deeper understanding of the microscopic mechanism of STEs formation in $BaBiO_{2.5}$, we next performed the band structure and density of states calculations using the density functional theory (DFT). When using the general gradient approximation (GGA)/Perdew-Burke-Ernzerhof (PBE) functional, $BaBiO_{2.5}$ is calculated to have an indirect bandgap of 2.85 eV, that is slightly larger than the experimental value of 2.48 eV. The valence band maximum is found to located at the

G point, and the conduction band is located at the *B* point of the Brillouin zone as shown in Fig. 5-17.

Partial state density (PDOS) shows that O $2p$ orbital mainly contribute to the maximum of valence band at the G point, meanwhile, Bi $6p$ and O $2p$ orbits mainly compose the conduction band, which indicates a strong hybridization of Bi $6p$ and O $2p$ orbitals. As the experiment shows, this is found to be very consistent with the special bonding nature between Bi and O.

Based on experiment results, we then suggest that the photo-generated self-trapping holes should be originated from the state of O and/or Bi. We emphasize that more works are necessary to deepen the understanding of relationship of the crystal structure and physical property in this system. Particularly, calculation research on the allocation of various vibration modes of $BaBiO_{2.5}$ and the details of electron-phonon coupling is useful to obtain a deep understanding of these properties, which is still an open question for more studies.
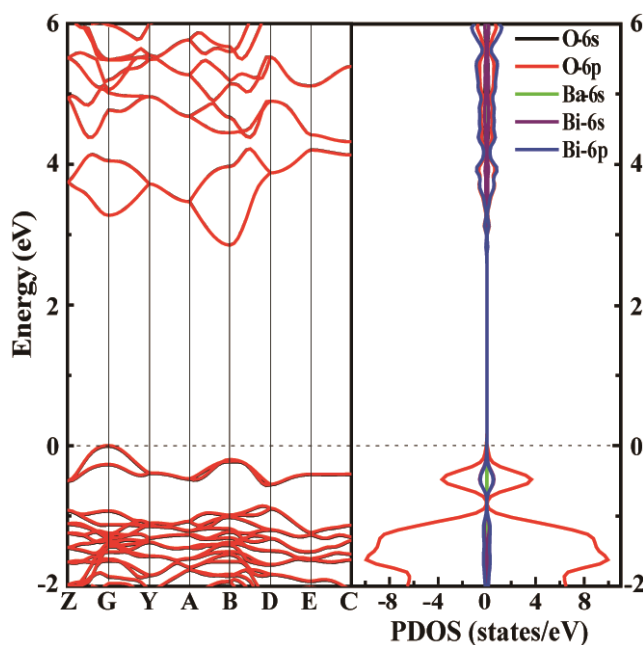
Figure 5-17. Calculated band structure and spin-up and spin-down states PDOS of $BaBiO_{2.5}$.

5.4 Conclusion

In summary, we have successfully synthesized the pure layered $BaBiO_{2.5}$ transformed from the perovskite-type oxide $BaBiO_3$. Using the MEM/Rietveld method combined with the high-resolution synchrotron-radiation X-ray diffraction data, the electron charge density distributions of $BaBiO_{2.5}$ are evaluated for the first time. The unusual chemical bonds between Bi and O ions are observed, which consists of three covalent bonds and one ionic bond. Hence, an unusual coordination environment is formed. We found that this special asymmetric structure shows the NIR PL that is different from the conventional Bi-containing light-emitting system. The combination of extensive spectral analysis and theoretical calculations has inspired us to suggest that the observed PL may be derived from the phonon-assisted radiation recombination of STEs associated with O and/or Bi states. Our work emphasizes that synthesis of materials with unique Bi-O bonds and unusual Bi coordination geometry would provide a way to discover systems with emerging properties. We believe that this work may stimulate a strong interest in exploring various materials containing Bi or other heavier p-block elements, which provides attractive prospects for finding new systems with intriguing characteristics.

Acknowledgment

Last, I am honored and happy to be a member of our laboratory and a student of my two lovely teachers.

References

[1] B. Martínez, X. Obradors, A. Gou, V. Gomis, S. Piñol, J. Fontcuberta, and H. Van Tol, Phy. Rev. B **53** (1996) 2797.

[2] Y. Long and Y. Shimakawa, New J. Phys. **12** (2010) 1906.

[3] J. Blasco, J. García, J. M. de Teresa, M. R. Ibarra, J. Perez, P. A. Algarabel, C. Marquina, and C. Ritter, Phys. Rev. B **55** (1997) 8905.

[4] W. T. Chen, Y. Long, T. Saito, J. Paul Attfield, and Y. Shimakawa, J. mater. Chem. **20** (2010) 7282.

[5] R. Shannon, Acta Crystallogr., Sec. A **32** (1976) 751.

[6] A. V. Hippel, R. G. Breckenridge, F. G. Chesley, and L. Tisza, Ind. Eng. Chem. **38** (1946) 1097.

[7] B. Wul and I. M. Goldman, C. R. Acad. Sci. USSR **51** (1946) 21.

[8] S. A. Hayward, S. A. T. Redfern, and E. K. H. Salje, J. Phys.: Condens. Mat. **14** (2002) 10131.

[9] G. King and P. M. Woodward, J. Mater. Chem. **20** (2010) 5785.

[10] T. Kimura, T. Goto, H. Shintani, K. Ishizaka, T. Arima and Y. Tokura, Nature **426** (2003) 55

[11] M. B. Salamon and M. Jaime, Rev. Mod. Phys. **73** (2001), 583.

[12] Y. Krockenberger, K. Mogare, M. Reehuis, M. Tovar, M. Jansen, G. Vaitheeswaran, V. Kanchana, F. Bultmark, A. Delin, F. Wilhelm, A. Rogalev, A. Winkler and L. Alff, Phys. Rev. B **75** (2007) 020404.

[13] T. Alamelu, U. V. Varadaraju, M. Venkatesan, A. P. Douvalis and J. M. D. Coey, J. Appl. Phys. **91** (2002) 8909.

[14] H. Kato, T. Okuda, Y. Okimoto, Y. Tomioka, Y. Takenoya, A. Ohkubo, M. Kawasaki and Y. Tokura, Appl. Phys. Lett. **81** (2002) 328.

[15] Y. Tokura, K. I. Kobayashi, T. Kimura, H. Sawada and K. Terakura, Nature **395** (1998) 677.

[16] Y. Tomioka, T. Okuda, Y. Okimoto, R. Kumai, K. I. Kobayashi and Y. Tokura, Phys. Rev. B **61** (2000) 422.

[17] D. Serrate, J. M. De Teresa and M. R. Ibarra, J. Phys.: Condens. Mat. **19** (2007) 023201.

[18] A. K. Paul, M. Jansen, B. Yan, C. Felser, M. Reehuis and P. M. Abdala, Inorg. Chem. **52** (2013) 6713.

[19] H. L. Feng, M. Arai, Y. Matsushita, Y. Tsujimoto, Y. Guo, C. I. Sathish, X. Wang, Y. Yuan, M. Tanaka and K. Yamaura, J. Am. Chem. Soc. **136** (2014), 3326.

[20] R. Morrow, J. W. Freeland and P. M. Woodward, Inorg. Chem. **53** (2014) 7983.

[21] A. K. Paul, M. Reehuis, V. Ksenofontov, B. Yan, A. Hoser, D. M. Tobbens, P. M. Abdala, P. Adler, M. Jansen and C. Felser, Phys. Rev. Lett. **111** (2013) 167205.

[22] Y. S. Hou, H. J. Xiang and X. G. Gong, Sci. Rep. **5** (2015) 13159.

[23] S. V. Ovsyannikov, M. Bykov, E. Bykova, D. P. Kozlenko, A. A. Tsirlin, A. E. Karkin, V. V. Shchennikov, S. E. Kichanov, H. Y. Gou, A. M. Abakumov, R. Egoavil, J. Verbeeck, C. McCammon, V. Dyadkin, D. Chernyshov, S. van Smaalen and L. S. Dubrovinsky, Nature Chem. **8** (2016) 501.

[24] B. Lavina, P. Dera, E. Kim, Y. Meng, R.T. Downs, P. Weck, S.R. Sutton and Y. Zhao, Proc. Natl. Acad. Sci. USA. **108** (2011) 17281.

[25] Y. W. Long, N. Hayashi, T. Saito, M. Azuma, S. Muranaka and Y. Shimakawa, Nature **458** (2009) 60.

[26] Y. W. Long, T. Kawakami, W. T. Chen, T. Saito, T. Watanuki, Y. Nakakura, Q. Q. Liu, C. Q. Jin and Y. Shimakawa, Chem. Mater. **24** (2012) 2235.

[27] T. Mizokawa and A. Fujimori, Phys. Rev. B **56** (1997) R493.

[28] D. H. Kim, H. M. Christen, M. Varela, H. N. Lee and D. H. Lowndes, Appl. Phys. Lett. **88** (2006) 202503.

[29] J. Fontcuberta, V. Laukhin and X. Obradors, Phys. Rev. B **60** (1999) 6266.

[30] S. Aoyagi, PhD thesis, Okayama University, 2002 [in Japanese].

[31] T. Nakamura, Ferroelectricity involved Structural Phase Transitions (Shokabo, Tokyo, 1988) [in Japanese].

[32] J. Harada, J. Cryst. Soc. Jpn 20, 1 (1978) [in Japanese].

[33] W. Zhong and D. Vanderbilt, Phys. Rev. Lett. **74** (1995) 2587.

[34] G. Pavel and J. B. Andrew, J. Phys.: Condens. Mat. **19** (2007) 176201.

[35] A. Glazer, Acta Crystallogr., Sec. B **28** (1972) 3384.

[36] P. Woodward, Acta Crystallogr., Sec. B **53** (1997) 32.

[37] M. E. Jones and R. E. Marsh, J. Am. Chem. Soc. **76** (1954) 1434.

[38] E. Nishibori, M. Takata, M. Sakata, H. Tanaka, T. Muranaka and J. Akimitsu, J. Phys. Soc. Jpn **70** (2001) 2252.

[39] K. Kato, M. Takata, Y. Moritomo, A. Nakamoto and N. Kojima, Appl. Phys. Lett. **90** (2007) 201902.

[40] Y. Kuroiwa, S. Aoyagi, A. Sawada, J. Harada, E. Nishibori, M. Takata and M. Sakata, Phys. Rev. Lett. **87** (2001) 217601.

[41] H. Tanaka, Y. Kuroiwa and M. Takata, Phys. Rev. B **74** (2006) 172105.

[42] P. Maselli, D. Nicoletti, A. Nucara, F. M. Vitucci, A. Irizawa, K. Shoji, T. Nanba and P. Calvani, EPL (Europhysics Letters) **92** (2010) 47001.

[43] K. Kato, M. Takata, E. Nishibori, M. Sakata, N. Hamada and Y. Moritomo, J. Phys. Soc. Jpn. **74** (2005) 2137.

[44] A. W. Sleight, J. L. Gillson and P. E. Bierstedt, Solid State Commun. **88** (1993) 841.

[45] R. J. Cava, B. Batlogg, J. J. Krajewski, R. Farrow, L. W. Rupp Jr, A. E. White, K. Short, W. F. Peck and T. Kometani, Nature **332** (1988) 814.

[46] D. G. Hinks, B. Dabrowski, J. D. Jorgensen, A. W. Mitchell, D. R. Richards, S. Pei and D. Shi, Nature **333** (1988) 836.

[47] S. M. Kazakov, C. Chaillout, P. Bordet, J. J. Capponi, M. Nunez-Regueiro, A. Rysak, J. L. Tholence, P. G. Radaelli, S. N. Putilin and E. V. Antipov, Nature **390** (1997) 148.

[48] A. M. Huerta-Flores, D. Sanchez-Martinez, M. del Rocío Hernández-Romero, M. E. Zarazúa-Morín and L. M. Torres-Martínez, J. Photoch. Photobio. A **368** (2019) 70.

[49] J. Tang, Z. Zou and J. Ye, J. Phys. Chem. C **111** (2007) 12779.

[50] M. Khraisheh, A. Khazndar and M.A. Al-Ghouti, Int. J. Energy Res. **39** (2015) 1142.

[51] J. Tang, Z. Zou and J. Ye, Angew. Chem., Int. Ed. **43** (2004) 4463.

[52] J. Sato, H. Kobayashi and Y. Inoue, J. Phys. Chem. B **107** (2003) 7970.

[53] A. W. Sleight, Physica C **514** (2015) 152.

[54] M. Yasukawa and N. Murayama, Physica C **297** (1998) 326.

[55] A. Ghosh, Solid State Commun. **112** (1999) 45.

[56] S. H. Lee, W. H. Jung, J. H. Sohn, J. H. Lee and S. H. Cho, J. Appl. Phys. **86** (1999) 6351.

[57] D. E. Cox and A. W. Sleight, Solid State Commun. **19** (1976) 969.

[58] Q. Zhou and B. J. Kennedy, Solid State Commun. **132** (2004) 389.

[59] B. J. Kennedy, C. J. Howard, K. S. Knight, Z. Zhang and Q. Zhou, Acta Cryst. B **62** (2006) 537.

[60] S. Pei, J. D. Jorgensen, B. Dabrowski, D. G. Hinks, D. R. Richards, A. W. Mitchell, J. M. Newam, S. K. Shiha, D. Vaknin and A. J. Jacobson, Phys. Rev. B **41** (1990) 4126.

[61] H. Krakauer and W. E. Pickett, Phys. Rev. Lett. **60** (1988) 1665.

[62] S. Sanna, V. Esposito, J. W. Andreasen, J. Hjelm, W. Zhang, T. Kasama, S. B. Simonsen, M. Christensen, S. Linderoth and N. Pryds, Nat. Mater. **14** (2015) 500.

[63] H. Taniguchi, A. Kuwabara, J. Kim, Y. Kim, H. Moriwake, S. Kim, T. Hoshiyama, T. Koyama, S. Mori, M. Takata, H. Hosono, Y. Inaguma and M. Itoh, Angew. Chem. Int. Ed. **52** (2013) 8088.

[64] G. Catalan and J. F. Scott, Adv. Mater. **21** (2009) 2463.

[65] Y. Hosaka, F. Denis Romero, N. Ichikawa, T. Saito and Y. Shimakawa, Angew. Chem. Int. Ed. **56** (2017) 4243.

[66] I. D. Brown, Chem. Rev. **109** (2009) 6858.

[67] H.-T. Sun, J. Zhou and J. Qiu, Prog. Mater. Sci. **64** (2014) 1.

[68] Z. Huang, J. E. Auckett, P. E. Blanchard, B. J. Kennedy, W. Miiller, Q. Zhou, M. Avdeev, M. R. Johnson, M. Zbiri, G. Garbarino, W. G. Marshall, Q. Gu, C. D. Ling, Angew. Chem. Int. Ed. **53** (2014) 3414.

[69] D. E. Cox and A. W. Sleight, Solid State Commun. **19** (1976) 969.

[70] G. Kim, M. Neumann, M. Kim, M. D. Le, T. D. Kang and T. W. Noh, Phys. Rev. Lett. **115** (2015) 226402.

[71] N. C. Plumb, D. J. Gawryluk, Y. Wang, Z. Ristic, J. Park, B. Q. Lv, Z. Wang, C. E.

Matt, N. Xu, T. Shang, K. Conder, J. Mesot, S. Johnston, M. Shi and M. Radovic, Phys. Rev. Lett. **117** (2016) 037002.

[72] M. A. Hayward, M. A. Green, M. J. Rosseinsky and J. Sloan, J. Am. Chem. Soc. **121** (1999) 8843.

[73] M. A. Hayward, E. J. Cussen, J. B. Claridge, M. Bieringer, M. J. Rosseinsky, C. J. Kiely, S. J. Blundell, I. M. Marshall and F. L. Pratt, Science **295** (2002) 1882-1884.

[74] Y. Tsujimoto, C. Tassel, N. Hayashi, T. Watanabe, H. Kageyama, K. Yoshimura, M. Takano, M. Ceretti, C. Ritter and W. Paulus, Nature 450 (2007) 1062.

[75] H. Kageyama, T. Watanabe, Y. Tsujimoto, A. Kitada, Y. Sumida, K. Kanamori, K. Yoshimura, N. Hayashi, S. Muranaka, M. Takano, M. Ceretti, W. Paulus, C. Ritter and G. Andre, Angew. Chem. Int. Ed. **47** (2008) 5740.

[76] S. Tominaka, Y. Tsujimoto, Y. Matsushita and K. Yamaura, Angew. Chem. Int. Ed. **50** (2011) 7418.

[77] a) G. K. Behrh, H. Serier-Brault, S. Jobic and R. Gautier, Angew. Chem. Int. Ed. **54** (2015) 11501; b) H. Barroux, T. Jiang, C. Paul, F. Massuyeau, R. Génois, E. E. Gordon, M.-H. Whangbo, S. Jobic and R. Gautier, Chem. Eur. J. **23** (2017) 2998.

[78] a) B. M. Liu, Z. G. Zhang, K. Zhang, Y. Kuroiwa, C. Moriyoshi, H. M. Yu, C. Li, L. R. Zheng, L. N. Li, G. Yang, Y. Zhou, Y. Z. Fang, J. S. Hou, Y. Matsushita and H.-T. Sun, Angew. Chem. Int. Ed. **55** (2016) 4967; b) K. Zhang, C.-G. Ma, J.-Y. Zhang, B.-M. Liu, Y. Zhou, S.-Q. Guo, J.-Y. Xu, J.-S. Hou, Y.-Z. Fang, L.-R. Zheng and H.-T. Sun, Adv. Optical Mater. **5** (2017) 1700448.

[79] S. Inoue, M. Kawai, N. Ichikawa, H. Kageyama, W. Paulus and Y. Shimakawa, Nat. Chem. **2** (2010) 213.

[80] H. S. Kim, J. B. Cook, H. Lin, J. S. Ko, S. H. Tolbert, V. Ozolins and B. Dunn, Nat. Mater. **16** (2017) 454.

[81] F. Lei, Y. Sun, K. Liu, S. Gao, L. Liang, B. Pan and Y. Xie, J. Am. Chem. Soc. **136** (2014) 6826.

[82] L. Tian, H. Zou, J. Fu, X. Yang, Y. Wang, H. Guo, X. Fu, C. Liang, M. Wu, P. K. Shen and Q. Gao, Adv. Func. Mater. **20** (2010) 617.

[83] P. Willmott, An Introduction to Synchrotron Radiation (Wiley, West Sussex,

2011).

[84] Outline Schematic view of beamline at source and optics of BL02B2
http://www.spring8.or.jp/wkg/BL02B2/instrument/lang-en/INS-0000000318/instrume
nt_summary_view

[85] E. Nishibori, M. Takata, K. Kato, M. Sakata, Y. Kubota, S. Aoyagi, Y. Kuroiwa,
M. Yamakata and N. Ikeda, Nucl. Instr. Meth. Phys. Res. A **62** (2001) 2095.

[86] S. Kawaguchi, M. Takemoto, K. Osaka, E. Nishibori, C. Moriyoshi, Y. Kubota, Y.
Kuroiwa and K. Sugimoto, Rev. Sci. Instrum. **88** (2017) 085111.

[87] H. Tanaka, M. Takata, E. Nishibori, K. Kato, T. Iishi and M. Sakata, J. Appl.
Crystallogr. **35** (2002) 282.

[88] K. Momma and F. Izumi, J. Appl. Crystallogr. **41** (2008) 653.

[89] B. Ravel and M. Newville, J. Synchrotron Radiat. **12** (2005) 537.

[90] G. Kresse and J. Furthmuller, Phys. Rev. B **54** (1996) 11169.

[91] J. P. Perdew, K. Burke and M. Ernzerhof, Phys. Rev. Lett. **77** (1996) 3865.

[92] J. Heyd, G. E. Scuseria and M. Ernzerhof, J. Chem. Phys. **124** (2006) 219906.

[93] H. Rietveld, J. Appl. Crystallogr. **2** (1969) 65.

[94] C. E. Shannon, Bell Syst. Tech. J. **27** (1948) 408.

[95] E. E. Jaynes, IEEE Trans. Syst. Sci. Cyb. SSC **4** (1968) 227.

[96] J. P. Burg, 37th Ann. Int. Meeting, "Soc. Explor. Geophys." Oklahoma City, OK,
1967

[97] D. M. Collins, Nature (London) **298** (1982) 49.

[98] M. Sakata, R. Mori, S. Kumazawa, M. Takata and H. Toraya, J. Appl. Cryst. **23**
(1990) 526.

[99] M. Sakata and M. Sato, Acta Crystallogr., Sec. A **46** (1990) 263.

[100] T. Saka and N. Kato, Acta Crystallogr., Sec. A **42** (1986) 469.

[101] M. Takata, Acta Crystallogr., Sec. A **64** (2008) 232.

[102] F. Mezzadri, D. Delmonte, F. Orlandi, C. Pernechele, G. Calestani, M. Solzi, M.
Lantieri, G. Spina, R. Cabassi, F. Bolzoni, M. Fittipaldi, M. Merlini, A. Migliori, P.
Manuel and E. Gilioli, J. Mater. Chem. C **4** (2016) 1533.

[103] S. J. Patwe, S. N. Achary, M. D. Mathews and A. K. Tyagi, J. Alloys Compd.

390 (2005) 100.

[104] I. D. Brown, Chem. Rev. **109** (2009) 6858.

[105] E. R. Dohner, A. Jaffe, L. R. Bradshaw and H. I. Karunadasa, J. Am. Chem. Soc. **136** (2014) 13154.

[106] a) T. Hu, M. D. Smith, E. R. Dohner, M. J. Sher, X. Wu, M. T. Trinh, A. Fisher, J. Corbett, X. Y. Zhu, H. I. Karunadasa and A. M. Lindenberg, J. Phys. Chem. Lett. **7** (2016) 2258; b) D. B. Mitzi, Chem. Mater. **8** (1996) 791; c) K. M. McCall, C. C. Stoumpos, S. S. Kostina, M. G. Kanatzidis and B. W. Wessels, Chem. Mater. **29** (2017) 4129.

[107] a) Y. Fujimoto and M. Nakatsuka, Jpn. J. Appl. Phys. **40** (2001) L279; b) E. M. Dianov, Light: Sci. Appl. **1** (2012) e12; c) H.-T. Sun, Y. Sakka, H. Gao, Y. Miwa, M. Fujii, N. Shirahata, Z. Bai and J.-G. Li, J. Mater. Chem. **21** (2011) 4060; d) H.-T. Sun, Y. Matsushita, Y. Sakka, N. Shirahata, M. Tanaka, Y. Katsuya, H. Gao and K. Kobayashi, J. Am. Chem. Soc. **134** (2012) 2918; e) B. Xu, S. Zhou, D. Tan, Z. Hong, J. Hao and J. Qiu, J. Appl. Phys. **113** (2013) 083503; f) L. S. Chi, R. S. Liu and B. J. Lee, J. Electrochem. Soc. **152** (2005) J93.